Molecular Dynamics Simulations of the Hydrogen Peroxyl Radical

---

A Dissertation

Presented to

The Faculty of the Graduate School

University of Missouri

In Partial Fulfillment

Of the Requirements for the Degree

Doctor of Philosophy

---

by

Jamin W. Perry

Prof. Donald L. Thompson, Dissertation Supervisor

May 2014

The undersigned, appointed by the dean of the Graduate School, have examined the dissertation entitled

Molecular Dynamics Simulations of the Hydrogen Peroxyl Radical presented by Jamin W. Perry,

a candidate for the degree of doctor of philosophy of Chemistry,

and hereby certify that, in their opinion, it is worthy of acceptance.

Professor Donald L. Thompson (Chair)

Professor John E. Adams (Member)

Professor Carol A. Deakyne (Member)

Professor Thomas D. Sewell (Member)

Professor Sashi Satpathy (Outside Member)

ACKNOWLEDGMENTS

I wish to offer my utmost thanks to Dr. Donald Thompson for giving me the opportunity to do research as a member of his group. While in his group, I learned a great many things about scientific computation ranging from cluster maintenance to programming and data analysis. I greatly appreciate his mentorship and his emphasis to "dwell on the details" has left an indelible mark in my approach to research and science.

A great many thanks go to my committee members for their flexibility and understanding during the process of completing the dissertation. I especially wish to thank Drs. Adams, Deakyne and Sewell for the advice and guidance they have all offered on science and life. I also benefited greatly from them opening their libraries to me. I dearly hope I returned all of the books which I borrowed. I also wish to thank all of the residents of the Theoretical Chemistry floor with whom I enjoyed numerous discussions and interactions.

Finally, I would like to extend my utmost gratitude to Dr. Albert Wagner for his interest in my work and guidance on a great many things. His attention to detail and insightful criticism forced me to be a better scientist and collaborator.

Outside the academic world, I wish to thank my parents, James and Janine Perry, for encouraging me to have an inquiring mind. Most importantly, I owe a great deal to Lyndsey Perry for suffering the burden of dealing with me through the ups and downs and proofing my writing in this document. While they probably won't ever read this, I thank my sons Liam and Harper for making this all worthwhile. On a final note to my mom who did not have a chance to see me complete my dissertation; this isn't purple smoke, but it comes pretty damn close.

TABLE OF CONTENTS

LIST OF TABLES

LIST OF FIGURES

LIST OF EQUATIONS

$$k(E) = \frac{1}{2}\left(\frac{\int d\Gamma \delta(H(\Gamma) - E)\delta(q_{RC} - q_c) \mid \dot{q}_{RC} \mid}{\int d\Gamma \delta(H(\Gamma) - E)} \right) \quad (21) \ldots 80$$

$$\nu_c = 4\pi R^2 \rho g(R)\left(\frac{\kappa T}{\pi\mu}\right)^{1/2} \quad (22) \ldots 84$$

$$V = V_{HO_2} + V_{Inter} + V_{Cell} \quad (23) \ldots 92$$

$$V_{Inter} = V_{HO_2-Ar} + V_{Ar-Ar} \quad (24) \ldots 92$$

$$V_{\mathrm{HO_2-Ar}} = \sum_{i \in HO_2} \sum_{j \in Ar} A_{ij} \exp(-B_{ij} r_{ij}) - \frac{C_{ij}}{r_{ij}^6} \quad (25) \ldots 92$$

$$V_{\mathrm{Ar-Ar}} = \sum_i \sum_{j>i} A_{ij} \exp(-B_{ij} r_{ij}) - \frac{C_{ij}}{r_{ij}^6} \quad (26) \ldots 92$$

$$A_{ij} = \sqrt{A_{ii} A_{jj}} \quad (27) \ldots 92$$

$$B_{ij} = \frac{1}{2}\left(B_{ii} + B_{jj}\right) \quad (28) \ldots 92$$

$$C_{ij} = \sqrt{C_{ii} C_{jj}} \quad (29) \ldots 92$$

$$V_{cell} = \sum_i \frac{\alpha r_i^2}{R^2} \exp(-\beta(R - r_i)) \quad (30) \ldots 93$$

$$S(\Delta) = \min[1, \max[0, 1 - 10g(r_{ij})^3 + 15g(r_{ij})^4 - 6g(r_{ij})^5]] \quad (31) \ldots 94$$

$$g(r_{ij}) = (r_{ij} - 2.5\sigma_{ij})(2.7\sigma_{ij} - 2.5\sigma_{ij})^{-1} \quad (32) \ldots 94$$

$$T_I = \frac{1}{3N\kappa} \sum \frac{p_x^2 + p_y^2 + p_z^2}{m} \quad (33) \ldots 99$$

$$P = \rho\kappa T_I - \frac{1}{3V} \sum\sum r_{ij} F(r_{ij}) \quad (34) \ldots 99$$

$$G_{roll} = \frac{1}{n} \sum_i^n G(n) + G(n-1) + \ldots + G(i) - G(i-1) \quad (35) \ldots 99$$

$$P_N = P_O \sqrt{\frac{T}{T_{roll}}} \quad (36) \ldots 99$$

ABSTRACT

The first study of this dissertation is focused on studies of the classical dynamics and associated rates of isomerization and dissociation of isolated HO_2. Comparisons are made between the three potential energy surfaces (PESs) used in these studies. The intramolecular vibrational energy redistribution (IVR) at energies above and below the threshold of isomerization is slow, especially for O–O stretch excitations, consistent with the regularity in the surfaces-of-section. The slow IVR rates lead to mode-specific effects that are prominent for isomerization and modest for unimolecular dissociation to $H + O_2$. Even with statistical distributions of initial energy, slow IVR rates result in bi-exponential decay for isomerization, with the slower rate correlated with slow IVR rates for O–O vibrational excitation. The calculated IVR results for all three PESs are reasonably well represented by an analytic, coupled three-mode energy transfer model.

The second study of this thesis is focused on the effects of pressure on the relaxation of the HO_2 embedded in a dense gas environment. A method of simulating the radical in an argon bath is proposed and validated. The time-dependent decay of vibrational energy is found to be bi-exponential for all of the simulated pressures. The relaxation rates at low pressures extrapolate poorly to the high-pressure results, with a turnover in the rate constants occurring at intermediate pressures. The effects of finite size on the simulation are investigated. Comparisons to studies with similar findings and additional considerations for understanding this behavior are discussed.

I. Introduction

The interplay of theory and experimentation has been a crucial engine advancing the understanding the mechanisms of unimolecular reactions.[1] The progression of theories describing unimolecular reactions are discussed in review articles[2] and in several monographs.[3] The Lindemann mechanism[4] is the foundation on which more recent theories are built upon. An example of this mechanism is the following

$$A + M \rightleftarrows A^* + M \tag{1}$$

and

$$A^* \rightarrow B, \tag{2}$$

where A is a reactant, A^* is a vibrationally excited reactant, B is a product and M is a buffer gas. The gist of the theory is that a chemical species gains and loses energy by collisions with the surrounding medium which can lead to a reaction occurring. At low pressures this is a bimolecular process, and at higher pressures the process in Eq. 2 becomes the rate determining step of the mechanism. However, this mechanism only qualitatively predicts the correct behavior of the reaction rate as a function of pressure.[3] The issue is that the internal state of the reactant must be addressed for better accuracy. The theories of Hinshelwood,[5] followed by those of Ramsberger, Rice,[6] and Kassel[7] (RRK) and Slater[8] all attempted to resolve the issue of how the internal energy of the chemical species affects the rate of reaction. These earlier theories provided a foundation for the extensions of RRK proposed by Marcus,[9] which has become known as RRKM theory. RRKM theory extends the ideas of RRK by incorporating a quantum-statistical mechanical description of the energization of a reactant species and transition state theory[1,3] to describe the conversion of the energized reactant to a product state. A key

assumption is that localization of energy in a vibrational degree of freedom is unimportant as long as the intramolecular redistribution of energy (IVR) amongst the vibrational modes is fast relative to the timescale of the reaction. An expectation of the assumption of fast IVR is that unimolecular reactions should occur in a probabilistic manner and where the reaction of a chemical species is independent of its initial state. A brief aside is necessary to discuss the nature of energy transfer amongst vibrational modes.

The first computational studies of nonlinear dynamics performed by Fermi, Pasta, and Ulam[10] (FPU) on the equipartion of energy in a one-dimensional anharmonic chain of oscillators yielded results that surprised the authors. The simulation consisted of exciting a single vibrational mode in a one-dimensional chain of oscillators and propagating the equations of motion. The intent was to study how nonlinear forces affected the transfer of energy to the higher vibrational modes of the system. However, they found that on a long time-scale, there was non-ergodic behavior with an almost complete relocalization of energy in the excited mode, which contradicted the expected equilibration of energy amongst the modes of the system. Additional work by Tuck and Menzel[11] showed that this long-time periodicity in the FPU work was in fact real and was not due to numerical error. Ford[12] showed the lack of relaxation in the FPU problem was due to the absence of resonances. The effect of resonance conditions on ergodic behavior in trajectories is generalized in the Kolmogorov, Arnol'd, and Moser theorem,[13a,22] which states that under a small perturbation periodic, or quasi-periodic motion in phase space will persist unless resonant conditions occur. This aside on nonlinear dynamics ties directly to a question that has been posed by others: Does the flow of energy amongst the

vibrational modes of a molecular system affect the rate of reaction?[2(b),13] The possible connection between non-statistical dynamics and the unimolecular reactivity motivated early classical trajectory studies of model tri-atomics by Bunker.[14] He found that frequency mismatches between vibrational modes due to mass differences could cause non-random lifetimes in the dissociating species. Bunker and Hase[15] further defined non-statistical lifetimes by differentiating between effects due to localization of energy and effects due to the phase space of chemical species being metrically decomposable.

Some expectations of the dynamics of HO_2 can be guided by observations that others have made while studying H_2O_2. There are numerous studies[16] which have furthered our understanding of this system; however, for brevity we focus on a few of the key conclusions. First, the motion of the HO is relatively decoupled from the other degrees of freedom of the system. Second, there is evidence of slow energy flow out of an excited HO mode that has been prepared in an overtone state. This slow energy flow could contribute to non-exponential population decay of a sample. Finally, participation of the lower-frequency modes and rotational motion along an axis defined by the O-O bond has the effect of increasing the rate of IVR. While the addition of a hydrogen atom to HO_2 leads to considering the motion of three more internal degrees of freedom, the vibrational frequencies of these two species share similarities, so one would expect some parallels between the intramolecular dynamics of these two species. More specifically, slow energy transfer between the high frequency and low frequency modes.

The first part of this dissertation is tied to the simplified reaction shown in Eq. 2, namely how does the unimolecular reaction of HO_2 occur? Are the dynamics in agreement with statistical expectations, with fast energy transfer among the vibrational

modes? What role does isomerization play in the energy transfer? Are there signatures of mode selectivity in the unimolecular dissociation of the radical? These questions are the subject of the research in Chapter III of this dissertation.

The second part of this dissertation is devoted to the study of the collisional deactivation of the vibrationally excited species shown in Eq. 1. The isolated binary collision approximation (IBC)[17] is a common assumption made in modeling the deactivating effect of collisions on a vibrationally excited species. Under this approximation, the time-dependent deactivation process is treated as a series of uncorrelated collisions with the bath gas. This simplified model allows for the calculation of the relaxation time of a solute from the product of an energy transference probability with a solute-bath gas collision frequency. The energy transference probability is typically based on gas-phase results, and the collision frequency is taken from a hard-sphere model. A general result of the IBC approximation is a linear dependence of the solute relaxation time constants with the bath density. Evidence for the general applicability of IBC is mixed, with favorable agreement for some systems,[18] whereas anomalous behavior is seen in others.[19] Given the importance of HO_2 in pressure-dependent combustion, we investigate the relaxation of a vibrationally excited radical in a dense Ar bath. We also examine the applicability of the IBC approximation under conditions of extreme pressure. These investigations are the focus of chapter IV.

The development of the code used in simulating HO_2 led to preliminary work on general methods and considerations of molecular dynamics (MD). This work does not directly fit in other chapters, but it was useful in motivating the work on HO_2 and is discussed in chapter II. The conclusions of the dissertation are given in chapter V.

II. Considerations in Trajectory Calculations

While the methods in an MD simulation can become quite involved, the technique can be broken into a simple set of steps: (1) definition of the potential energy surface; (2) selection of initial conditions; (3) integrating the equations of motion; (4) sampling and analysis of physical properties and end-test criteria. These steps are shown below for the simple case of trajectories integrated on the Hénon-Heiles[20] potential. Extension of these steps to more complicated simulations is also discussed. The discussion of this chapter sets the stage for the research conducted in completing this dissertation.

A. The Hénon-Heiles Hamiltonian: An Illustrative Example

Defining a potential energy surface (PES) is the first step in an MD simulation. The purpose of the PES is to represent the interactions of the nuclei that compose the chemical species being studied. Originally the Hénon-Heiles potential was developed as a model for understanding cosmological motion,[20] but the simple form and complex dynamics of this potential has resulted in its use in understanding chemical dynamics.[21] The Hénon-Heiles potential is the following:

$$V(x,y) = \frac{1}{2}(x^2 + y^2) + x^2 y - \frac{1}{3}y^3, \qquad (3)$$

where x and y are Cartesian coordinates. This potential is two harmonic oscillators with cubic anharmonic coupling and anharmonicity in the y coordinate. An illustration of the potential can be seen in Fig. 1. The minimum of the potential is the central blue region. The coloration of the figure changes with progressively higher potential energy from green to yellow and finally red. The extremely high-energy regions, which are of little dynamical importance, are shown as white. The potential has three-fold symmetry with

the exit channels diverging to infinity both spatially and energetically. The threshold for a dissociative trajectory is ≈1/6 energy units and trajectories with energy beneath that energy threshold display behavior characteristics that range from quasi-periodic to irregular.

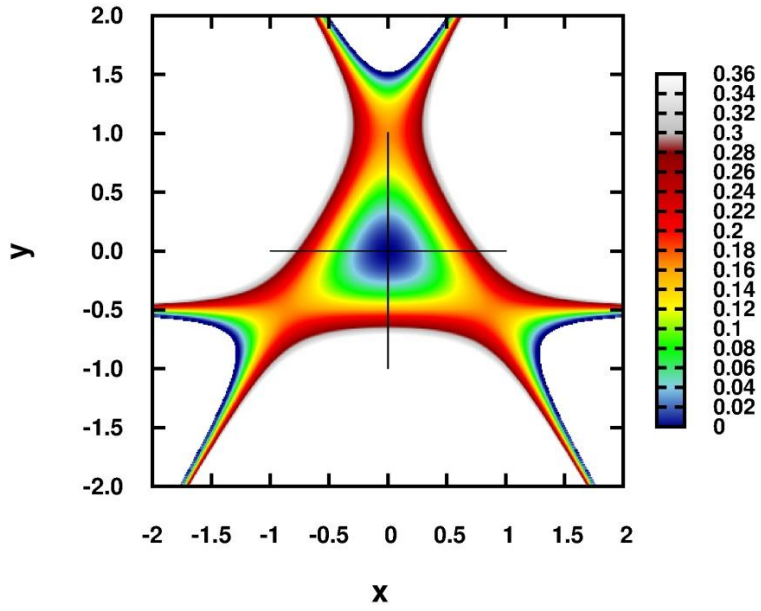

Figure 1 Hénon-Heiles potential plotted in Cartesian coordinates. The black lines indicate planes of intersection that were used in calculating surfaces-of-section.

The initial conditions for these illustrative tests were selected with a simple Monte Carlo scheme. The first step involves selecting two pseudo-random numbers uniformly distributed on [-1,1] as the initial-Cartesian coordinates. The potential is evaluated at these points to determine if they lie below the specified total energy. If the potential energy is above the specified threshold, the points are then discarded and a new set of points is sampled; this process is repeated until the energy criterion is satisfied. Once the energy criterion is met, then a set of conjugate momenta is selected that satisfies $T = H\text{-}V$ where T is the kinetic energy, H is the total energy and V is the potential. The kinetic

energy is then divided between the two oscillators using $P_x = \sqrt{2T\zeta}$ and $P_y = \sqrt{2T(1-\zeta)}$, where ζ is a pseudo-random number uniformly distributed on [0,1], P_x is the momentum in the x direction and P_y is the momentum in the y direction. The signs of the momenta are randomized and a trajectory is initiated. This trajectory is then integrated for some desired length of time, or until a termination criterion, such as dissociation, is satisfied. The trajectory terminates when a predefined time or event occurs and the initial conditions of the next trajectory are selected. The process is repeated until a group, or ensemble, of trajectories is completed. During the simulation, the trajectory can be analyzed on the fly with ensemble averages being calculated at the end of the simulation, or phase points can be stored for subsequent post-simulation analysis. Collecting the full phase space information has the advantage that new analyses can be considered without rerunning trajectories. The main disadvantage of storing the entire phase space information of a simulation is the dependence on having sufficient disk space available and preventing data corruption. The on-the-fly analysis has the advantage of requiring minimal disk space and data corruption issues, but new analysis can require rerunning simulations. The complex dynamics of the Hénon-Heiles potential has resulted in its extensive study, particularly with regard to the transition from quasi-periodic dynamics to irregular dynamics where the phase space of the system is explored in a much more chaotic manner. Figure 2 contains two representative trajectories which are representative of quasi-periodic (frame a) and irregular dynamics (frame b).

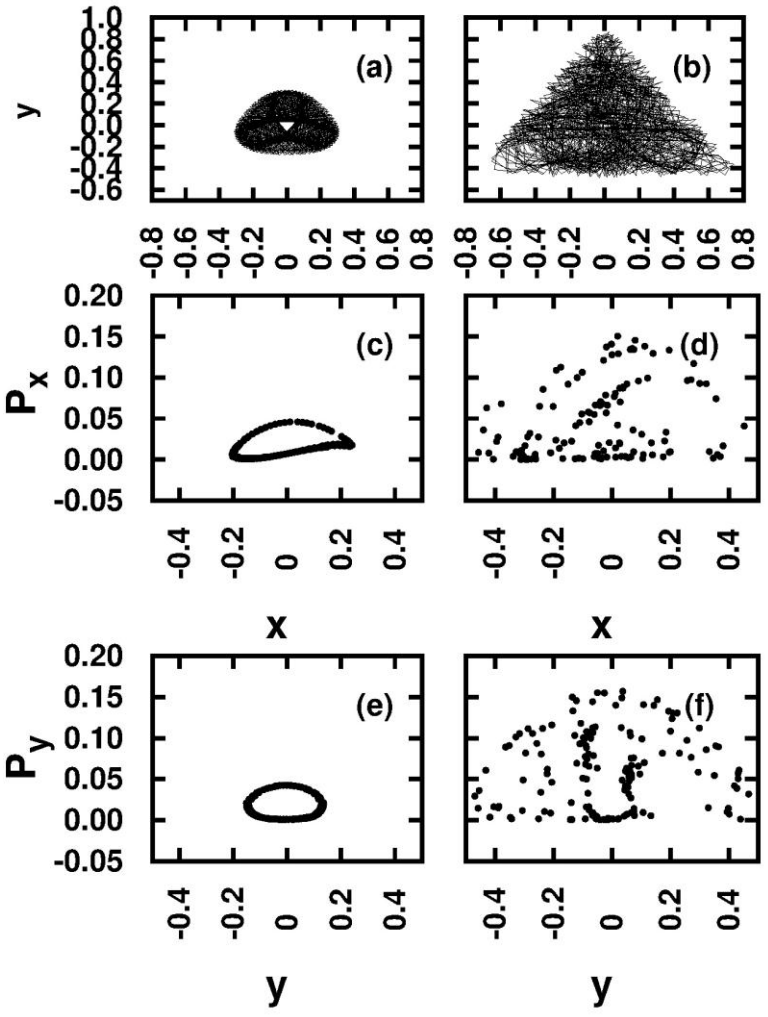

Figure 2. Representative trajectories of quasi-periodic and irregular trajectories: (a) Quasi-periodic trajectory with a total energy of 0.05 energy units; (b) irregular trajectory with a total energy of 0.16 energy units; (c) and (d) the X surface-of-section; (e) and (f) the Y surface-of-section.

Now imagine attempting to classify an ensemble of the trajectories. Examining plots of individual trajectories would be inefficient, and understanding the behavior of the ensemble would be difficult. A slight change in perspective can provide some clarity shown, as in Fig. 2c, 2d, 2e and 2f by using Poincaré surfaces-of-section (SOS). An SOS plot is calculated by first selecting a plane defined by one of the coordinates in configuration space and recording the second coordinate and conjugate momentum when

a trajectory crosses the surface in one direction. A surface-of-section is a common mapping technique[22] in the analysis of dynamical systems with low dimensionality. Higher dimensional systems often require more involved analysis.[13a] An SOS plot provides a striking means of showing recurrence, or periodicity, in an group of overlapping, complicated trajectories. Figure 3 shows how the surfaces-of-section for an ensemble of trajectories change as the energy of the system increases. As the energy of the system increases, the amount of accessible phase space volume grows and the regions of structure begin to disappear as the trajectories become more irregular.

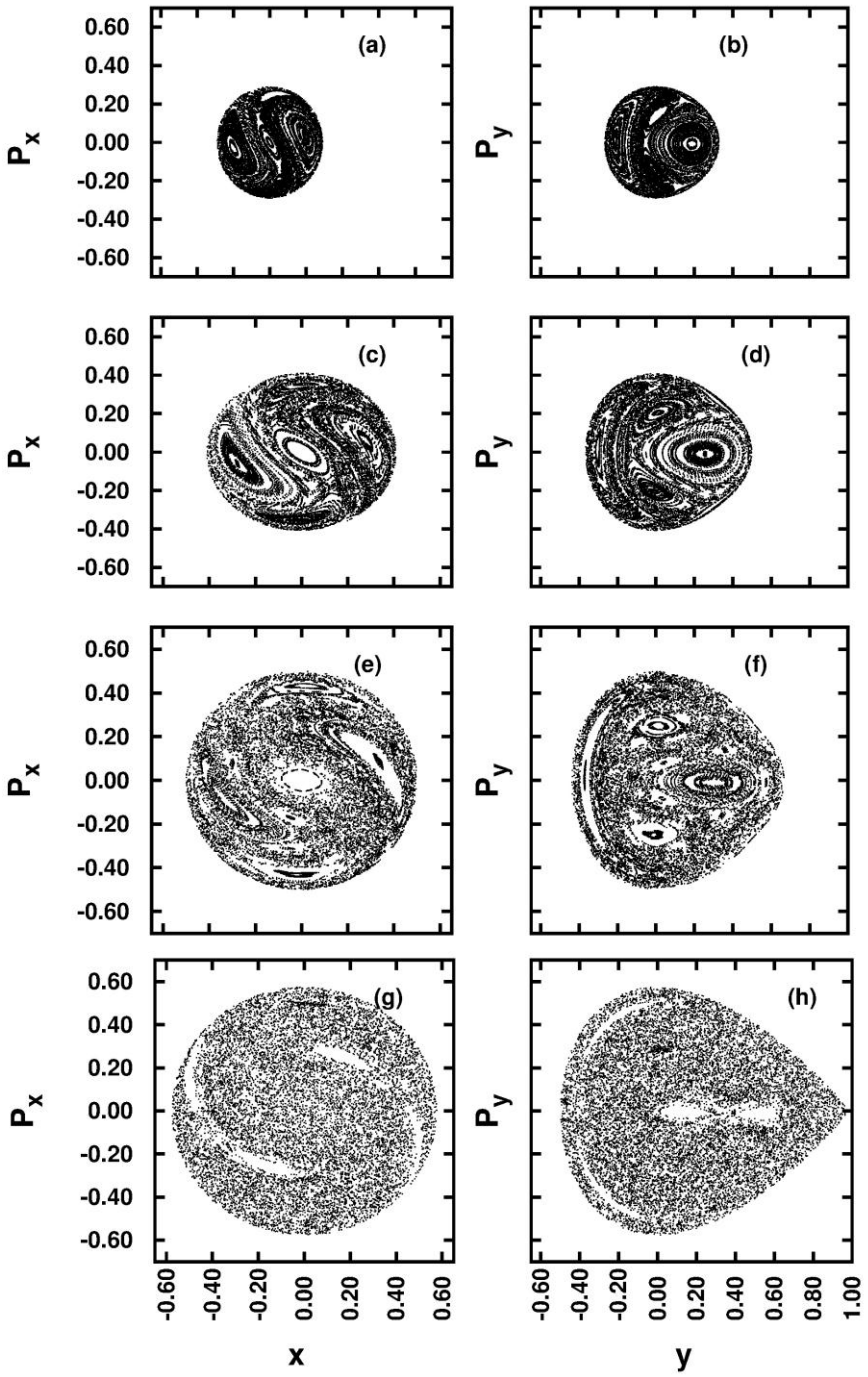

Figure 3. Surfaces-of-section from dynamics on the Hénon-Heiles potential that show the progression of phase space expansion and exploration with increasing energy. The trajectories were integrated for 1000 time units. Each frame is the result of intersections calculated from ensembles of 100 trajectories per frame. The planes of intersection are defined in Fig. 1: (a) and (b) the total energy is 0.042; (c) and (d) the total energy is 0.084; (e) and (f) the total energy is 0.125; (g) and (h) the total energy is 0.166.

B. Potential Energy Surfaces

While a full quantum mechanical solution for the motion of both the electrons and the nuclei is desired, it is often cost prohibitive. But, to a good approximation, an acceptable solution can often be obtained. The good approximation is otherwise known as the Born-Oppenheimer approximation,[23] where the general idea is that the motion of the electrons can be separated from the motion of the nuclei by virtue of the vastly differing masses of these two subatomic particles. In other words, the motion of the electrons is so fast that one can conceive the electrons instantaneously adjusting for the motion of the nuclei, and that the nuclei move on a surface that is defined by energies obtained by solving the electronic structure of the system. However, given the computational cost of electronic structure calculations, it is common practice to construct model systems with analytic functions describing the interactions between the nuclei.[24] These analytic functions can be parameterized to reflect the known information on the chemical system, such as the thermochemistry and vibrational frequencies of the system.

The analytic functions parameterized with experimental and *ab initio* data may not be sufficient to represent the complex topography of the true PES. But there are two different means of obtaining a more realistic PES. With the improvement in computing power and electronic structure codes, there has been development of a method known as "Direct Dynamics."[25] With Direct Dynamics, the electronic structure problem is solved on the fly during a trajectory. The primary issue with this technique is the sheer computational cost of solving the electronic structure problem for tens of thousands of force evaluations in a single trajectory. This cost is compounded by the need to simulate hundreds, if not thousands, of trajectories to obtain converged averages. The alternative

to direct dynamics is to save the output of electronic structure calculations and interpolate it using a flexible function or polynomial.[26] However, interpolation of low-symmetry systems that contain four or more atoms suffers from the "curse of dimensionality,"[27] in that a large number of data points will be required to fit a high-dimension PES accurately. Another issue with interpolation is that the computational cost grows with the complexity of the function being used to fit the surface.[28]

In the context of this dissertation and the HO_2 radical, we are fortunate to have access to interpolated potentials that were developed by others.[54,56] We use these PESs to study the phenomena in which we are interested, which are the dynamics and reactivity of the HO_2 radical. The description of the potential energy surfaces of this radical used in this dissertation is provided in Ch. III.

C. Selection of Initial Conditions

The selection of initial conditions for trajectories is very much dependent on the statistical ensemble and what one wishes to learn from the trajectories. Whatever the phenomenon of interest, the Monte Carlo method[29,30,32] is a common means for selecting initial conditions Typically, one uses a pseudo-random number generator to select random numbers distributed on an interval between 0 and 1. These numbers can then be weighted, or scaled, to the variables needed to describe the initial state of the system. For NPT (constant temperature, pressure, and number of particles), and NVT (constant temperature, volume, and number of particles) simulations,[30] the initial conditions generally consist of selecting initial coordinates and momenta and then running a sufficiently long trajectory with a thermostat or barostat[30] to obtain the desired physical state. The sort of initial conditions that are of greatest use in studying unimolecular

dynamics are ones that correspond to the NVE ensemble (constant energy, volume and number of particles). This ensemble is attractive because there are general conservation principles: energy, total angular momentum, and linear momentum, which can be used to assess the accuracy of the simulation. But most important, the equations of motion are not modified as they would be with a thermostat or a barostat, so in the classical limit where quantum effects are assumed to be minimal, a trajectory calculated on an accurate PES should reproduce the dynamics, and the ensemble averages calculated by trajectories would agree with the expectation values derived from quantum mechanics. There has been considerable investment of time and effort in the development of the algorithms used to select initial conditions that correspond to the NVE ensemble, so we will focus on the ones most relevant to this study.

1. Mode-Specific Initial Conditions

The ability to localize energy in a particular degree of freedom is of interest inasmuch as it provides a means of studying how energy relaxes amongst the various degrees of freedom. These methods have been discussed in great detail in numerous reviews[24] on classical simulations and are only briefly described here. The simplest form of approximating the vibrational degrees of freedom is to picture them as normal modes. The normal mode approximation provides a general means of separating the vibrational motion into discrete parts. However, this method does have limitations: the vibrational motion is assumed to be harmonic and there is no accounting for the anharmonicity of the PES. The form of a normal mode is

$$q_i(t) = A_i \cos(\lambda^{1/2} t + \phi), \qquad (4)$$

where q_i is the i^{th} normal mode, A_i is the amplitude, λ is the force constant and ϕ is the phase of the oscillator. The first step in setting the mode-specific initial conditions is to solve the eigenvalue equation of the normal modes for the eigenvalues and vectors. This is done by calculating the Hessian, or second derivative matrix of the potential at a stationary point on the PES, such as a minimum on the surface. Detailed discussions of normal mode analysis and spectroscopy can be found in a classic text.[31] The eigenvalue equation is then solved, typically with readily available codes.[32] The eigenvector matrix is used in the linear transformation between normal coordinates and Cartesian coordinates during the selection of initial conditions, but can also find use in the analysis of the trajectory. The selection of initial conditions begins by calculating the total energy summed from the individual mode contributions. Then the phase of each oscillator is sampled independently using

$$q = q_e - (q_e - q_t)\sin(\pi/2 + \pi\zeta), \qquad (5)$$

where q_e is the equilibrium value of the normal mode and q_t is the inner turning point and ζ is a pseudo-random number. The potential energy of the surface is then calculated with the sampled phase and is accepted if the potential energy of the displacement is less than the specified energy of the mode. If the potential energy is greater than the specified mode energy then displacement is rejected and the phase is resample until an acceptable displacement is found. After independently sampling the phase of all of the modes, the normal mode velocities and displacements are added to the stationary point at which the normal mode analysis was done. The resultant sum of the coordinate and momentum vectors may result in a non-zero angular momentum, which Hase *et al.*[33] showed can be iteratively removed to enforce a requirement of zero angular momentum if it is desired.

The use of normal mode excitations has found considerable use in studying IVR. A complementary method of localizing energy in a particular mode, similar to normal mode excitation can be done using a local mode model,[24] where the excitation energy is projected along a bond vector with the assumption of the potential interaction being harmonic, or Morse-like. The advantage of a local mode excitation is that the anharmonicity of the potential in the local mode is taken into account in the selection of the initial conditions.

2. Statistical Initial Conditions

The limitation of assuming a normal or local mode picture has led to development of alternative means of selecting initial conditions for the microcanonical ensemble. The question of efficient and accurate selection of initial conditions for the microcanonical ensemble has been extensively studied by others.[34,35] The initial conditions of the HO_2 radical were selected using *efficient microcanonical sampling* (EMS) with no restriction to angular momentum or with the angular momentum restricted to zero. The procedures consists of a random walk where the Cartesian coordinates of the radical are randomly changed

$$q_{new} = q_{old} + \Delta(\zeta - 0.5), \qquad (6)$$

where q_{new}, and q_{old} are the "old" and "new" x, y, or z component of the Cartesian coordinates of the atoms and ζ is a pseudo-random number on the range 0 to 1 and Δ is a maximum displacement. The acceptance of a new displacement with no restriction to angular momenta is assigned the following[34(b)] weight

$$W(E,J) = [E - V(q)]^{(3N-5)/2}, \qquad (7)$$

and the corresponding weight for J = 0 is[34(a)]

$$W(E,J) = \sqrt{\frac{1}{I_A I_B I_C}}[E - V(q)]^{(3N-8)/2}, \qquad (8)$$

where I_a, I_b, I_c are the principal moments of inertia, E is the desired energy, V is the current potential energy, and N is the number of atoms in the system. A trial move is accepted if the weight of the new state is greater than weight of the current configuration. If the trial weight is less than or equal to the current weight, then a ratio of the trial weight and the current weight is compared to a pseudo-random number sampled from a uniform distribution of [0,1]. If the ratio of weights is greater than the selected pseudo-random number the trial move is then accepted; otherwise, it is rejected and a new trial displacement is sampled. At the end of the random walk, a set of velocities is selected and scaled to ensure that the desired initial internal energy E_D is obtained. The momentum scaling is

$$P_N = P_O \sqrt{\frac{E_D - V}{H - V}}, \qquad (9)$$

where H is the Hamiltonian, and P_O and P_N are, respectively, the old and new x, y, or z momenta of the atoms in the radical. The final geometric configuration of system at the end of the Markov walk was used as the starting point for subsequent random walks in the ensemble.

D. Integration of the equations of motion

After selecting the initial conditions, the next task is integration of the equations of motion. Typically a closed form solution to the equations of motion does not exist and a numerical solution is required. Numerical integration is a rich and varied field and has

been deeply studied in the context of MD simulations.[36,37] While no development of integration methods occurred in this dissertation, coding and testing of existing algorithms did happen, so it is worthwhile to consider the range of integration algorithms available and the respective strengths and weakness of these algorithms.

In MD simulations, the equations of motion solved are typically Hamilton's equations since these equations are valid in any coordinate frame and the solving a set of first-order equations is generally less complicated than solving a set of second-order equations. Hamilton's equations are the following

$$\dot{p} = -\frac{dH}{dq} \tag{10}$$

and

$$\dot{q} = \frac{dH}{dp}, \tag{11}$$

where $\dot{p}$ and $\dot{q}$ are the time derivatives of the momenta and coordinates, respectively, and H is the Hamiltonian, which is a function of p and q. Typically, the integration coordinates are selected to be in the fixed lab-frame Cartesian coordinates, a choice that simplifies the expression of the kinetic energy. This expression can be complicated if the system is described in terms of in generalized coordinates. The issue of the potential energy being a function of internal coordinates is dealt with by using the chain rule to transform the gradients from internal coordinates to the Cartesian, fixed lab-frame coordinates. The result is a set of 6N first-order equations that must be solved to propagate the trajectory.

There are numerous integration schemes[37] that have been devised to solve sets of differential equations. These schemes are based on finite steps along the function or system of functions that is being integrated. These finite steps are used to extrapolate to the next integration point. The finite nature of the integration process means that a stable integration in MD is determined by having a smooth differentiable potential, since the gradient of potential is used in Eq. (10) to determine how the momentum changes. Changes in the momenta in turn determine the next displacement in configuration space at which the potential and gradient are evaluated, and the gradient in turn affects the momenta, and so the process repeats. Continuing this stepwise process is known as integrating a trajectory. The largest cost of an MD simulation is typically found in the evaluation of the forces, which can become laborious if the evaluation is done by finite difference or if the PES is complex, as in direct dynamics or interpolated surfaces. Even a large number of pairwise interactions to be evaluated can result in unfavorable scaling of the computational cost of a problem.[30] Ultimately, this means that minimizing the number or cost of gradient evaluations per integration step leads to a more efficient simulation. A simple means of decreasing the computational cost of a trajectory is to use a larger integration step size, so that fewer integration steps are required to simulate some time interval; however, but care must be taken because larger step sizes can increase the effect of truncation errors .

The original simulation code (GENDYN),[38] which was further developed in this research, had the 4^{th} order Runge-Kutta-Gill[39] (RKG4) algorithm as the standard integration algorithm. This method is attractive because of the relatively high accuracy of the method, $O(h^4)$, and is self-starting in that the algorithm does not require multiple

forward and backward integration steps to calculate the next step. However, this integrator requires four gradient evaluations for a single time step, so direct dynamics or some other costly source for gradient information becomes cost prohibitive with increased integration time or system size.

Numerical errors in integration can easily accumulate and lead to instability in the integration. Pritchard[40] discussed the effects of integration step size and finite precision on the reproducibility of trajectories on various machines. One of the findings of the study was that while acceptable agreement of ensemble averages across the various machines was found, results of individual trajectories could vary substantially due to numerical errors. Care must be taken in considering the errors of finite mathematics that can creep into a simulation. A simple illustration of the issue of cumulative error can be seen in Fig. 3. These are trajectories integrated on the Hénon-Heiles potential with a total energy of 0.0125 using two different integration methods: RKG4 and velocity Verlet[41] with the same integration step size of 0.1. The total integration time was 1,000,000 time units. All of the trajectories were started at the same point in phase space. On a shorter timescale, frames (a) and (b) show that the energy drift for the velocity Verlet and RKG4 integrators is very small for the entire integration time. However, as the RKG4 trajectory is integrated for a much longer time, there is a progressive deterioration of the energy conservation. This deterioration is also reflected in the surfaces-of-section plotted in frames (e-h) for the long time trajectories, where the progressive loss of energy conservation results in the RKG4 trajectory exploring different regions of phase space. The surfaces-of-section were collected over the entire integration time. Reduction of the

integration step size in the case of RKG4 by an order of magnitude results in improved energy conservation, but this comes with the additional cost of more force evaluations.

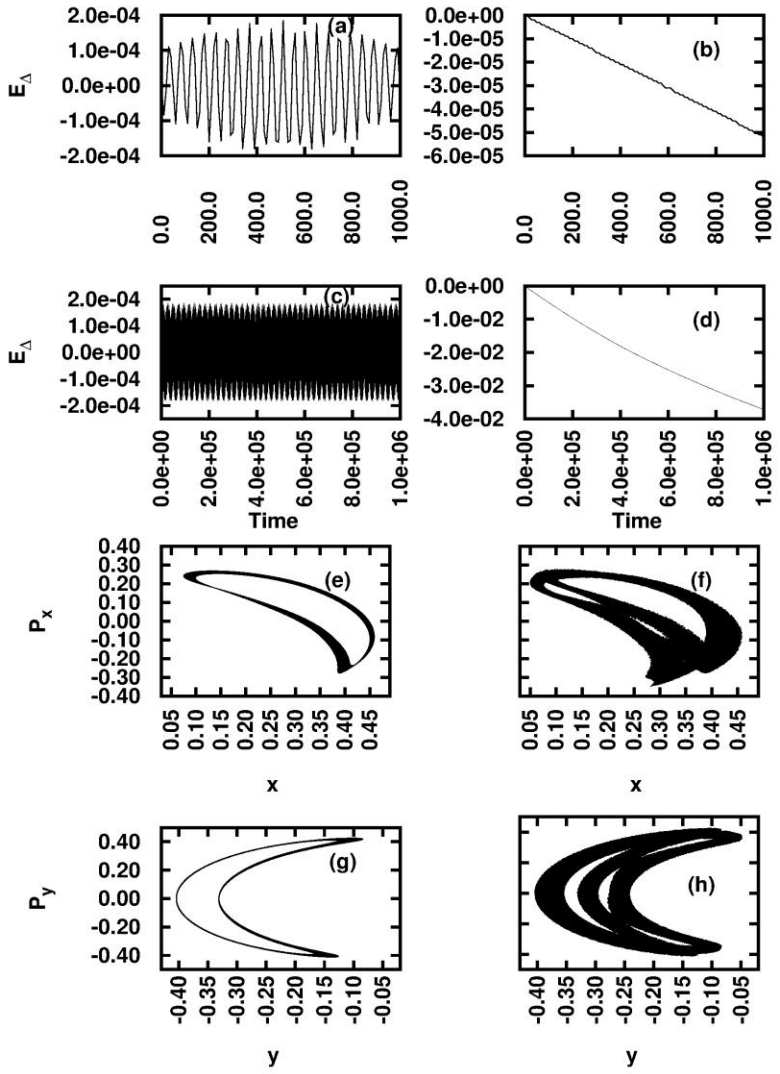

Figure 4. Plots of integration accuracy tests for the velocity Verlet integrator and RKG with identical step sizes of 0.1: (a) Energy drift of a velocity Verlet trajectory, (b) same as (a) except for a RKG trajectory; (c) Energy drift of a velocity Verlet trajectory plotted in (a) for longer timeframe, (d) same as (c) except for a RKG trajectory; (e) Surfaces-of-section for the X, P_x subspace from a velocity Verlet trajectory, (f) same as (e) except for RKG trajectory; (g) Surfaces-of-section for the Y, P_y subspace from a velocity Verlet trajectory; (h) same as (g) except from a RKG trajectory.

The potential issue of loss of energy conservation does not mean that the RKG integrator is not useful, since the order of accuracy for short integrator times is superior to

that of the Verlet algorithm. The stability of the Verlet integration is due to it being part of a class of integrators known as symplectic integrators. A symplectic integrator is one that preserves the volume of phase space and the constants of motion of the system.[42] Gray et al.[36(a)] tested several symplectic integrators and concluded that there is not necessarily one integrator that is the best for all applications.

The inefficient scaling of the RKG4 with system size and force evaluations motivated the coding of two additional integrators into GENDYN: one integrator being the Adams-Moulton Predictor-Corrector algorithm[43] and the other the velocity Verlet. Each of these integration methods was coded for a specific use. The predictor-corrector was coded since it has the same order of accuracy as RKG4, which is important for detailed energy transfer studies, but only requires one gradient evaluation per integration step as opposed to four. The velocity Verlet was coded for larger systems and longer timescales where stable, efficient long time integration becomes important.

E. Sampling and Analysis

The majority of the analysis techniques are discussed in subsequent chapters in the context of the research topic. However, there are a couple of issues that are worth discussing, but do not readily fit in the other chapters of this dissertation.

Any number of properties can be calculated from a classical trajectory simulation, but there is an important caveat that must considered when interpreting simulation results. Individual trajectories can provide mechanistic details, but the meaningful result is the ensemble average. The mean of the ensemble average is extremely important when considering the correspondence between classical and quantum mechanics.[44] Sewell

et al.[45] and Guo *et al.*[46] both studied the issue of zero-point energy flow and showed that both active and passive constraints on zero point energy result in aphysical dynamics. Proton tunneling[47] can also be an important quantum effect to consider when studying the dynamics of HO_2 in the case of isomerization. A detailed study of this phenomenon is beyond the scope of the research in this dissertation, and thus such a study is outlined as a proposed future work at the end of chapter III.

Error estimation in trajectory studies can be done with two different approaches. The first approach is to averaging across multiple independent groups of trajectories. This approach is time and labor intensive, and fortunately, the second way is more tractable. The more tractable approach is known as bootstrap estimation, which was originally proposed by Efron.[48] The bootstrap procedure consists of randomly resampling the data and generating bootstrap data sets, or resampled data sets. The random resampling is done through use of a pseudo-random number generator. The resampled data sets are then subject to the same analysis as the parent data and resampled parameters are then used to calculate statistics that can be used to describe the parent data set.

We applied the bootstrap method in resampling of trajectory indices to generate bootstrapped ensembles of trajectories for analysis. Our application of the bootstrap method in both Chs. III and IV differed from the original bootstrap method. The first difference is that we chose to have the bootstrapped ensembles of trajectories be composed of fewer trajectories than the parent trajectory ensemble. The traditional application of the bootstrap involves having the number of points in each resampled data set equal to the number of points in the parent data set. It is well known that the magnitude of the statistical error of an average calculated in a trajectory simulation is ≈

$1/\sqrt{n}$, where n is the number of trajectories in a simulation. This means that bootstrapped data composed of smaller subsets of the parent data should provide an upper estimate to the error of the simulation.

The second difference, which only applies to Ch. IV, is that the bootstrap was modified so resampling was done without replacement, to prevent duplicate inclusion of a single-trajectory index in an individual, bootstrapped data set. Although, it is possible that a trajectory index could have been included in multiple, independent bootstrapped data sets. This modification to the resampling was done because a trajectory index is just a placeholder for an entire, correlated time history. However, it is not completely clear to us if resampling of smaller data subsets without replacement is equivalent to the original bootstrap method; consequently, we treat our error bars, in Ch IV, as rough-upper estimate of the variance in the data.

III. Dynamics and Unimolecular Dissociation of Hydrogen Peroxyl Radical

A. Introduction

1. Literature

The hydrogen peroxyl radical HO_2 is important in free radical chain propagation and termination in combustion reactions.[49] Over the past quarter century the bimolecular reactions

$$H + O_2 \rightarrow HO + O \quad (12)$$

$$HO + O \rightarrow H + O_2 \quad (13)$$

and associated unimolecular dissociation reactions

$$HO_2^* \rightarrow H + O_2, \quad (14)$$

$$HO_2^* \rightarrow HO + O \quad (15)$$

have been the subjects of a number of experimental and theoretical studies. An important part of these studies has been potential energy surface (PES) development using *ab initio* data,[50,51,52,53,54,55,56] and the use of these PESs for rate calculations. Brandão *et al.*[57] reviewed these HO_2 PESs with the exception of the most recent one by Li *et al.*[56]

We have used classical trajectories to study the fundamental reaction dynamics of HO_2 because two new PESs are available, both based on accurate, state-of-the-art electronic structure theory. The most recent PES, by Li *et al*., is an *interpolating moving least squares* (IMLS)[28] polynomial surface that constructed from *ab initio* icMRCI+Q[58,59,60] results with CBS extrapolation.[93] The second PES is the third member

of a progression of 3-D cubic-spline-fitted surfaces started by Xu, Xie, Zhang, Lin, and Guo[53-,54,55,56] (XXZLG). This PES[55] is based on ≈18,000 icMRCI+Q calculations, but without CBS extrapolation. It best represented the experimental vibrational spectroscopy of the PESs discussed in the 2009 Brandão *et al.*[57] review. We contrast the results calculated using these recent PESs with those obtained by using the semi-empirical *double many-body expansion* (DMBE-IV) PES developed by Pastrana *et al*.[50]

The DMBE-IV PES has been used in many studies of the reactions dynamics of HO_2. It was built with data from several sources, including the *ab initio* data reported by Melius and Blint[61] and Walch *et al.*[62], with parameters adjusted to match experimentally determined force constants.[63] The *ab initio* data from Walch *et al.*[62] for the O + OH asymptote were semi-empirically[64] adjusted for electron correlation. The method used to construct the DMBE-IV PES has been discussed in detail elsewhere.[65] Comparisons of different regions of the PES to higher quality electronic structure calculations[51,52] than used in its construction have shown significant differences, and comparisons to spectroscopic[66] and kinetics[67,68] experiments show some of the limitations of this surface in accurately describing this radical. Several classical trajectory studies[69,70] and quantum dynamical studies[69,71,72] of microcanonical unimolecular decay or bimolecular reaction dynamics on this PES have shown strong mixing among the modes, and reaction kinetics qualitatively consistent with statistical theories. However, a trajectory study of Miller[73] using the Melius and Blint[61] PES and a follow-up trajectory study of Miller and Garrett[74] using the DMBE IV showed that the HO_2* complexes formed from H + O_2 or OH + O have biased decay back to the reactants. This result implies the collision complex retains some memory of its origin. Also, Duchovic and Parker[75] inferred from a classical

trajectory study of $H + O_2$ that IVR in HO_2* is slow enough to cause non-statistical unimolecular decay, an observation made earlier by Lemon and Hase[76] based on an empirical PES. Marques and Varandas[70] examined mode-specific unimolecular dissociation at constant energy and found that the energy decay rate constants were only weakly dependent on the mode initially excited. However, the results were reported at insufficient resolution to compare to the modest effects Miller and Garrett[74] found. The finding of these studies suggest that mode mixing is strong enough on the DMBE-IV PES to create an irregular spectrum of quantum mechanical metastable states and a single time scale of unimolecular decay, but not strong enough to completely erase all memory of the initial conditions under which HO_2* is formed.

Studies on the XXZLG PES[53,54,55] show that the modes of HO_2 are more quasi-periodic and decoupled than the modes predicted using the DMBE-IV PES. The vibrational spectrum for the bound states on the XXZLG calculated by Lin *et al.*[77] showed a reduced density of states supported on the surface, with the distribution of states being an intermediate case of regular and irregular level spacing. They found that the statistical theory rate overestimated the average quantum mechanical rate, and posited that the result is a consequence of slow IVR. Xu *et al.*[78] found regularities in the vibrational spectrum of the radical even at energies near the dissociation threshold indicative of weak modal coupling, which they suggested would strongly affect unimolecular dissociation of HO_2. They assigned pure O–O vibrational overtones up to 18 quanta and to within $\approx$100 cm^{-1} of the dissociation limit. Pure O–H vibrational overtones could be assigned up to 4 quanta, but at higher energies isomerization appears to enhance the interaction between the OH stretching and OOH bending motions, thus

ending the overtone progression. Xu *et al.* also suggested that resonances between O-O and O-H could also play a role in energy transfer[13(a)] between these two modes. The results of three different quantum dynamics studies[79-,80,81] on XXZLG for the bimolecular reactions (1a) and (1b) show significant non-statistical effects in the differential cross sections, trace the contributions from individual and assignable HO_2* resonances to reaction cross sections and display significant differences with quantum scattering results on DMBE-IV. Quasiclassical trajectory calculations on the XXZLG PES have been carried out for reactions (1a) and (1b) by Lendvay *et al.*[82] and show that the lifetimes of the collision complex formed in reaction (1a) display a bi-exponential distribution. For reaction (1b), Jorfi *et al*.[83] found evidence of slow energy transfer between the O–H and O–O bonds, resulting in a non-statistically large probability of HO_2* dissociating back to the H + O_2 reactants. All of these studies suggest that XXZLG dynamics has much weaker mode coupling than DMBE-IV dynamics, and the result is much more salient non-statistical behavior in bimolecular reactions. Despite the high-quality *ab initio* foundation of XXZLG, exact quantum dynamical rate constants[81] on XXZLG for the O + OH reaction (1b) agree with experiment within a factor of two. Likely sources of the discrepancy include experimental error, limitations of the PES, and the possible relevance[84] of multistate non-adiabatic dynamics.

The possible involvement of electronically excited states and the need for more accurate electronic structure methods led to the calculations of new sets of PESs for the HO_2 ground- and first-excited states by Li *et al*.[56] Among those PESs is the ground state IMLS PES that is further studied in this paper. The electronic structure theory used to generate the IMLS PES includes extrapolation to estimate the CBS limit. While also

interpolative, IMLS fitting is a different kind of representation than the splines used in XXZLG and is capable of high accuracy with relatively few points. However, while containing the reaction path for dissociation to H + O_2, the current IMLS PES is restricted to coordinate ranges that do not include the higher energy O + OH asymptote.

This brief survey of the literature shows that earlier work placed some emphasis on the extent of mode coupling in HO_2*. Despite that emphasis, lower-energy processes, such as IVR and isomerization, which can be sensitive to mode coupling, have not been extensively studied on any of the three surfaces. If lower-energy processes display different results on the different PESs, perhaps it would be possible to identify specific PES features that underpin the dynamical differences. For the higher-energy process of unimolecular decay, mode-specificity has only been studied on the DMBE-IV PES where mode coupling is thought to be quite strong and only modest mode-specific effects have been identified. Based on previous IVR studies,[24(a),108] mode-specific effects in unimolecular decay are expected to be more significant for the XXZLG PES (due apparently to weaker mode coupling). No dynamics studies have been carried out using the IMLS PES.

In this study we investigate, using classical trajectories, the intramolecular dynamics and isomerization on all three PESs and the unimolecular dissociation of $HO_2 \rightarrow H + O_2$ on the XXZLG and DMBE-IV. This chapter is organized as follows: Descriptions of the characteristics of the PESs are given in Sec. A.2, the computational methods are described in Sec. B, results and discussion are given in Sec. C, and the conclusions are given in Sec. D. Potential future studies are proposed in Sec. E.

2. Potential Energy Surfaces

a. The XXZLG PES

Four different spline-based versions of the XXZLG PES have been produced by Xie and coworkers. The first two[53,54] are based on ≈15,000 *ab initio* data points computed at the level with the valence electrons correlated in the icMRCI+Q/AVQZ calculations. The active space for the CASSCF reference (9e, 7o) constrains the oxygen 1*s* and 2*s* orbitals to be doubly occupied and includes two ^{2}A" states with equal weights. Later in 2007 the data set was augmented by ≈3,000 points for large O–O separations (as encountered in the O + OH channel), leading to the third version of the XXZLG PES.[55] Finally, in 2010 as part of a study of the lowest ^{2}A' excited state, a further update to the ground state data was also reported.[56] The new *ab initio* data were computed using a full valence active space (13e, 9o) in the two-state CASSCF reference and the core electrons were also correlated in the subsequent icMRCI+Q calculations. Including core electron correlation and the full-valence active space was reported to improve the thermochemistry slightly with respect to experiment.[56] For the ground state, these improved *ab initio* calculations were carried out at ≈4,000 points to obtain their difference with respect to the previous XXZLG PES. This difference was fit with a spline which when added to the previous XXZLG PES constitutes the fourth version of the XXZLG PES. The version of the XXZLG PES used in this study is the third version[85] developed in 2007 from ≈18,000 *ab initio* points.[55]

An examination of the isomerization saddle point identified a minor seam in the XXZLG PES that results in a discontinuous force for trajectories traversing the O–O

perpendicular symmetry plane. This seam occurs because XXZLG uses only the shorter of the two O-H distances. The use of the shorter O-H distance guarantees a continuous value across the symmetry plane but not a continuous gradient. We smoothed the seam using symmetrization[86,87] of the PES in the region near the symmetry plane. This smoothed surface has the form

$$V_{sym} = V(\mathrm{H-O_aO_b})S(\Delta) + V(\mathrm{H-O_bO_a})(1 - S(\Delta)) \quad (16)$$

where $S(\Delta)$ is a smoothly varying second-order switch of the following form

$$S(\Delta) = \min[1, \max[0, 1- (10g(\Delta)^3 - 15g(\Delta)^4 + 6g(\Delta)^5)]] \quad (17)$$

where

$$g(\Delta) = (\Delta - \Delta_l)(\Delta - \Delta_u)^{-1} \quad (18)$$

where the progress variable $\Delta = R_{\mathrm{H\text{-}Oa}} - R_{\mathrm{H\text{-}Ob}}$ with limits $\Delta_u = 0.2$ Å and $\Delta_l = -0.2$ Å. The value, gradient, and Hessian of $S(\Delta)$ are zero at both limits, making the V_{sym} patch smoothly join the unmodified XXZLG PES outside of ≈0.2 Å from the O–O perpendicular bisector plane. Note also that precisely at the symmetry plane, the patched surface is exactly equal to the original XXZLG PES. Reproducing the value of the original XXZLG surface at the symmetry plane means that the isomerization saddle point energy, geometry, and vibrational frequencies are exactly the same on the original and corrected XXZLG PES except for the imaginary frequency, which is ill-defined on the original XXZLG PES. Additional technical details of the XXZLG PES are discussed in the appendices.

b. The IMLS PES

Li *et al.*[56] reported a ground-state IMLS PES for HO_2 based on icMRCI+Q data using CBS extrapolation and 18-reference-states with dynamic weighting. We used the C_S point group and built the set of molecular states from separate ground state atoms,

$$HO_2(^2A'') \rightarrow O(^3P_g) + O(^3P_g) + H(^2S_g). \quad (19)$$

Resolving the atomic states into the molecular C_S point group using tables from Herzberg[88] and combining into molecular states yields a total of 18 doublet states (10 ^{2}A', 8 ^{2}A") which are asymptotically degenerate for separated atoms. There are also sets of higher spin quartet and sextet states not considered here. The 18 doublet states were included in dynamically weighted (DW) state-averaged (SA) CASSCF calculations[89,90] using a full-valence active space. Maximum weight was focused on the ground ^{2}A" state, and weights for the other states were determined by the DW scheme with B = 2.0 eV.[90] The DW scheme correctly reflects the differing degeneracies which arise in different regions of the PES, including Renner-Teller degeneracy with the lowest ^{2}A' state observed at linear geometries. The DW multistate scheme also promotes robust convergence that is critically important for automated interpolative methods (such as IMLS) in which new data is added automatically. Using the DW 18-state description, no convergence problems such as those noted in the 2-state fixed weight calculations reported by Xie *et al.*[53] were encountered. The 18-state DW-SA-CASSCF calculations were used as the reference for subsequent icMRCI+Q calculations.[91,92] All electrons were correlated in the icMRCI calculations, and the CBS limit was estimated using the l^{-3} formula[93] and Dunning's aug-cc-pVTZ and aug-cc-pVQZ bases.[94]

An automated PES generation scheme[28(b),,95,96] was used to construct the IMLS PES. A total of 1,609 symmetry-unique points was generated by the algorithm starting with a seed grid of 200 points. Jacobi coordinates were used with ranges of R_{OO} = [1.0, 2.1] Å and $R_{H\text{-}OO}$ = [0.5, 2.65] Å. Data were computed for $\gamma \leq \pi/2$ with the symmetry partner (π-γ) added at no cost. Explicit inclusion of the symmetry partner ensures correct exchange symmetry and provides smooth behavior across the transition between the two wells. Energy was restricted to a maximum of 70 kcal/mol above the global minimum. The algorithm for generating the PES as well as the form of the interpolative weight function and related numerical parameters are as described in the supporting information of Ref. 28(b). The automatic PES generation was terminated with 1,609 points when the estimated fitting error reached 1 cm^{-1}. The computed *ab initio* value of the isomerization saddle barrier height differs by 2 cm^{-1} from the IMLS PES value while the geometries differ by less than 0.0001 Å, consistent with the estimated quality of the fit. It has been shown in previous studies that once an IMLS PES is fit to negligible fitting error ($\approx$1cm^{-1}), very high fidelity to the structural parameters and vibrational levels associated with that *ab initio* method is achieved.[95]

c. Comparisons of the IMLS, XXZLG, and DMBE-IV PESs

For all three PESs, the dissociation energy (both D_0 and D_e) and the isomerization saddle point energy are listed in Table I along with the measured dissociation energy. The best experimental estimate for D_0(H–OO) is 48.01±0.04 kcal/mol.[97] The value of D_0(H–OO) is 0.21 kcal/mol lower for the IMLS PES,[98] 0.82 kcal/mol lower for XXZLG, and 0.73 kcal/mol higher for DMBE-IV. Typically *ab initio* methods cannot capture all

the correlation energy of a bond and thus underestimate dissociation energies. The remaining ≈0.2 kcal/mol discrepancy in the IMLS result is assigned to error in the CBS procedure as well as the effect of higher-order correlation not captured by the icMRCI method. The classical isomerization barrier is highest on the DMBE-IV PES, with IMLS 0.798 kcal/mol lower and XXZLG 2.01 kcal/mol lower than IMLS. The XXZLG value in Table I is the value for the fitted PES. As discussed above, when the electronic structure method that XXZLG is based on is used to directly calculate the barrier, the result is 1.3 kcal/mol higher than the value in the table. This barrier is ≈0.7 kcal/mol lower than the IMLS barrier and consistent with the differences found for dissociation.

The entries in the lower part of Table I are the geometries of the equilibrium and isomerization saddle point structures. The experimental HO_2 equilibrium geometry is essentially exactly given by the DMBE PES (which was adjusted to do this) and closely approximated by the XXZLG and IMLS PESs. While the XXZLG and IMLS PESs have very similar isomerization saddle point geometries, the DMBE PES has a noticeably more elongated structure; that is, longer R_{OO} and R_{OH} distances.

Table I Dissociation and isomerization energies and equilibrium and isomerization saddle point geometries for the DMBE-IV, XXZLG, and IMLS PESs; and available experimental results

	DMBE-IV	XXZLG	IMLS	Experiment
Energetics (kcal/mol)				
Dissociation to $H+O_2$ D_0	48.74[a]	47.19[b,c]	47.80[b,c,d]	48.01±0.04[e]
D_e	54.85	53.68	54.36	
Isomerization Barrier	40.72	36.92	38.93	
Geometries				
Equilibrium				
r(OH) Å	0.9708	0.9708	0.9689	0.9705[f]
r(OO) Å	1.3305	1.3341	1.327	1.330[f]
Ð (OOH)^o	104.29	104.12	104.39	104.29[f]
Isomerization Saddle Point				
r(OH) Å	1.202	1.174	1.162	
r(OO) Å	1.484	1.424	1.420	
Ð (OOH)^o	51.88	52.66	52.34	

[a] Mandelshtam *et al*., Ref. 66.

[b] The O_2 harmonic ZPE required for D0 is 787 cm^{-1}. There is an inconsequential anharmonic contribution to the O_2 zero point energy; experimentally determined $w_e x_e$ is ≈12 cm^{-1} [P. H. Krupenie, J. Chem. Ref. Data 1, 423 (1972)].

[c] The HO_2 ZPE used in calculating for D_0 has an anharmonic value of 3054.6 cm^{-1} (for XXZLG) and 3083.2 cm^{-1} (for IMLS) calculated as described in the text.

[d] The fitted range of the IMLS PES only extends to $R_{H–OO}$ = 2.65 Å, so the asymptotic energy was evaluated from an electronic structure calculation with $R_{H–OO}$ = 25.0 Å. The difference in energy between 25.0 Å and 2.65 Å is 0.11 kcal/mol.

[e] Ruscic, Ref. 97.

[f] Lubic, Ref. 63(a).

Table II lists the calculated lower vibrational levels on the three PESs and the experimental values. For the IMLS and XXZLG PESs, the entries in Table II and the HO_2 zero point energy (ZPE), referred to in Table I, are from a potential-optimized discrete variable representation (PODVR) variational calculation.[99] The details of those calculations are as reported in Ref. 56 for the IMLS PES. Vibrational levels have been reported[53,54] for the two earliest versions of XXZLG PESs but not for the later version used here. The XXZLG and IMLS PESs predict vibrational spectra in excellent agreement with experiment.[63] For the seven levels listed in Table II, the root-mean-square

(rms) error with respect to experiment is ≈9 cm^{-1} for the XXZLG PES and ≈10 cm^{-1} for the IMLS PES. In contrast, the rms error for the DMBE-IV PES is an order of magnitude larger.

We have found previously that a litany of small corrections such as core correlation, CBS extrapolation, spin-orbit or relativistic corrections can offset each other, and unless everything is included, improving one aspect of the electronic structure calculation might not improve agreement with experiment (if the lower-level calculations benefit from cancelation of errors). Further improvements of the XXZLG and IMLS PESs with high-level electronic structure theory results will require addressing the effects of these many small corrections.

Table II. Comparison to experiment of the calculated vibrational levels in cm^{-1} for the DMBE-IV, XXZLG, and IMLS PESs.

	DMBE-IV[a]	XXZLG	IMLS	Experiment
HO_2				
(001)	1065.5 (32.1)[b]	1090.1 (7.5)	1104.7 (-7.1)	1097.63[c]
(010)	1296.4 (95.4)	1388.4 (3.4)	1395.9 (-4.1)	1391.75[c]
(100)	3333.7 (102.5)	3442.6 (-6.4)	3448.9 (-12.7)	3436.20[d]
(200)	6492.4 (158.8)	6671.0 (-19.8)	6672.8 (-21.6)	6651.19[e]
DO_2				
(001)		1015.0 (5.2)	1023.4 (-3.2)	1020.16[f]
(010)		1116.5 (5.0)	1122.3 (-0.8)	1121.47[f]
(100)		2552.7 (-3.5)	2551.7 (-2.5)	2549.22[g]

[a] Brandao *et al*., Ref. 57.
[b] The numbers in parentheses are the differences in the experimental and calculated values.
[c] Burkerholder, 63(e)
[d] Yamada, 63(d)
[e] DeSain, 63(f)
[f] Uehara, 63 (b)
[g] Lubic, 63(a)

The contour plots of the three PESs in Fig. 5 highlight the similarity in global shapes of the IMLS and XXZLG PESs and how they differ from the DMBE-IV PES. In these

plots, the Jacobi coordinates $R_{OO\text{-}H}$ and $\measuredangle\theta_{OO\text{-}H}$ vary while the O–O bond distance is fixed at the value in the HO_2 equilibrium geometry of each respective PES. The plots of the XXZLG and DMBE-IV PESs are matched side by side along the O–O perpendicular bisector symmetry line with the plot of the IMLS surface in order to provide direct comparison of the surfaces. The two symmetrically related equilibrium positions can be seen with the isomerization barrier separating them. At the top of each plot, the two symmetrically related dissociation channels from each isomer are readily seen. At the bottom of each plot, there are two symmetrically related barriers to linearity in the H-O-O bending motion.

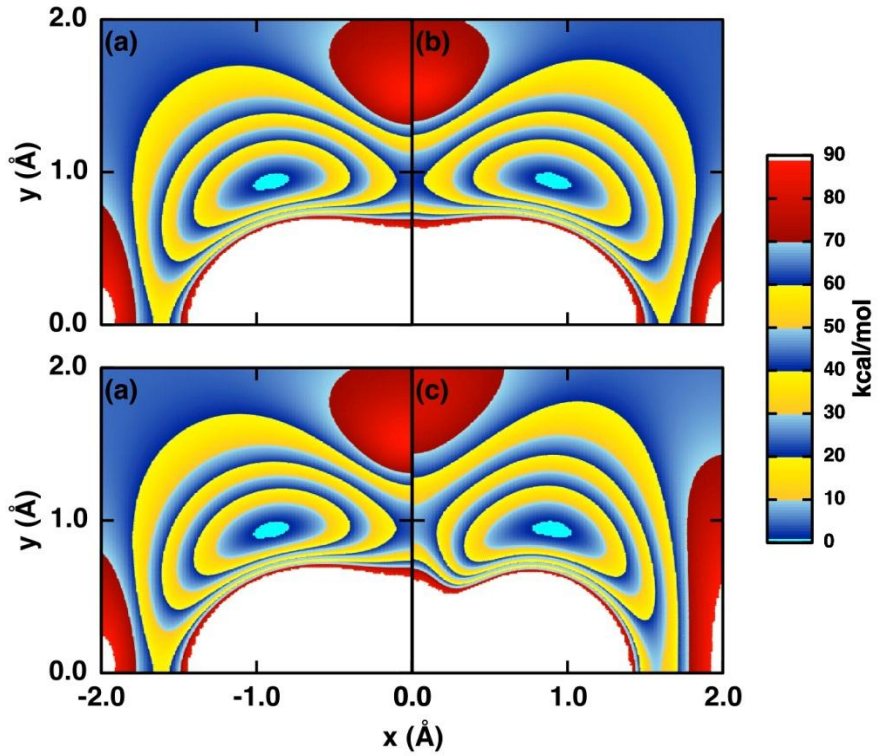

Figure 5 Contour plots of the IMLS (a), XXZLG (b), and DMBE-IV (c) surfaces, with respect to ROH and the center of mass angle of H with the O-O bond. The O-O bond distance is fixed at the HO_2 equilibrium geometry of each PES. Contour spacing is 10 kcal/mol.

On the scale of Fig. 5, the IMLS and XXZLG PESs in the top panel appear to be very similar; however, there is a slight mismatch (≈1 kcal/mol) at the isomerization symmetry line and at the barrier to linearity. The width of the dissociation channel illustrated by the closeness of the red features in the plot is probably slightly narrower in the IMLS PES. These results are consistent with the energy differences in Table I. The bottom panel of Fig. 5 shows that the IMLS and DMBE-IV PESs are clearly different, with the DMBE-IV having a more curved reaction path between the isomerization barrier and the equilibrium point, a considerably lower barrier to linearity, and a narrower dissociation channel. Yang and Klippenstein[67] commented on the lack of sufficient *ab initio* input into DMBE-IV for the bending component of the dissociation channel and the possible implications for reliable rate constant calculations.

The manifestations in the dynamics of the similarities and differences in the three PESs are clearly illustrated with SOS plots.[100] The SOS plots shown in Fig. 6 were calculated on each of the three PESs with groups of 50 trajectories with energies of 10.0, 20.0, 30.0, and 40.0 kcal/mol (trajectory details are given in Sec. B.1.). The 2N-2 mapping,[100] which defines the 4D subspace, was done by freezing the O-O distance at the respective equilibrium value for each PES (as in Fig. 5). Xu, *et al.*[78] found evidence of regularity in the motion of the O-O mode up to dissociation, but also found signs of irregularity in the motion of the modes associated with the hydrogen atom. This irregular motion, which could be associated with mode mixing, is what we would like to understand. Surfaces-of-section, shown in Fig. 6, makes the visualization of the accessible phase space and identification of regularities in trajectories straightforward and allow for direct comparison for reduced dimensionalities of the dynamics. We defined

two planes in Cartesian space using the equilibrium coordinates of the hydrogen atom (x_{min},y_{min}). Figure 6 shows the record of the coordinate x and conjugate momentum P_x each time a trajectory of the hydrogen atom passes through the plane defined by y_{min}. An analogous figure (not included here) for y and P_y for passage through the plane defined by x_{min} shows similar results.

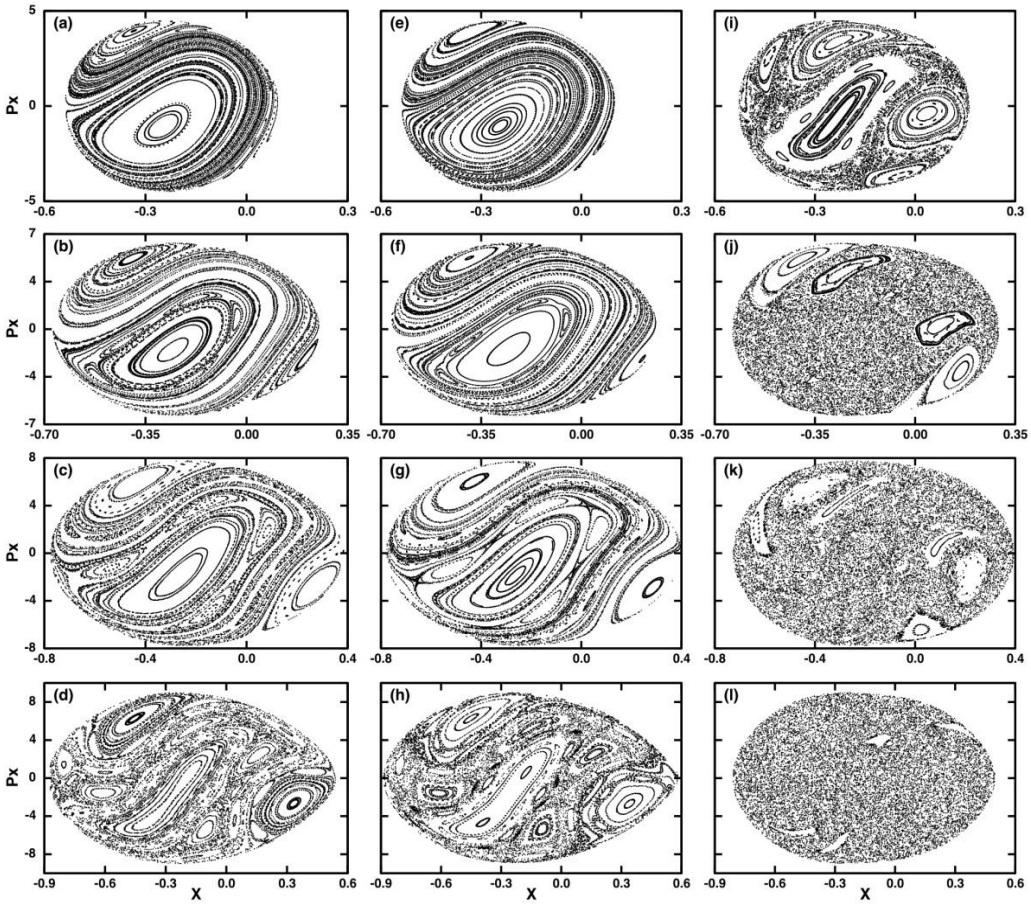

Figure 6 Poincaré surfaces-of-section for x and P_x subspace (see text for details). From the top, rows are results for energies 10, 20, 30, and 40 kcal/mol. From the left, columns are for the IMLS, XXZLG, and DMBE-IV PESs

The results in Fig. 6 for the IMLS and XXZLG PESs are similar over the whole energy range. Except at the highest energy of 40 kcal/mol, both show a regular phase-space structure. At 40 kcal/mol there is increasing irregularity in the phase space,

but the major regular features of the SOS from the two PESs still match. In contrast, the phase space of the DMBE-IV is largely irregular except at the lowest energy of 10 kcal/mol, which is just above the ZPE. The features of the regular phase-space structure do not match well with those of IMLS and XXZLG, consistent with noticeable differences in the vibrational frequencies as seen in Table II. The highest total energy in Fig. 6 remains below the isomerization barrier on all three PESs for the fixed O-O distance of the SOS calculations. (Note that the isomerization barrier heights in Table I are for the O-O distance relaxed.) Related results to those shown in Fig. 6 have been reported by Seidel *et al.*[101] for the DMBE-IV PES and by Barnes and Kellman[102] for earlier versions of the XXZLG PES than the one used here.

These results on energetics, geometry, frequencies, shape, and phase-space structure emphasize the similarities between the IMLS and XXZLG PESs and their common differences with the pioneering DMBE-IV PES. The most easily quantified difference in the IMLS and XXZLG PESs is in the isomerization barrier heights, which is probably mostly due to a local sparsity of *ab initio* data used to fit the XXZLG PES (see Appendices) and only partially due to the different accuracies of the underlying electronic structure theory methods. At greater levels of detail, there are other differences between the IMLS and XXZLG PESs that have implications for dynamics and are explored in Sec. C.

B. Methods

1. Trajectory Calculations

All of the simulations were performed with the classical trajectory code GenDyn.[38] Groups of 50 trajectories were calculated for the SOS plots and groups of 1,000 trajectories were calculated to determine all rate constants. The trajectories were integrated using a fixed step size $5^{th}/6^{th}$-order Adams-Moulton predictor-corrector integrator[43] initiated with a fourth-order Runge-Kutta-Gill routine. The SOS trajectories were integrated for 5 ps. The integration time for the IVR studies was 10 ps. The trajectories for studying reactive processes were integrated until either a reaction criterion was satisfied, or the maximum integration time of 10 ps was reached. Hessian matrices for normal mode and IVR analyses were calculated by fourth-order finite difference.[103] The angular momentum was set to zero in all simulations.

Statistical initial conditions were prepared for total energies of 44, 46, 48, 50, and 52 kcal/mol for isomerization and ≈60.0 kcal/mol for dissociation using the *efficient microcanonical sampling* (EMS)[24,34] algorithm as implemented in GENDYN. All three atoms were moved during a Markov walk started from the equilibrium geometry with a 250,000-step warm-up walk, followed by 100,000-step walks between trajectories. The maximum atomic displacement of each atom was 0.2 Å, and the acceptance/rejection ratio of each walk was in the range of 0.4 to 0.6. Statistical initial conditions were selected for total energies of 10, 20, 30 and 40 kcal/mol for SOS plots. Only the hydrogen atom moved in the Markov walk with a 25,000-step warm-up with subsequent walks of 10,000 steps. The Markov walk assigned only the *x* and *y* components of the momentum of the hydrogen atom. The momenta of the oxygen atoms and the

momentum in the z direction of the hydrogen atom were fixed at zero, restricting the phase space to four dimensions.

Quasiclassical initial conditions[24] were used for initial excitation of one normal mode while the other normal modes were assigned ZPE. At high energies significant regions of phase space may not be well described by the normal modes, which can cause small transient, minor effects in the initial trajectory behavior. However we find that these minor effects do not influence the conclusions of this study. The mode-specific initial excitations are listed in Table III, where the normal modes are identified by their major component in valence coordinates.

Table III. Initial normal mode excitation energies (and corresponding fractional quantum numbers) and ZPE energies. Excitation quantum numbers are in parentheses.[a]

	DMBE-IV	IMLS	XXZLG
Total Energy (kcal/mol)			
E = ≈35.5 (below isomerization)			
O-O	28.6 (8.6)	28.1 (8.2)	28.4 (8.4)
O-O-H	28.9 (7.0)	28.9 (6.5)	29.0 (6.6)
O-H	31.9 (2.7)	31.6 (2.5)	31.5 (2.5)
E = ≈47.3 (above isomerization)			
O-O	40.9 (12.5)	40.1 (11.8)	39.9 (12.0)
O-O-H	40.6 (10.0)	40.5 (9.3)	40.5 (9.4)
O-H	43.8 (3.9)	43.7 (3.7)	43.6 (3.7)
E = ≈59.9 (above dissociation)			
O-O	51.88 (16)		50.34 (15.26)
O-O-H	52.19 (13)		50.72 (11.91)
O-H	54.75 (5)		53.45 (4.593)
Harmonic ZPE			
O-O	1.57	1.63	1.60
O-O-H	1.93	2.07	2.04
O-H	4.98	5.27	5.25

[a.] The normal modes are identified by the major internal coordinate component.

For IVR and isomerization studies, fractional quantum numbers were used to give the same total energy to within ≈1% for each of the PESs. We have repeated the Marque and

Varandas[70] trajectory study of unimolecular dissociation on the DMBE-IV PES. For a comparable calculation using the XXZLG PES, we assigned ZPE to the unexcited modes and used fractional quantum numbers (given in parentheses in Table III) for the excited modes to obtain the same total energy above D_e for the two PESs. The difference in the average total energies for the DMBE-IV and XXZLG PESs corresponds to the difference in D_e (see Table I). The approximate total energy listed in Table III is the mean of these two average energies.

2. Analysis of Trajectories

Studying the energy relaxation of an excited vibrational mode requires a means of measuring energy localization, which can only be done approximately due to ro-vibrational coupling. The method selected for monitoring IVR involves decomposing the kinetic energy by standard transformations[31] into the three normal mode kinetic energies and then assuming that the fraction of total *kinetic* energy in a mode is equivalent to the fraction of total energy in a mode. In this approach, the inherent ambiguity in assigning potential energy to different modes is avoided. Since the normal mode eigenvectors mathematically span the space of the three internal coordinates, the kinetic energy decomposition is, in principle, complete. By this means, the energy $E_i(t)$ in the i^{th} mode is calculated from the trajectories. To us help interpret $E_i(t)$, we developed an analytical kinetics model of energy transfer in a three mode system that is based on two principles: (1) the change in the energy of a mode is directly proportional to the amount of energy the mode currently has and (2) the energy of each mode asymptotically relaxes to the same value, i.e., the total energy divided by the number of modes. As discussed in the

Appendix II, these two principles lead to an explicit expression for $E_i(t)$ in terms of two effective IVR rate constants k_j and one constant c that affects the amplitude of the two decay processes. These expressions will be compared to the classical trajectory results.

The two bond-breaking processes of isomerization and unimolecular dissociation are defined as follows. The time of isomerization was defined to be when the hydrogen atom passed through the symmetry plane, bisecting the O-O bond, provided that the shorter O-H stretching motion underwent two turning points. This arbitrary definition excludes rapidly recrossing trajectories. For dissociation, the lifetime was taken to be the time of the last inner turning point for the shorter OH bond distance before the distance between the center of mass of O_2 and H exceeded 5 Å. This inner turning point definition eliminates the effect of the relative velocity of escaping H-atom on the dissociation lifetime. By the turning point definition of a lifetime, any trajectory that dissociates with no inner turning point must be back integrated in time to find its last inner turning point in negative time. We refer to these rapidly dissociating trajectories as "ballistic" trajectories.[104]

The first-order rate constants for isomerization and dissociation were calculated by least-squares fitting of the unisomerized or undissociated trajectory populations (determined from the lifetimes) to the bi-exponential form:

$$E(t) = A\exp(-k_1 t) + B\exp(-k_2 t) \qquad (20)$$

where A and B are prefactors and k_1 and k_2 are rate constants. The prefactors were determined by linear least squares fitting and the rate constants were determined by a grid search. In many cases, the second term in Eq. (20) was found to be negligible. For some mode-specific excitations, for an initial period of time there is either no decay rate or an

accelerating decay rate. The reasons for such initial regions are varied[24 (a)] and will be discussed as they appear in the next section. We will refer to this as a latency effect. Equation (20) is inappropriate for fitting such behavior, and in Appendix II we develop a method to determine a latency time t_0. Any population information that occurred before t_0, in the groups of trajectories that displayed latent effects, was excluded from the fitting process of Eq. (20).

C. Results and Discussion

We have run trajectories on all three PESs to compare the HO_2 IVR dynamics, the isomerization dynamics of H-O-O' → O-O'-H, and the unimolecular dissociation dynamics of $HO_2 \rightarrow H + O_2$. The results of each of these are now discussed in order.

1. IVR

Normal mode kinetic energies as fractions of the total are plotted as a function of time in Figs. 7 and 8 for total energies of 35.5 kcal/mol and 47.3 kcal/mol, respectively; the red, magenta, and green curves correspond, respectively, to the results of the initially excited O–O stretching, O-O-H bending, and O-H stretching modes. These two different energies were selected to determine the effect of isomerization on the relaxation process. Isomerization is not energetically accessible on any of the PESs at 35.5 kcal/mol but is at 47.3 kcal/mol. The results in the columns from left to right are for the IMLS, XXZLG, and DMBE-IV PESs.

The results for 35.5 kcal/mol are quite similar for the IMLS and XXZLG PESs down to fine detail. The relaxation timescale is well beyond the duration of the integration time

of the trajectories (10 ps) regardless of the excited mode. The relative ordering of the modes from fastest to slowest is: OH*, OOH* and then OO*. The ordering is similar with the results from the DMBE IV; however, the relaxation of trajectories on this surface completed within 1 ps to 2 ps (note the expanded x-axis timescale for the DMBE-IV PES results in Fig. 7).

The results in Fig. 7 illustrate some of the limitations of our mode-specific trajectory studies. The ZPE fraction of the total energy of 35.5 kcal/mol is ≈0.05 for the OO and OOH modes and ≈0.15 for the OH mode (see Table III). Consequently, the top (OO*) and middle (OOH*) row of panels in Fig. 7 should have the excited mode energy fraction starting at ≈0.8 while the lower row (OH*) should start at ≈0.9. This expectation of the fractional partitioning of energy in the normal modes is only true for the OO* energy. For the other cases, the initial fraction is noticeably lower, and for OOH* on the DMBE-IV PES, it would appear that *two* modes are excited. On all three PESs, when either OH* or OOH* are initially excited, there is a rapid energy redistribution from the selected initial distribution to what is seen in Fig. 7 on a timescale less than 100 fs, too fast to be resolved in the figure. This redistribution is undoubtedly due to the inherent difficulties of decomposing the total energy into contributions from specific modes and the use of normal modes for assigning the initial conditions. The kinetics model does not include such processes, and no attempt is made to initialize the model to the true initial conditions. Rather, as discussed in the Appendix II, a least-squares procedure is used to get effective initial conditions. The resulting fits are the black lines in Fig. 7, with optimized values of k_1, k_2, and appearing c in Table IV. There is later discussion of expanding the two exponentials as linear functions to characterize the fitting process.

These linear expansions are described by two slopes sΔ and sΓ that also appear in this Table IV .

The results in Fig. 7 show that the kinetics model fits the trajectory results very well. The only clear but minor fitting deficiency occurs for the IMLS and XXZLG PESs for OH* at early times (< 1 ps). In this case, the trajectory results and the model display a fast and a slow decay for each mode of energy. However, in the region of slow decay the OO and OOH energy fractions maintain a near constant *absolute* difference with time, a result that cannot be represented by the common slow rate constant of the model. In effect, the trajectory results exhibit more decay constants than the model can provide, implying the physical principles upon which the model is based are insufficient to describe the results in detail.

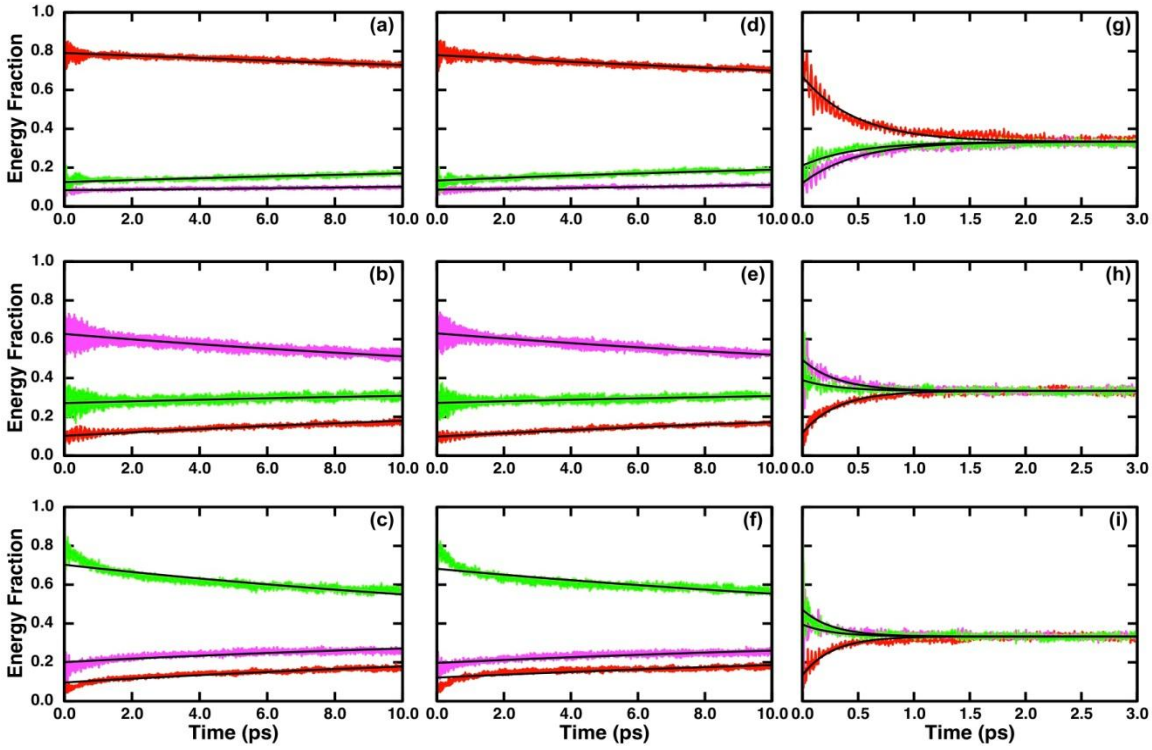

Figure 7 Ensemble-averaged normal mode energies as functions of time for initial conditions of mode-specific excitation (see text for details) and a total energy of ≈35.5 kcal/mol. From the top, rows are results for the excited mode being OO*, OOH*, and OH*. From the left, columns are results for the IMLS, XXZLG, and DMBE-IV PESs. In all panels, red, magenta, and green curves represent the OO, OOH, and OH modes, respectively, while the black lines represent the kinetics model fits.

Table IV. IVR rate constants (ps^{-1}) for specific mode excitations.[a]

		E =35.5 kcal/mol			E=47.3 kcal/mol		
		IMLS	XXZLG	DMBE IV	IMLS	XXZLG	DMBE IV
OO*	c	0.8(6)	-0.1(3)	1.66(9)	2.2(9)	2.1(3)	4.2(1)
k_1		0.003(5)	0.017(4)	0.72(5)	0.05(3)	0.07(1)	0.32(1)
k_2		0.014()	0.037(4)	2.18(5)	0.16(3)	0.22(1)	1.37(1)
$s\Delta$		-0.0076	-0.012				
$s\Gamma$		0.0024	0.0045				
OO*	c	-2.0(7)	1.2(4)	-2.4(9)	0.33(5)	0.42(2)	0.50(3)
k_1		0.042(8)	0.015(8)	3.0(1)	0.051(9)	0.040(8)	0.0(3)
k_2		0.092(8)	0.045(8)	9.0(1)	0.258(9)	0.394(8)	10.6(3)
$s\Delta$		-0.021	-0.018				
$s\Gamma$		0.00075	0.0045				
OO*	c	1.3(4)	1.2(6)	0.53(2)	0.57(2)	0.58(2)	0.61(3)
k_1		0.02(1)	0.02(1)	3.4(6)	0.50(3)	0.32(2)	7.0(2)
k_2		0.054(8)	0.049(3)	94.0(2)	5.4(1)	3.21(4)	62.0(2)
$s\Delta$		-0.032	-0.025				
$s\Gamma$		-0.00087	0.0096				

[a] Number in parentheses is the uncertainty in the last digit.

Figure 8 is the analogue of Fig. 7 but for 47.3 kcal/mol, which is above the barriers for isomerization for the three PESs. Table IV contains the optimized values of the kinetics model parameters. The IVR above the isomerization threshold is similar in fine detail for the IMLS and XXZLG PESs. The relaxation timescale for all excited modes is comparable to or less than the duration of the trajectories (10 ps). In contrast, on the DMBE-IV PES IVR is complete by ≈1 ps or less no matter what mode is excited (notice the smaller x-axis scale for the DMBE-IV PES results in Fig. 8). The excited OH* and OOH* relax faster with OO* noticeably slower for all three PESs, as is the case for the lower-lenergy results shown in Fig. 7. As in Fig. 7 and for the same reasons, there are fast redistribution effects. The ≈12.3 kcal/mol increase into each excited mode should make the initial energy fraction higher in Fig. 8 than in Fig. 7. In almost all cases the apparent initial fraction is *lower* due to short time (≤ 100 fs) energy redistribution not resolvable in the panels.

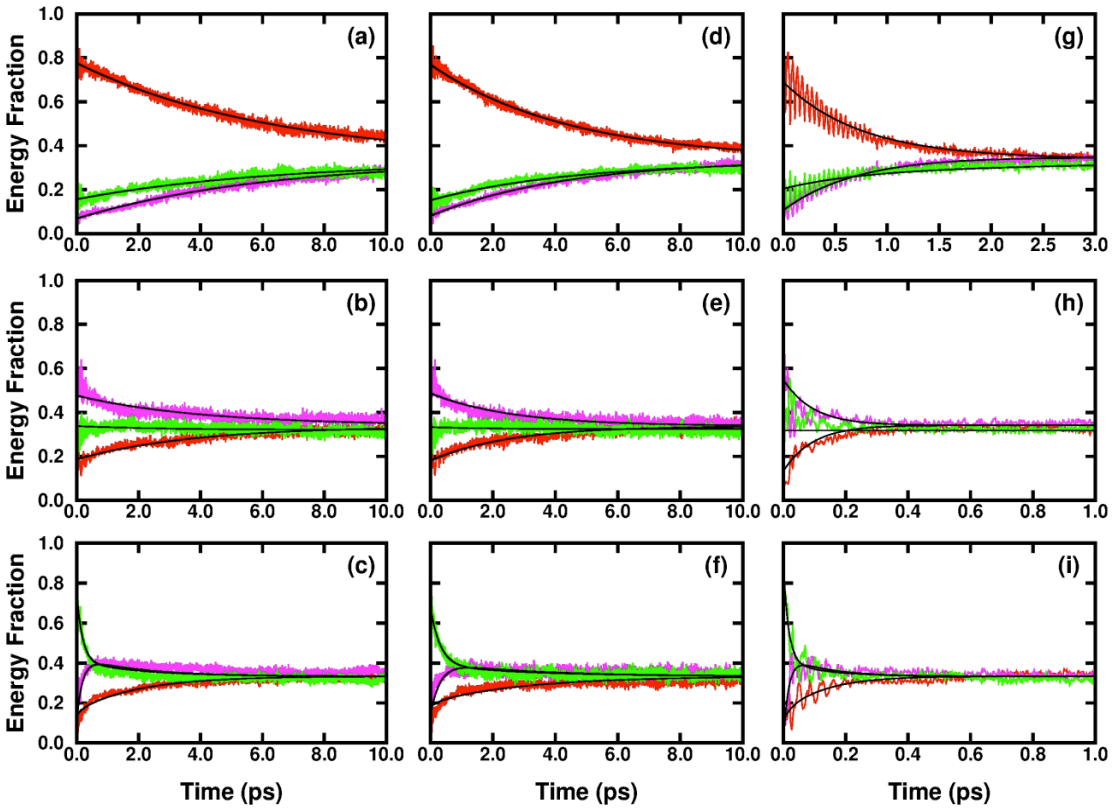

Figure 8 The same as Fig. 3 except for a total energy of ≈47.3 kcal/mol.

Although the results in Fig. 8 show more varied relaxations including an overshoot of the asymptotic equipartition of energy, the kinetics model fits the trajectory results at nearly comparable quality to that in Fig. 7 for the lower energy. The clearest deficiency concerns OOH* relaxation on both the IMLS and XXZLG PESs where the decay at short times is underestimated. In this case, E_2, the OH energy, is essentially at its asymptotic value of $E/3$ except at times too early to be resolved on the plot. Energy conservation then forces E_1 and E_3 to be essentially mirror images of each other about the E_2 at all times. The fits and trajectory results display this symmetry but the kinetics model is too simplistic to represent the higher frequency or transient decay components of the trajectories. A second deficiency is OOH* for DMBE where E_2 is poorly represented at

very short times (<200 fs). The temporal range of the panel is only 1 ps but the fit is applied over the entire 10 ps range. Upon close examination of the panel, the fit has two asymptotic values, one for E_2 and the other for E_1 and E_3. Through most of the range of the panel and beyond to the 10 ps maximum range of the fit, the trajectory results for OOH* on the DMBE-IV PES exhibit an E_2 energy fraction persistently lower than the energy fraction for the other two modes. This behavior forces the optimum fit to display two asymptotes at the price of a poor representation of E_2 at very early times. (How the model can realize two asymptotes is discussed in Appendix II material.) In this case, the trajectory approach to equilibrium is too complicated for the kinetics model.

It is convenient to discuss the IMLS and XXZLG results in Table IV first, then the DMBE-IV results. A leading feature of the IMLS and XXZLG results is that for 35.5 kcal/mol, all the values for k_1 and k_2 are smaller than 0.1 ps^{-1} whereas for 47.3 kcal/mol at least k_2 is substantially greater than 0.1 ps^{-1}. This means that for all or at least most of the 10 ps temporal range of the IVR data at 35.5 kcal/mol, the exponentials in the fitting function of Eq. (S.4), found in Appendix II, can be reasonably well approximated by a first-order expansion that is linear in time. The fits in Fig. 7 clearly show this approximately linear behavior. As discussed in Appendix II, in such circumstances the decay is best represented by two slopes, s_Δ and s_Γ, which only for IMLS and XXZLG at 35.5 kcal/mol are listed in Table IV. For both IMLS and XXZLG, the values of s_Δ and s_Γ show overall that IVR becomes more rapid in the order OO*, OOH*, and OH*. However, the IMLS and XXZLG values are not that similar. For the larger slope s_Δ, the IMLS value varies from ≈60% lower to ≈30% higher than the XXZLG value. The lesser slope s_Γ, the IMLS value varies from ≈15% to 90% of the XXZLG value. The IMLS and

XXZLG results at 35 kcal/mol look quite similar in Fig. 7, but that is somewhat due to the fact that only a fraction of the decay takes place in 10 ps. Had the trajectory results been carried out to longer times, the differences would likely be more manifest.

The IMLS and XXZLG results for 47.3 kcal/mol in Table IV show relaxation rate constants that are all considerably larger than the rate constants at the lower energy. Exponential, as opposed to linear, decay is much more evident in Fig. 8. As for 35 kcal/mol, for both IMLS and XXZLG the IVR decay rate constants increase in the order OO*, OOH*, and OH*. The OH* rate constants are an order of magnitude larger than the rate constants of OOH*, a much larger increase than at 35 kcal/mol and an indication of an accelerating OH* decay. For the large decay rate k_2, the IMLS value is from ≈65% lower to ≈65% higher than the XXZLG value. For the smaller decay rate k_1, the IMLS value is from ≈70% lower to ≈60% higher than the XXZLG value. Together with similar results at 35 kcal/mol, the results indicate that IMLS and XXZLG do have somewhat different IVR decay characteristics. Over this energy range, IMLS IVR occurs more slowly for OO* and more rapidly for OH* relative to XXZLG IVR decay. For OOH* over this energy range, the IMLS and XXZLG exchange order with respect to decay rate constants.

Unlike IMLS and XXZLG, a 10 ps timescale is sufficient at both energies to capture all of the IVR processes on DMBE-IV. The k_1 and k_2 values time constants obtained using the DMBE-IV PES in Table IV are at least 40 times larger at 35 kcal/mol and at least 4.5 times larger at 47.3 kcal/mol than the corresponding rate constants computed using the IMLS or XXZLG PESs. This implies a significant qualitative difference in the dynamics and associated IVR. For example, the DMBE-IV results for OH* at both

energies below and above isomerization has the larger k_2 time constant exceeds 50 ps^{-1}, implying relaxation over within a 10 fs to 20 fs, or one to two OH vibrational periods. Such processes are not resolvable in the IMLS and XXZLG panels of Figs. 7 and 8 but in the expanded timescale of the panels for DMBE, they are just visible in the earliest times on the plots. As discussed earlier, on this timescale limitations in the initial condition preparation and the approximations used to monitor mode-specific energies lead to noticeable apparent redistributions of energy. For IMLS and XXZLG, the fit is insensitive to such processes because slow energy transfer processes that extend over the whole temporal range outweigh such brief transients. However, for DMBE-IV, these transients are more comparable to the usual energy transfer processes and the fits at least of OH* reflect that.

Consistent with IMLS and XXZLG, the DMBE-IV decay rate is slowest for OO* and fastest for OH*. In contrast to IMLS and XXZLG, the DMBE-IV decay rate constants have a much milder dependence on energy and, in the case of OO*, the decay rate constants actually decrease with energy. Careful examination of the OO* results for the DMBE-IV PES in Figs. 7 and 8 show the trajectories predict a slightly slower relaxation at the higher total energy. The DMBE-IV PES has the highest isomerization barrier, ≈1.8 kcal/mol higher than IMLS. This might imply that the phase space volume associated with the isomerization region of the PES is less accessible for the DMBE-IV PES than for the IMLS or XXZLG PES, resulting in a corresponding decrease to already rapid IVR for the bend and stretch modes most coupled at the isomerization saddle point.

To better understand the effect of isomerization on IVR,[105] the energy fraction of different modes is plotted as a function of time in Fig. 9 for the time-dependent ensemble

of trajectories that have not yet isomerized. As time progresses, isomerization reduces the number of trajectories in this ensemble causing the sampling noise in the ensemble averaged energy fraction to increase. For this reason, the energy fraction was not followed beyond the time where 90% of the trajectories had isomerized. The comparison of Fig. 9, which excludes isomerization, to Fig. 8, which includes isomerization, shows qualitative differences.

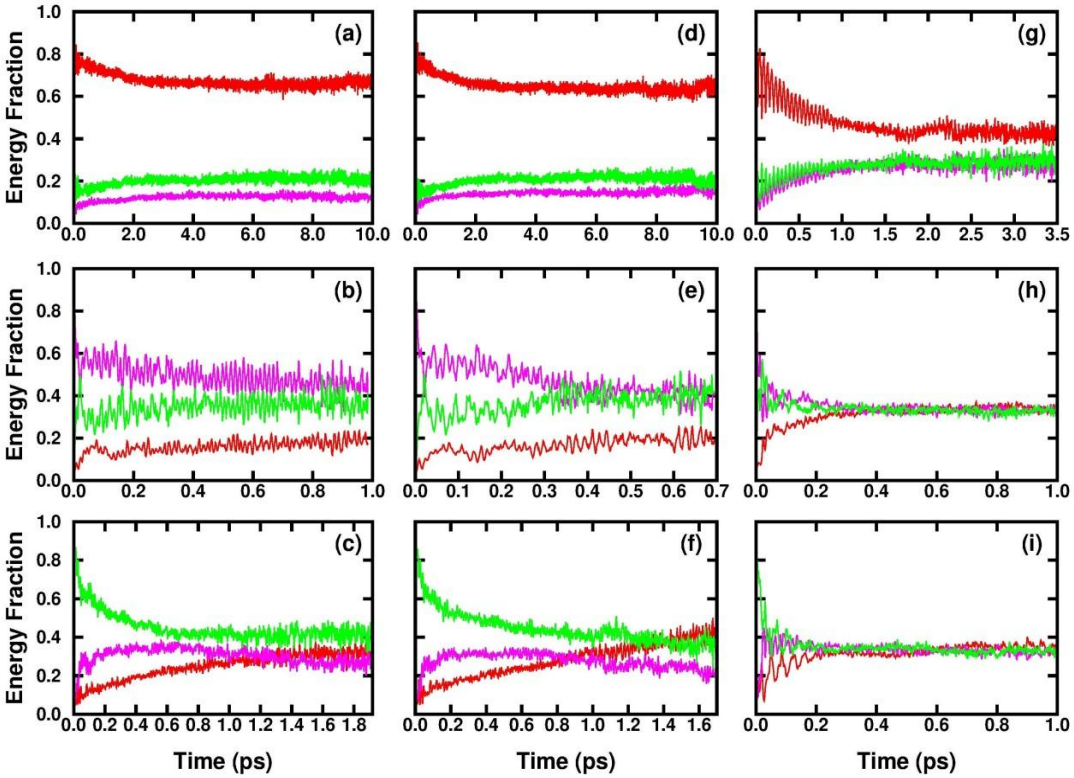

Figure 9 The same as Fig. 8 only for the populations of those trajectories at time t that have not yet isomerized. The time history of each unisomerized population stops at either 10 ps, or when only 10% of the population remains.

Before discussing the differences, note that the OOH* and OH* DMBE-IV results in panels (h) and (i) are almost identical in Figs. 8 and 9. As will be shown in Sec. C.2 of the results and discussion, for these two cases the isomerization rate is significantly

slower than the IVR rate. The IVR is essentially complete before isomerization begins. In all other cases in Figs. 8 and 9, the IVR is comparable to or slower than isomerization. In these other cases, Fig. 9 shows that isomerization selectively removes from the ensemble those trajectories that spend most of their time with more OOH bend energy and leaves behind trajectories that have larger OO and OH stretch energy. This is most clearly seen for all three PESs for OO*. The results in Fig. 9 suggest that the asymptotic equipartition of energy is not reached in the ensemble of unisomerized radicals because the isomerization removes those with sufficient energy in the OOH and OH modes to isomerize leaving a population with "excess" energy in the OO mode. As shown in Sec. B.2, the main difference between DMBE-IV and IMLS or XXZLG in the top row of Fig. 9 is that the isomerization and IVR rate constants are comparable for only DMBE-IV, for which some of the IVR is complete before isomerization becomes significant. In the cases of OOH* and OH* excitations on the IMLS or XXZLG PES, the removal of isomerized species from the ensemble results in a much shorter timescale shown in Fig. 9, which is an indication of how dominant isomerization is over IVR. The results for OOH* clearly illustrate that isomerization is much faster than IVR; note that the timescale of Fig. 9 is about one-tenth that of Fig. 8. An important difference in the two PESs is that they differ by ≈2 kcal/mol in the isomerization barrier.

The results in Fig. 9 show how isomerization acts to create a new energy distribution in the as yet unisomerized population. Under normal circumstances, that new energy distribution cannot be accessed because eventual re-isomerization would further mix all populations. However, conceptually if the isomerized HO_2 could be prevented from re-isomerizing, then the filtering by isomerization could have chemical consequences. For

example, if two different isotopes of oxygen were present in HO_2 and if some isotopically selective photochemical process could prevent a re-isomerization, then the unisomerized population could carry out chemistry with its filtered energy distribution. This kind of effect would be present for any molecule where isomerization is faster than IVR.

2. Isomerization

Since the trajectories used for the IVR calculations in Figs. 8 and 9 isomerized on all three PESs, these same trajectories can be analyzed for mode-specific isomerization. The normalized populations of unisomerized trajectories as a function of time are plotted in Fig. 10 along with the fit according to Eq. (20), whose rate constants are listed in Table V. In the figure, red (OO*), magenta (OOH*), and green (OH*) curves are compared to the black dashed curves of the fit.

Figure 10 displays what we have called a latency time in Sec. B.2 For all three PESs, OO* has an initial accelerating rate while for IMLS and XXZLG, OH* has a shelf visible in the plot inserts. A prominent reason for such features is that the initial position of the hydrogen atom for OO* and OH* are well removed from the perpendicular bisecting plane of the O-O bond. Even with facile energy transfer into the bending mode, the hydrogen atom will take time to reach the isomerization region. Also as discussed concerning IVR, imperfect initial conditions can affect initial energy transfer. Taken together, these effects can give rise to latency in the isomerization time. As described in Supplemental Material, the population up to the latency time listed in Table V is not included in the fit of Eq. (20). This results in a single exponential fit, i.e., $B = 0$ in Eq. (20), for all three excitations for DMBE-IV and for OO* for IMLS and XXZLG.

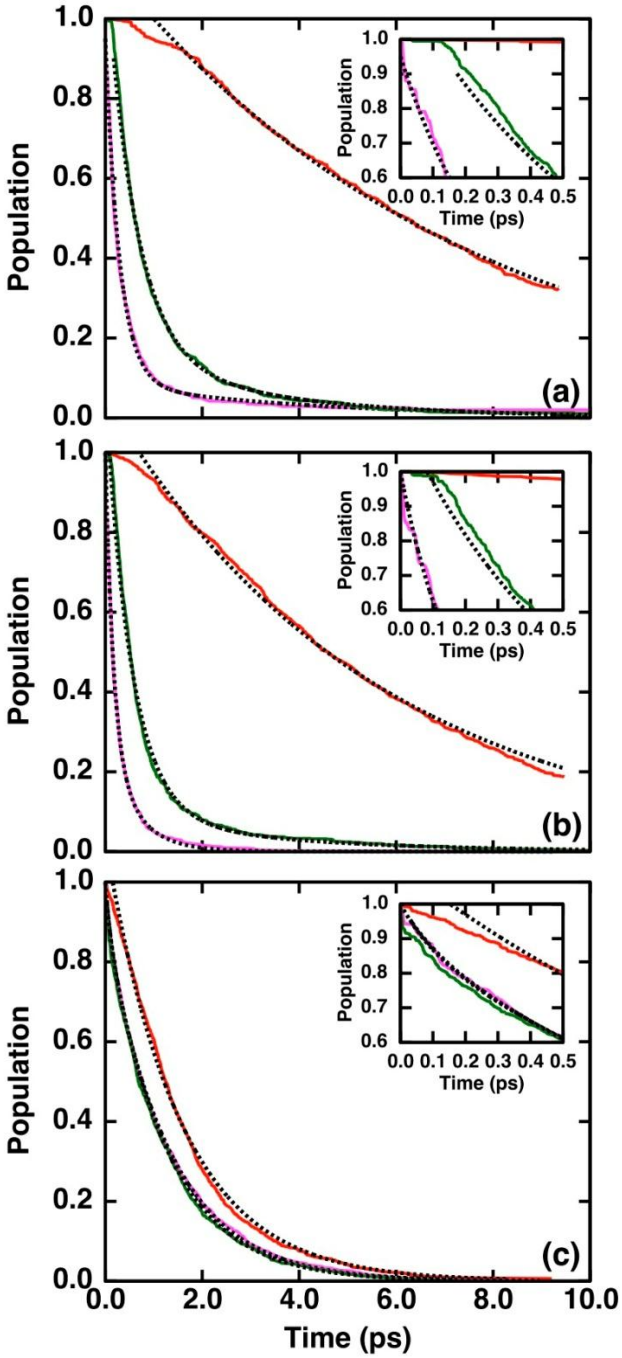

Figure 10 For the IMLS (a), XXZLG (b), and DMBE-IV (c) PESs, the population decay as a function of time due to isomerization for initial conditions of mode-specific excitation at a total energy of ≈47.3 kcal/mol (see text for details). In all panels, red, magenta, and green curves represent the OO, OOH, and OH modes respectively while the black lines represent the kinetics model fits. Inserts in each panel magnify the results at

early times.

A prominent reason for such features is that the initial position of the hydrogen atom for OO* and OH* is well removed from the perpendicular bisecting plane of the O-O bond. Even with facile energy transfer into the bending mode, the hydrogen atom will take time to reach the isomerization region. Also as discussed concerning IVR, imperfect initial conditions can affect initial energy transfer. Taken together, these effects can give rise to latency in the isomerization time. As described in Appendix II, the population up to the latency time listed in Table V is not included in the fit of Eq. (20). This results in a single exponential fit, i.e., $B = 0$ in Eq. (20), for all three excitations for DMBE-IV and for OO* for IMLS and XXZLG.

Table V. Isomerization rate constants (ps^{-1}), prefactors, and latency times (ps) under different initial conditions as a function of energy for the three different PESs.

Energy	Initial	IMLS					XXZLG					DMBE-IV		
(kcal/mol)	Conditions	A	k_1	B	k_2	t_0	A	k_1	B	k_2	t_0	A	k_1	t_0
44.0	EMS	0.56	0.04	0.40	0.71		0.49	0.13	0.48	1.31		1.00	0.22	
46.0	EMS	0.46	0.16	0.52	1.77		0.40	0.19	0.54	1.93		1.00	0.53	
47.3	OO*	0.99	0.13			1.53	0.99	0.18			1.24	1.23	0.68	0.38
	OOH*	0.08	0.23	0.87	3.40		0.14	1.04	0.84	5.01		0.92	0.77	
	OH*	0.16	0.31	0.99	1.63	0.17	0.11	0.30	1.07	1.98	0.28	0.94	0.82	
48.0	EMS	0.43	0.21	0.55	2.53		0.37	0.32	0.59	2.73		1.00	0.90	
50.0	EMS	0.33	0.28	0.62	2.84		0.27	0.36	0.69	2.94		0.96	1.44	
52.0	EMS	0.30	0.36	0.66	3.49		0.30	0.58	0.68	4.14		0.97	1.78	

For IMLS and XXZLG, Fig. 10 clearly shows the rate constant for isomerization is quite dependent on which mode was initially excited. In particular, the OO* isomerization rate is on the order of 10 times slower than the rate when either of the two other modes are excited. In Table IV, the relevant IVR rate k_2 is comparable to the isomerization rate in Table V. Since O-O vibration is not the isomerization reaction coordinate, IVR is a necessary first step for isomerization to occur. The substantial latency times and the slow isomerization rate indicate that IVR is the bottleneck for isomerization for OO*. As would be expected, OOH* has the fastest isomerization rate and no latency time because bending motion is a dominant component of the isomerization reaction path. The dominant isomerization rate is an order of magnitude faster than the IVR rate constants in Table IV, meaning that isomerization is largely over before substantial amounts of energy have leaked by IVR into modes less well connected to the isomerization reaction path. The slower rate in the bi-exponential fit to OOH* isomerization is somewhat comparable to the IVR rate constants in Table IV, suggesting that this ≈10% tail to the declining population is a consequence of IVR processes re-assembling energy into the bend. The OH* isomerization rate constants fall in between those of OO* and OOH*. From Table IV, the fastest IVR rate constants are two or three times faster than the dominant isomerization rate constants in Table V and comparable to the dominant isomerization rate constants for OOH*. Although faster than isomerization, there is a time lag between converting OH stretching motion into OOH bending motion which leads to the small (≈100 fs) latency times listed in Table V. IVR distributes energy to OOH, promoting isomerization, but also to OO, which is inefficiently connected to isomerization. Like OOH*, the ≈10% tail to the population declines at a slow rate that is

comparable to most of the IVR rate constants in Table IV, suggesting an IVR-type bottleneck to re-assembling initially misdirected energy back into the bend.

In contrast to IMLS and XXZLG, the results in Fig. 10c and Table V clearly show the isomerization rate obtained using DMBE-IV is independent of which mode is excited. The main difference between modes seen in Fig. 10c is not the rate but the latency time for OO*. Contrasting Tables IV and V, the OO* faster IVR rate is twice that of isomerization, leading to a latency time smaller by a factor of three than those of the other two PESs. The OO* isomerization rate is the smaller than that from either OOH* or OH* excitations by ≈15%, perhaps due to some lingering effects of IVR processes. The OOH* and OH* faster IVR rate constants are at least an order of magnitude faster than the isomerization rate constants, meaning that for most of isomerization, memory of the initial excitation is nearly lost. There are no latency times and the isomerization rate constants are within 10% of each other.

The isomerization decay of an initially random population is plotted in Fig. 11 for total energies 44, 46, 48, 50, and 52 kcal/mol on each PES.

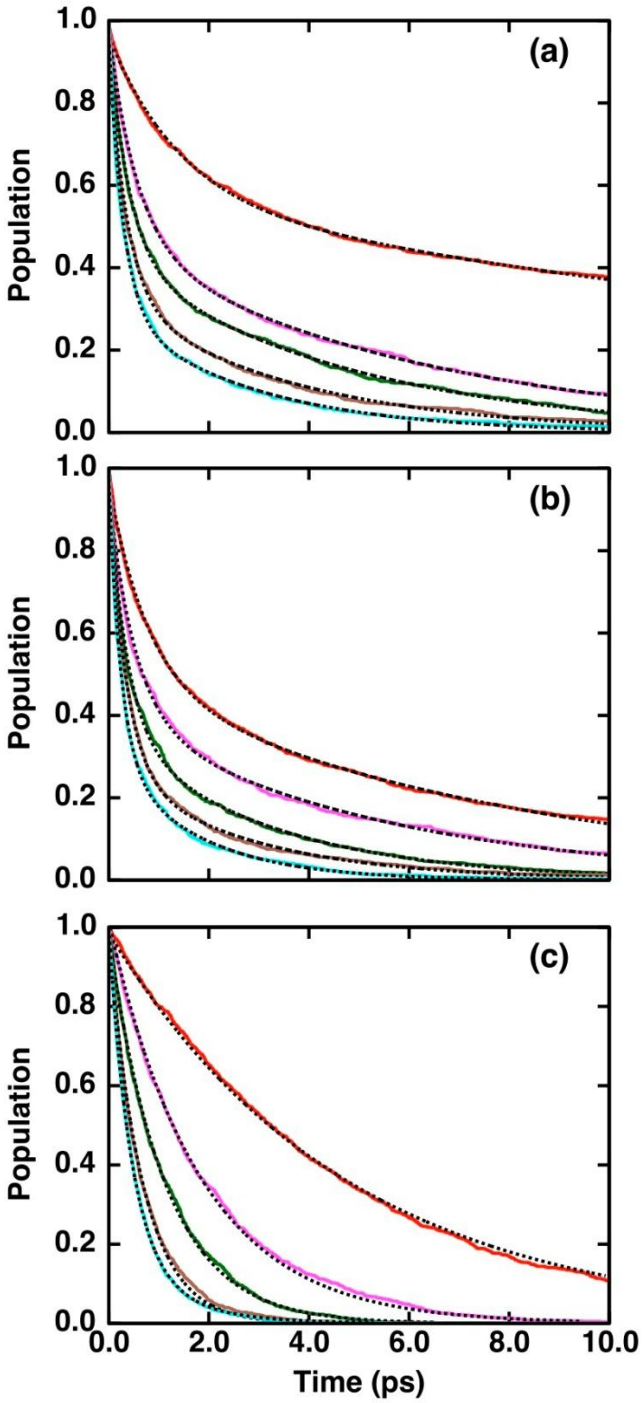

Figure 11 For the IMLS (a), XXZLG (b), and DMBE-IV (c) PESs, the population decay as a function of time due to isomerization for initial conditions selected using EMS (J=0) sampling and for total energies in kcal/mol of 44 (red), 46 (magenta), 48 (green), 50 (brown), and 52 (cyan). The black lines represent the kinetics model fits.

This range of energies was selected so the radical would be above the respective thresholds of isomerization for all of the PESs, but below the classical thresholds for dissociation (see Table I). In Figs. 11(a) and 11(b), the decay curves for IMLS and XXZLG are fit with a bi-exponential function (shown by the dotted curves in the figure) to produce the fast and slow rate constants in Table V for the grid of total energies. In contrast, the decay curves, computed using the DMBE-IV PES results, are well fit by a single exponential; the values of the parameters from the fits are given in Table V. The bi-exponential rate constants of isomerization for statistical initial conditions can be interpreted by using the graphical representation in Fig. 12 of the rate constants in Table V plotted as a function of the total energy above the isomerization barrier on each PES (see Table I). The results are color coded by PES: red, IMLS; blue, XXZLG; magenta, DMBE-IV. The two solid straight lines at the bottom of the plot are the linear least squares fits to the *slower* EMS isomerization rate constants for IMLS and XXZLG. The three dotted straight lines in the figure are the linear least-squares fits to the *faster* IMLS and XXZLG EMS isomerization rate constants and the single DMBE-IV statistical isomerization rate constants. The open symbols (squares, triangles, diamonds) are in order the OO*, OOH*, and OH* isomerization rate constants for DMBE-IV or IMLS and XXZLG (only the rate with the largest prefactor). (The OOH* XXZLG faster isomerization rate of 5.01 ps^{-1}, the largest rate in Table IV, is off the scale of the plot.) The total energy in excess of the isomerization barrier is used for the x axis in this plot to make a side-by-side comparison of the rate constants clearer.

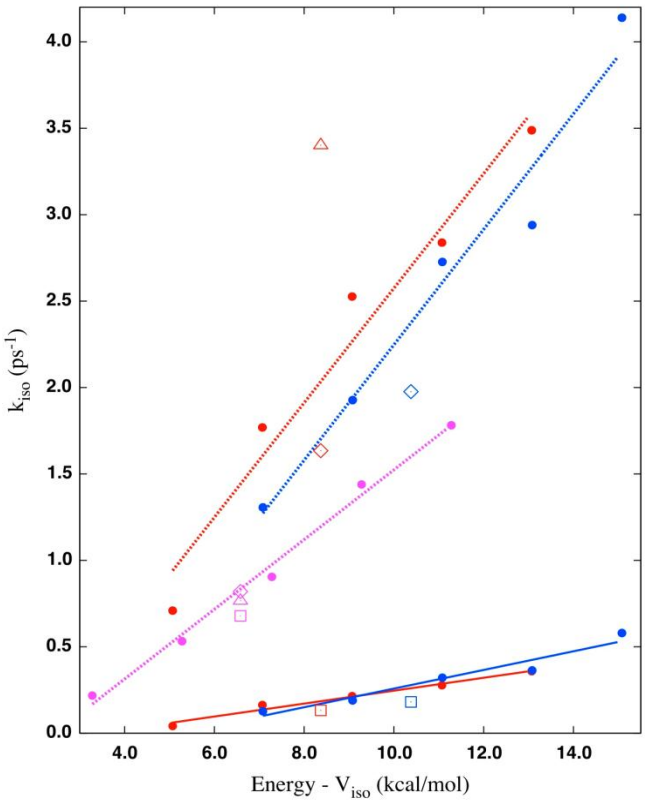

Figure 12 Rate constants for isomerization from Table V plotted as functions of the total energy above the isomerization barrier (V_{iso}). See text for details

For IMLS and XXZLG, among the lowest isomerization rate constants are those for OO*. These rate constants are somewhat lower than the straight-line fits to the slower EMS isomerization rate constant. The likely interpretation is that the slow rate on either IMLS or XXZLG is due to a bottleneck in relaxing, from the initial statistical distribution, those trajectories that have a high degree of O-O vibrational excitation. The calculated rate is a reflection of both isomerization and energy transfer from the O-O stretch into the two other degrees of freedom that are coupled to the isomerization saddle point. In contrast, among the highest IMLS or XXZLG rate constants are those for either OOH* or OH*. At the same energy, the OH* rate constants are comparable to the faster EMS rate constants while the OOH* rate constants are approximately double the faster

EMS rate constants (note the OOH* XXZLG rate is off the scale of the plot). Consequently, the faster EMS rate constants on IMLS and XXZLG have no significant energy transfer bottleneck from either the O-H stretch or the O-O-H bend modes. These faster rate constants are a closer measure of isomerization uncomplicated by energy transfer issues. For DMBE-IV, as discussed above, the OO*, OOH*, and OH* isomerization rate constants are nearly the same because IVR is fast enough to scramble any mode specific initial conditions. Since EMS initial conditions are statistically random, it is not surprising that the least-squares fits to the EMS isomerization rate constants essentially pass through the mode-specific rate constants. The OO* isomerization rate is the lowest below the linear fit to the statistical rate constants and in this case, as discussed above, the IVR rate is only double the isomerization rate. Interestingly, despite the different topologies seen in the three PESs in Fig. 5, the component of the IMLS, XXZLG, and DMBE-IV isomerization rate constants least contaminated by IVR effects all have a similar size, within a factor of two, as indicated by the dotted lines in Fig. 12. This occurs only if the barrier height is subtracted from the total energy, as in Fig. 12, indicating the typical dominance of barrier height over saddle point shape is determining the gross features of the rate constant.

3. Unimolecular dissociation

The mode specific behavior found in IVR and isomerization motivates a similar investigation for the unimolecular dissociation of $HO_2 \rightarrow H + O_2$. As discussed earlier, only the XXZLG and DMBE-IV PESs are fully specified at this limit and can be studied. Marques and Varandas[70] carried out exactly such a study on the DMBE-IV PES, portions

of which we repeat with more trajectories and extend to XXZLG. As discussed in Sec. C.1 we used fractional vibrational quantum numbers on the XXZLG PES in order to preserve the same total energies above D_e. The approximate total energy listed in Table III is the average energy for all six mode-specific runs. While the energy in any excited mode is always below the dissociation energy, the energy of the OH* mode is especially close to the dissociation energy being only ≈0.1 kcal/mol and ≈0.2 kcal/mol below the dissociation limits for the DMBE-IV and XXZLG PESs, respectively. In addition to mode-specific initial conditions, Marques and Varandas[70] also studied statistical initial conditions at one dissociative energy, which we repeat and extend to the XXZLG PES at a shifted total energy to preserve the excess energy above D_e. The resulting unimolecular decay curves are shown in Fig. 13 and the rate constants derived from them in Table VI. The DMBE-IV results are consistent[106] with the results of Marques and Varandas.

Table VI For $HO_2 \rightarrow H + O_2$, unimolecular dissociation rate constants (ps^{-1}), prefactors, and latency times (ps) under different initial conditions as a function of the total energy for the two different PESs. The energy in parenthesis is the amount of energy in excess of the D_e in Table I.

Initial conditions	Energy (kcal/mol)	DMBE-IV					Energy (kcal/mol)	XXZLG				
		A	k_1	B	k_2	t_0		A	k_1	B	k_2	t_0
OO*	58.79(3.95)	1.18	0.69			0.29	57.63(3.95)	1.18	0.47			0.41
OOH*	58.74(3.90)	1.00	0.76				57.57(3.89)	0.79[a]	0.49[a]	0.25[a]	1.04[a]	0.10
OH	58.26(3.41)	0.86	0.67				57.09(3.41)	0.47	0.45	0.41	12.5	
EMS	59.43(4.59)	1.00	0.89				58.27(4.59)	0.87	0.62	0.10	3.32	

[a] The least squares solution shows an rms fitting error that is a weak function of correlated small changes in k_1 and large changes in k_2. Many more trajectories would be needed to determine k_2 with a precision comparable to other entries in the table.

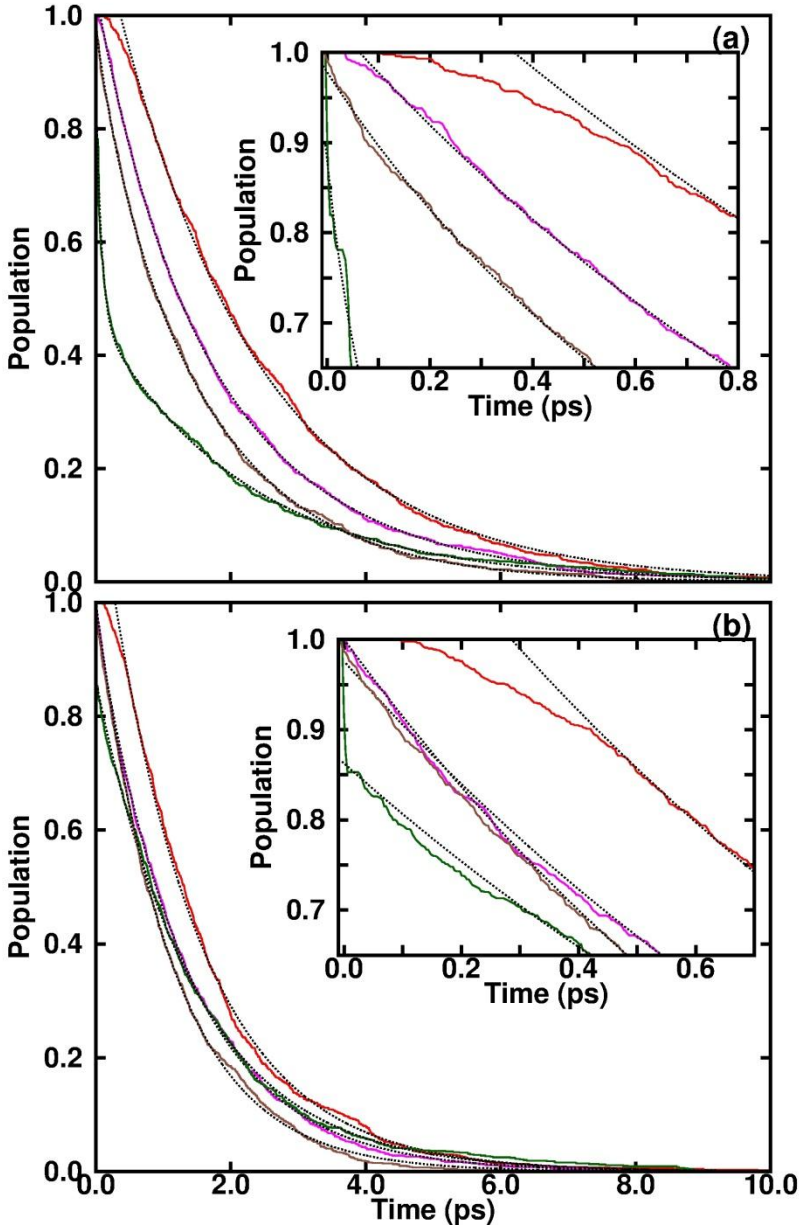

Figure 13 For the XXZLG (a) and DMBE-IV (b) PESs, the population decay as a function of time due to unimolecular dissociation to H + O_2 for initial conditions of mode-specific excitation [OO* (red), OOH* (magenta), OH* (green)] or for initial conditions selected using EMS (J=0) sampling (brown). The black lines represent the kinetics model fits. Inserts in each panel magnify the results at early times. See text for details.

Three points about the results in Fig. 13 and Table VI are worth noting. First, in Fig. 13 on both PESs there are significant early time behaviors that cause the mode-specific

population decays to generally be distinct from each other. The early time decay for each excitation mode will now be considered in the order OO*, OH*, and OOH*.

On both PESs, OO* has the most pronounced latency effects as detected by the procedure outlined in Appendix I. Comparisons of Fig. 13 and Table VI for dissociation with Fig. 4 and Table V for isomerization shows that the latency effects in OO* dissociation are similar in form but shorter than those for OO* isomerization on both PESs. Since insufficiently fast IVR rate constants are a likely source of this latency for isomerization, can IVR OO* rate constants at dissociation energies be estimated? For XXZLG, the linear extrapolation of the OO* IVR rate constants in Table IV produce a rate at the OO* dissociation energy of Table VI that is $\approx$0.4 ps^{-1}, less than but comparable to the OO* dissociation rate, a situation analogous to that in isomerization. This extrapolation is bolstered by the fact that, as discussed above, the slower EMS isomerization rate is thought to track the OO* IVR rate. As seen in Fig. 12, this slow rate is reasonably well approximated as a linear function of energy. Extension of this linear function to dissociation energies requires an extrapolation over half the energy range required with extrapolation using Table IV. The end result is a slow rate component of isomerization that is higher than but comparable to the dissociation rate. Thus the latency in OO* dissociation likely has the same cause as the latency in isomerization with OO*. The latency in OO* dissociation is shorter than that for isomerization because both IVR and dissociation rate constants are higher at the higher energy. For DMBE-IV, extrapolations from Table IV are dubious because, as commented above, the IVR rate constants in Table IV *decrease* with energy, a result most unlikely to persist at higher energies. Furthermore, there is no particular reason to correlate OO* IVR rate constants

on the DMBE IV with EMS isomerization rate constants. However, unlike the case for XXZLG, the results in Tables V and VI show that the OO* isomerization rate at the higher energy at which IVR was calculated is almost identical to the OO* dissociation rate. Thus if the IVR rate constants were to just flatten out with energy or modestly increase, the relationship of IVR rate constants to dissociation rate constants would be comparable to that for isomerization. Since IVR is faster for DMBE-IV than XXZLG, for both isomerization and dissociation the latency time is shorter for DMBE-IV than for XXZLG. Since this scenario does not involve a significant increase in any of the rate constants from that for isomerization, the latency time at dissociation is closer to that for isomerization than is the case for XXZLG.

For OH*, there is no latency time on either PES. However, as the inserts in Fig. 13 show, ≈10% of the population has the last inner turning point in negative time. In other words, 10% of the trajectories are ballistic, that is they are created with initial conditions that directly lead to dissociation.[104,33**107**] As seen in Tables I and III, the OH* excitation energy is only ≈0.2 kcal/mol below the dissociation energy and trajectories need to gain only a few tenths of a kcal/mol from the other two modes to dissociate. The OH* results on the DMBE-IV PES suggest that trajectories that have one inner turning point are much more likely to lose significant energy out of the OH stretch and begin a statistical repopulation of the phase space of the dissociative coordinate. However, the OH* results on the XXZLG PES suggest that a few turning points do not significantly decrease the energy in the OH stretch, allowing trajectories during each expansion phase of the OH stretch to acquire from the two other modes the small amount of energy they need to dissociate. The difference between the two PESs is undoubtedly a reflection of the order

of magnitude higher OH* IVR rate for DMBE-IV relative to XXZLG seen in Table IV for lower total energies. This difference is reflected in the fit to the two different dissociation decay curves. For DMBE-IV, the fitting error is not sensitive to the very early time behavior, so although the local fitting error is an order of magnitude larger than at any other time, the ≈5 fs duration of this very large local error is overwhelmed by minimizing the global error over the remaining 10 ps of decay. For related reasons, this initial short period is not recognized as a latency time by the procedure outlined in Sec. B.2 However, for XXZLG because the ballistic-like mechanism persists much longer, bi-exponential behavior results with the very rapid process having a rate constant of ≈13 ps^{-1} (see Table VI). Since the vibrational period of the O-H stretch is ≈10 fs, the inverse of this fast rate ≈75 fs implies that for half a dozen vibrational periods the OH* retains sufficient energy for the radical to undergo ballistic dissociation before enough energy is lost out of the OH stretch to require the statistical reassembly of sufficient energy[107] to dissociate.

For OOH*, there is no latency on the DMBE-IV PES. This is as expected because any reasonable extrapolation of the OOH* IVR results in Table IV to dissociation energies would have OOH* IVR more than an order of magnitude larger than the OOH* dissociation rate in Table VI. However, for XXZLG, doing the same would have IVR rate constants somewhat higher than but comparable to the OOH* dissociation rate constants. This would suggest, based on the arguments in the OO* case, a noticeable latency time for dissociation. There is in fact a latency time of only 60 fs, which is too short to influence the OOH* dissociation rate. The reason for such a small latency was discussed in connection with Figs. 7 and 8. These IVR figures show plots of mode

specific energies as a function of time, but the initial distributions in the figures show much less OOH energy and much more OH energy. The explanation is a massive redistribution of the initial mode-specific energy in tens of femtoseconds that cannot be distinguished within the time resolution of the figures. This is particularly prominent at the higher energy (see Fig. 8) where the OH mode appears to start with the asymptotic energy.

This short time redistribution is due at least in part to the breakdown in the normal mode approximation in the initial conditions preparation. However, the normal mode approximation is more valid for the O-O-H bending potential than it is for the stretches. For the stretches, compression leads to a rapid increase in repulsive energy not well described by the harmonic potential of normal modes. In the bending potential, both compression and expansion lead to a barrier through a symmetry plane (see Fig. 5) on all three PESs. In HO_2, the isomerization barrier is lower than, but comparable to, the barrier through the collinear geometry. Consequently, the harmonic potential is a somewhat better approximation of the anharmonic potential than it is for the stretches.

Beyond the breakdown of the normal mode approximation, the ballistic mechanism discussed above for OH* suggests a second very rapid energy transfer mechanism. A careful examination of the early time OOH* populations shown in the inserts in Fig. 10 reveals a behavior for OOH* isomerization similar to that seen in the inserts in Fig. 13 for OH* dissociation. A ballistic interpretation of these isomerization population features would have been clearer if a turning point definition in terms of the last O-O-H bend turning point had been used, because that would have led to negative lifetimes for rigorously ballistic trajectories as is the case for OH* dissociation. Isomerization might

very well accelerate energy transfer out of OOH*. The massive redistribution of energy in the OOH* IVR case occurs on the same timescale as ballistic isomerization, namely a few oscillations of the bending mode. This redistribution is much more pronounced in Fig. 8 for energies above dissociation than in Fig. 7 for energies below dissociation. This redistribution is also somewhat more pronounced for OOH* than for OH*. Finally, as seen in Figs. 7 and 8, the primary beneficiary of loss of energy out of OOH* is the OH mode which is the reaction coordinate for dissociation. Energy flow between bending and stretching modes can be especially facile; see, for example, Refs. 24(a) and 108. Thus the breakdown in the normal mode approximation and ballistic isomerization could both contribute to very early IVR and unexpected short dissociation latency times for OOH* on XXZLG. Furthermore, OOH* dissociation on XXZLG obeys bi-exponential behavior like that for OH* dissociation (see Table VI). The larger secondary rate constant for OOH*, although much smaller than the larger OH* rate constant and with half the amplitude, may be due to ballistic trajectories. In the case of OOH,* a probable source of the ballistic dissociative trajectories may well be ballistic isomerization which, as long as it lasts, initially pumps energy into the OH reaction coordinate to accelerate dissociation.[104]

The second conclusion that can be drawn from Fig. 13 and Table IV is that both PESs display, at best, modest mode-specific effects in unimolecular dissociation. While Fig. 13 has distinct curves depending on the mode excited, especially for XXZLG, those differences primarily reflect the latency and ballistic effects at early times discussed extensively above. As shown in Table VI, the dominant rate constants from the mode specific conditions are quite similar to each other with only an 8% (5%) maximum

deviation from the average for DMBE-IV (XXZLG). If plotted as functions of energy, these mode-specific unimolecular dissociation rate constants on both surfaces are reasonably consistent with the EMS dissociation rate constants at somewhat higher energies. In the case of isomerization, mode-specific effects for XXZLG, especially for OO*, are prominent and comparison with the IVR rate constants calculated at the same energy suggests competition between IVR and isomerization. For OH* and OOH* dissociation on both surfaces, IVR is generally fast enough to not be a substantial bottleneck to dissociation. For OO*, IVR at short times is slow enough to cause latency effects on both PESs. However, for DMBE-IV, Fig. 12 would suggest that the isomerization rate at the OO* dissociation energy will be on the order of 5 times higher than the OO* dissociation rate in Table VI. For XXZLG, as discussed previously, the slower component of the EMS isomerization rate is associated with the OO* isomerization rate and at the OO* dissociation energy it would be at least double the OO* dissociation rate in Table VI. To the degree that isomerization drives energy transfer, the IVR rate at early times that influences latency may not be the IVR rate operational over the bulk of the unimolecular dissociation after the latency time.

The third and final conclusion is that, as can be seen from Table VI, DMBE-IV produces unimolecular dissociation rate constants that are approximately 50% larger than does the XXZLG at the same excess energy over the dissociation energy. There have been four previous studies[55,78,79,80] that compared reactions on these two PESs but all of them were quantum dynamics studies of reactions (1a) and (1b), not the unimolecular reaction (1c) considered here. The more relevant studies[78,79] with H + O_2 as reactants predicted a lower reaction probability for XXZLG relative to DMBE-IV. The two other

studies[55,80] with O + OH as reactants found that only at intermediate energies was XXZLG more reactive. The results in Table VI are thus consistent with the general observation that XXZLG is less reactive than DMBE-IV. The quantum dynamics studies[81] also make clear that the reaction dynamics of HO_2 is dominated by quantum mechanical resonances unrepresented in classical trajectories that can result in large discrepancies in classical microcanonical and even canonical rate constants relative to their quantum analogs.

One last point concerning Table VI is the relationship between two bi-exponential cases in the table: OH* and EMS dissociation on XXZLG. (The XXZLG OOH* case is also bi-exponential but not to a degree sufficient to influence the following discussion.) The OH* case is described above as a combination of an early time ballistic-type dissociation process and the usual statistical dissociation process. Most likely the EMS behavior is bi-exponential because it contains a faint hint of the OH* ballistic process. If one assumes that the EMS distributed energy is approximated by an equal mix of OO*, OOH*, and OH* initial conditions, then the quite similar slow rate constants of OO*, OOH*, and OH* would be reflected in a similar EMS rate that has increased due to the higher total energy, and more particularly the relatively higher excess energy, for the EMS case. However the fast OH* rate constants should also be reflected in a fast EMS rate, with only 1/3 weight to the prefactor if we assume that each mode contributes equally, or ≈0.13. In fact the amplitude of the fast EMS rate is ≈0.10. This fast rate, while ≈5 times faster than the slow rate, is also about 3 times slower than the OH* fast rate. These differences are probably due to both absorbing the latency features of the OO* dissociation and the severity of approximating EMS by equal portions of OO*,

OOH*, and OH*. While this approximation is indeed severe, the EMS case produces some trajectories with last inner turning points prior to dissociation occurring at negative times. Even though the energy is statistically distributed, some trajectories do have OH energies comparable to the dissociation energy as the above interpretation suggests.

D. Conclusions

Three PESs for HO_2 have been comparatively examined for their characterization of equilibrium, isomerization, and dissociation energies, structures, and quantum variational vibrational frequencies, phase space structures using surfaces-of-section, and for IVR, isomerization, and dissociation trajectory dynamics. Two of the PESs, DMBE-IV[50] and XXZLG[53,54,55,56] have been fully described in the literature while the third surface, IMLS, has been only introduced in the literature[56] and is more fully described here. The two most recent PESs, XXZLG and IMLS, are based on higher quality and more systematically distributed *ab initio* electronic structure calculations than the DMBE-IV, a PES for HO_2 that has been used in many studies. The XXZLG and IMLS differ in the manner in which the electronic structure calculations are fit and a slight improvement in the quality of the *ab initio* method in going from XXZLG to IMLS. These two PESs are not without limitations with IMLS not being globally characterized up to the lowest dissociation channel and XXZLG displaying small violations of permutation symmetry and some fitting imperfections due to data sparsity.

The major conclusions of this study are:

- The IMLS and XXZLG are quite similar and of high quality. In comparison to experiment, the rms error of IMLS and XXZLG vibrational frequencies is ≈10 cm^{-1}

while the dissociation energy is too low by ≈0.2 kcal/mol for IMLS and ≈0.8 kcal/mol for XXZLG. Surfaces-of-section plots as a function of energy show consistent and comparable phase space structures for trajectories calculated on both the IMLS and XXZLG. Irregular phase space structure is first apparent at energies near the isomerization barrier. The structured nature of phase space gives rise to slow and roughly comparable IVR processes on both PESs. The relaxation of excited OO stretch is especially slow. Slow IVR in turn leads to prominent mode-specific effects in isomerization (on both PESs) and dissociation (only accessible on XXZLG). Since IVR is not fast enough to redistribute the initial vibrational energy, even for the initial conditions selected by using EMS isomerization, decay curves display double exponential behavior with the slower rate correlated with slow IVR rate constants. The likely source of this slow IVR is energy initially localized in the OO stretch. The longer it takes for a trajectory, with sufficient energy, to isomerize; the more probable it becomes that energy has been localized in the OO mode. As the OO mode becomes progressively enriched with energy the chance for isomerization decrease. In other words, isomerization acts as a filter that over time that can leave behind a population highly excited in the OO stretching mode.

- In detail XXZLG and IMLS do display somewhat different dynamics. The heights of the isomerization saddle points on the two PESs differ by ≈2.0 kcal/mol. (This is primarily due to sparsity in the XXZLG *ab initio* database around the symmetry plane of the surface and not differences in the underlying electronic structure calculations). Results sensitive to isomerization have an energy dependence shifted approximately by

that amount. The IVR rate constants computed on the two PESs differ by a factor of two for some initial conditions.

- The DMBE-IV PES displays many different characteristics relative to IMLS and XXZLG. It does not compare well to experiment with ≈100 cm^{-1} rms errors in vibrational frequencies and ≈0.7 kcal/mol overestimation of the dissociation energy. The surfaces-of-section plots show a more irregular phase space structure starting at energies that are half the isomerization barrier height. The IVR decay rate constants are nearly an order of magnitude faster than those for IMLS and XXZLG. As a consequence, mode-specific effects on isomerization and unimolecular dissociation are much less prominent and single exponential decay indicative of statistical behavior was found.

- The isomerization and unimolecular dissociation rate constants were determined with a kinetics model that identified early time latency effects by comparing the fitting error to the sampling error due to the finite number of trajectories in each simulation. This approach works reasonably well. In a related fashion, the IVR decay on all three PESs was analyzed with a kinetics model based on an asymptotic limit of equipartition of energy and on mode-to-mode energy transfer rate constants that are proportional to the amount of energy in the initial mode. This model also works well and represents the IVR features on all three PESs at energies above and below isomerization. However, the derived mode-to-mode rate constants were sometimes negative and therefore not physically meaningful, reducing the model to a phenomenological one. This may be due to the effects of resonances[13(a),108] on the energy transfer that are not accounted for in the model.

- Dissociation rate constants could only be determined on XXZLG and DMBE-IV. On both surfaces, latency times due to slow energy transfer and fast ballistic processes result in population decays that are distinctly different. However, after these early time effects, the dominant dissociation rate constants are at best only modestly sensitive to initial mode-specific excitations. As is true for bimolecular reactions, XXZLG has a lower dissociation rate constant than DMBE-IV at comparable energies above the dissociation limit.

On balance the IMLS and XXZLG are the PESs of choice with IMLS slightly superior because of better energetics and a more reliable description of isomerization. However, the IMLS at present cannot be used for dynamics studies at energies above dissociation without incorporating additional *ab initio* information.

E. Directions of Future Research

There are three directions of research that could be conducted on the dynamics and reactivity of HO_2. The first direction is investigating the quantum mechanical effect of tunneling which cannot be accounted for due to the classical nature of these studies. The effect of proton tunneling would be manifest by vibrational line splitting and by an enhanced rate of isomerization. There have been similar studies done with the hydrogen peroxyl anion.[109] The PESs of the anion and the radical share some similar topological characteristics, such as the symmetric hydrogen wells and a barrier to isomerization. On the anion PES the classical barrier to isomerization is ≈17 kcal/mol, which is a little under half the barrier height of the radical. At the isomerization saddle point the O-O bond length is elongated relative to the bond distance at the minima as it is with the radical. The higher barrier to isomerization on the radical could result in tunneling being

less important at lower energies. Previous studies of proton transfer studies with the anion found mode specific effects with excitation of the O-O-H mode contributing to the largest splitting factors and there was mode specific enhancement from excitation of the O-O mode. It would also be of interest to see if the lower isomerization barrier with the anion would lead to enhanced IVR compared to the IVR found with the radical.

The second direction of future research with HO_2 is related to the reactivity of the radical. The study conducted so far only looked at the dissociation of the radical in a very narrow energy range, but in this energy range modest mode specific effects were found and the lifetime of the radical was bi-exponential. A general study of the dissociation reactions, across a larger energy range, could give more insight into the nonstatistical dynamics of the radical. Such trajectory studies would be complemented by comparison to predictions from statistical rate calculations. Monte Carlo variational transition state theory (MCVTST), [110]given the barrierless nature of the H-O bond fission, would be useful for comparison since the study can be conducted on the same potential energy surface as the trajectory study, which would facilitate a direct comparison. A rate in MCVTST theory is calculated using[24(a),110(b)]

$$k(E) = \frac{1}{2}\left(\frac{\int d\Gamma \delta(H(\Gamma) - E)\delta(q_{RC} - q_c) \mid \dot{q}_{RC} \mid}{\int d\Gamma \delta(H(\Gamma) - E)} \right), \qquad (21)$$

where Γ is the phase space of the system, $H(\Gamma)$ is the Hamiltonian with no motion of the center of mass, q_{RC} is the reaction coordinate which is a function of the other coordinates q, q_C is the value required for reaction or a dividing surface and $\dot{q}_{TC}$ is the flux through q_C MCVTST rate constants have previously been interpreted as the upper limit to rate

constants calculated by trajectories. This means that the inequality $k(E)_{MCVTST} < k(E)_{traj}$ would be observed if the trajectories did not sample all of the energetically accessible phase space. Such a comparison would be useful in further understanding the dynamics of HO_2.

We investigated the energy transfer between the vibrational modes of HO_2 on three different PESs and found evidence of different timescales of relaxation which was shown to be dependent on the potential energy surface used.[111] However, in these studies the radical was not rotating. The final proposed direction of future research would focus on understanding the coupling between rotation and vibration. Frederick *et al.* [112] used trajectories to study OCS and SO_2 and found that large scale energy transfer between rotation and vibration (R-V) readily occurred. It is probable that centrifugal effects from rotation motion could influence the rate constants of isomerization and dissociation in HO_2.

IV. Dynamics of Hydrogen Peroxyl Radical in a Dense Gas Environment

A. Introduction

Understanding intermolecular energy transfer is an important step in the mechanistic understanding of H_2/O_2 combustion. We are interested in the collisional deactivation of HO_2, because the transfer of energy into and out of the internal motions of the radical will ultimately control whether the radical stabilizes or reacts. If the energized radical decomposes, it propagates the free radical chain; if it is stabilized by collisions, the free radical chain terminates. Kinetics modeling of HO_2 in combustion environments requires mapping out a large number of interconnected reaction pathways and the associated reaction and energy transfer rates, but possible inaccuracies in the time constants used in parameterizing combustion models can result in disagreements between theoretical predictions and experimental results.[113] Completely resolving all of the discrepancies between theory and experiment is a monumental task, so in hopes of contributing useful information about the rich chemistry of this radical, we continue with a "from the bottom up" approach on HO_2. In chapter III, which has been published,[111] we focused on the intramolecular dynamics of the radical and found complex dynamics and multiple timescales for energy transfer amongst the vibrational modes of the radical, which affect the unimolecular dissociation of the radical. In a similar spirit we next focus on studying the deactivation of a vibrationally excited HO_2 in a dense-gas environment.

We have chosen to simulate vibrationally excited HO_2 in an argon bath. Argon was selected as the solvent bath to avoid any possible phase change of the medium, since the

Ar bath was simulated at the temperatures and pressures above the experimental critical point.[114] The timescales for relaxation in a dense gas or liquid environment are commonly discussed in the context of two physical processes: T_1 for vibrationally deactivating collisions and T_2 for elastic collisions that dephase the motion of the solute.[115] The isolated binary collision approximation (IBC) is commonly used to calculate the timescale and behavior of T_1 as a function of density. Litovitz[116] was one of the first to apply a gas phase binary collision model in describing relaxation of an excited species in a liquid. The gist of this theory is that relaxation of a vibrationally excited species in a fluid can be described as a series of isolated collision events that are uncorrelated from one another. The effect of density on the energy transfer process can be described by a simple multiplication of an energy transfer probability with the collision frequency. The energy transfer probability is assumed to be independent of the internal energy of the solute. The collision frequency is calculated for the particular density or pressure of the system; at the simplest approximation the collision frequency is based on hard sphere model.

Early debates concerning the validity of IBC theory centered on neglecting the possible effects of many body collisions.[117] Herzfeld[118] pointed out that infrequent, high energy collisions would contribute the most to energy transfer into and out of the vibrational degrees of freedom, so solute relaxation consists of a large number of elastic collisions punctuated with occasional inelastic collisions. Davis and Oppenheim[119] revised the definition of IBC by using a pairwise radial distribution function (RDF) to implicitly include many body effects in the collision definition. Their definition of collision frequency is

$$v_c = 4\pi R^2 \rho g(R)\left(\frac{\kappa T}{\pi\mu}\right)^{1/2}, \qquad (22)$$

where $4\pi R^2$ defines a spherical shell at R, ρ is the system density, $g(R)$ is the RDF evaluated at R and $[\kappa T/\pi\mu]^{1/2}$ is the average thermal velocity representing the flux of the bath gas through the shell. They also emphasized that the only important collisions are those that explore high energy regions of the potential, along the same lines of reasoning as Herzfeld. Dardi and Cukier[120] put forth an interesting criticism that the selection of R in Eq. (22) is arbitrary and a sensible collision radius cannot be defined for both low and high density regions. They pointed to and reanalyzed the experimental work of Châtelet *et al.*[121] on the relaxation of H_2 and showed that the relaxation time constants at higher densities do not extrapolate to the low-density predictions.

The proposal that high energy collisions are the dominant source of relaxation was explored by Ohmine,[122] using simulations of excited ethylene in both Ar and H_2O. Ohmine found for Ar that high energy collisions, which explore the repulsive wall of the potential, dominate the relaxation, but multistep vibration-to-rotation (V-R) energy transfer followed by rotational energy transfer into the bath plays a role. Relaxation in water was found to involve much shorter timescales, which Ohmine attributed to the much stronger electrostatic interactions with the solute and the rapid response of the solvent to rearrangements in the system. Modifying the Ar-ethylene parameters to increase the magnitude of the interaction was found to accelerate the relaxation.

Schultz *et al.*[19a] studied the relaxation of azulene in a rare gas solvent and used the Davis and Oppenheim definition of collision frequency to understand the weak density dependence of the relaxation. They found that the implicit assumption of spherical

symmetry in this collision model led to an over-estimation of the actual density dependence of the relaxation. Using MD simulations with a rigid azulene embedded in a dense bath, they found that the anisotropy of the solute and the intermolecular potential led to a density independent packing above and below the azulene rings. They illustrated this anisotropy by calculating RDFs with explicit consideration of the spatial orientation of the solute. These RDFs indicate a much higher local density in the region above and below the plane of the molecule, particularly at higher densities. They suggest that the bath-gas packing could inhibit the energy transfer out of the azulene; because, the lowest frequency modes in the molecule involve out-of-plane motion that could be constricted by the packing of the bath gas atoms.

Schwarzer *et al.*[19b] studied the vibrational relaxation of excited azulene in several solvents by monitoring the decay of a UV absorption band. At higher pressures corresponding to liquid densities there was a fast initial decay of the signal, which became increasingly exponential-like at longer times. They found a nonlinear dependence between the relaxation times of azulene and solvent density in Xe, CO_2, and C_2H_6. They ruled out local heat conduction because aphysical adjustments to the model would have to be made to fit the data. They also reasoned that IVR was unimportant since the deviations from linear behavior occurred at different scaled collision frequencies for the various bath gases. In other words, they reasoned that IVR was not a limiting factor since the deviation from linear behavior did not occur at the same collision frequency. They proposed a simple adsorption model of azulene forming collision complexes with the bath gas which they posited would decrease the collision frequency and consequently inhibit energy transfer. They assumed that the reduction in the

collision frequency would be linearly dependent on the fractional coverage of the solute by the bath gas atoms. They found that the model gave agreement at lower densities, but failed at higher densities. They postulated that a change in the average energy transferred per collision could account for the failure of the model at higher densities.

Benzler *et al.*[123] did a similar UV absorption study to measure the relaxation of cycloheptatriene and found a nonlinear density dependence on the relaxation timescales as the solvent density increased. Along a similar line of reasoning as used by Schwarzer *et al.*,[19b] they concluded that local heating and IVR were not important factors in the nonlinear density dependence of the relaxation. They proposed a modified version collision-complex model of Schwarzer *et al.*, except that fractional coverage of the solute by the bath gas atoms was assumed to follow exponential dependence, rather than a linear one. This model gave acceptable fits to the experimental data and they noted that saturation of the spectral shift in the absorption band at higher pressure could be related to the effect of bath gas atoms clustering around the solute,[124] but additional work would be needed to confirm this model.

A series of trajectory studies[125] on the relaxation of excited azulene embedded in CO_2[125] and Xe[125(b)] were motivated by the density dependent relaxation time constants observed by both Schwarzer *et al.*[19c] and Benzler *et al.*[123] The first study by Heildelbach *et al.*[125(a)] consisted of simulations at two different pressures and two different temperatures. The azulene was simulated with two different PES models: one which reduced the number of intramolecular parameters and constrained C-H bonds and one which represented the full motion of the intramolecular potential. The CO_2 molecules were also represented with reduced and full PESs, which were used with the respective

reduced and full azulene PESs. The authors of this study focused on investigating gross relaxation time constants, local heating effects, collision frequency calculations and the local structure of the solvent. The second trajectory study[125(b)] was directed towards investigating how the vibrational modes of azulene coupled to the bath and how the time constants of energy loss occurred on a mode-by-mode basis.

Heildelbach *et al.*[125(a)] found in the first study that the gross relaxation time constants could be fit to a single exponential for both the low and high pressure simulations. It should be noted that the integration time for the lower pressure (250 atm) is ≈3 times shorter than the experimental timescale reported by either Schultz *et al*.[19a] or Schwarzer *et al*.[19b] The high pressure results were simulated for ≈1/8th of the reported experimental timescales of Schwarzer *et al*. for comparable pressures. The short timescales of these simulations and incomplete relaxation of the azulene preclude making any additional observations about the complete thermalization process. The relaxation was heavily influenced by whether full or reduced PES representations of the azulene and CO_2 were used. No evidence of local heating was found in examining the kinetic energy of the bath atoms in close proximity to the solute. The structure of the bath around the solute was found to be anisotropic, but the anisotropy above and below the plane of the azulene was related only qualitatively to the calculated RDFs and the explicit orientation of azulene was not considered. The RDFs calculated by Schultz *et al.*[19a] are much more illustrative of this anisotropy. The formation of bath gas-solute collision complexes, which were an earlier suggested cause of nonlinear density dependence of relaxation timescales, was not investigated

The interaction of the vibrational modes with the bath was the motivation for the second paper with the focus being primarily on the CO_2 bath. The simulation details were similar to those described in the first paper. The second study also contained details of additional simulations of azulene embedded in Xe. Heildelbach *et al.*[125(b)] found that energy loss from azulene in low pressure CO_2 occurred primarily through the low frequency modes, but at elevated pressures the higher frequency modes began to have a larger role in the relaxation process. The relaxation in Xe occurred primarily through the low frequency modes. In both cases the low frequency motion corresponding to out-of-plane modes of the molecule contributed the most to the energy transfer. They also found that the translational and rotational energy of the molecule relaxed rather quickly and that V-R transfer was unimportant in the relaxation. They also studied the IVR of isolated azulene using both simulated frictional forces and simple non-equilibrium distributions of energy amongst the vibrational degrees of freedom. They found that the relaxation of the modes in the isolated molecule happened on longer timescales and that non-equilibrium energy distributions could occur. They proposed that the solvent plays a role in facilitating the IVR, which ultimately led to single timescale for energy loss to the bath.

Paul *et al.*[19c] studied the relaxation of hexafluorobenzene embedded in a bath of N_2 at several densities using classical trajectories, at a single bath temperature of 298 K. The initial state of the C_6F_6 was vibrationally hot. The translational and rotational motion of the molecular was selected to be thermal. They found only minimal V-R energy transfer occurring during the relaxation process. The effect of the intermolecular potential on relaxation dynamics was examined and determined to have minimal effect. Most of the

energy lost by the solute was transferred to the translational and rotational degrees of freedom in the bath. The relaxation of the solute was well fit by a bi-exponential function with the asymptotic energy being treated as an adjustable parameter. Based on the asymptotic energy of C_6F_6 they concluded that a bi-exponential was best suited for lower densities and that additional exponential terms would be needed to properly model the higher density results. The groups of 96 trajectories that were simulated for each density were decomposed into smaller subgroups for analysis of the number of trajectories needed to converged results. It was found the same general behavior and fitting results could be obtained with a sample of 24 trajectories. Interestingly, it appears that Paul *et al.* were not aware that the nonlinear density dependence of the relaxation time constants they observed is quite similar to the trends seen in the results of Benzler *et al.*[123] and Schwarzer *et al.*[19b] An interesting contrast between these two studies is that the relaxation of C_6F_6 was found to be bi-exponential instead of single exponential.

To our knowledge there are only two studies of the collisional relaxation of vibrationally excited HO_2 and both are based on bimolecular trajectory scattering. The first study, by Brown and Miller,[126] focused on the deactivation of HO_2 by collisions with He as a function of bath temperature, total molecular energy, and total angular momentum. They concluded that there are two ways that HO_2 is vibrationally deactivated. Low temperature collisions (800 K) with a rotationally cold radical tended to cause an internal V-R energy transfer. Hotter collisions (2,000 and 5,000 K) with the bath gas with a rotationally excited HO_2 resulted in more direct loss of vibrational energy to translational energy of the radical.

The second study, by Varandas and Zhang,[127] focused on the deactivation of HO_2 by collisions with O_2. The relative translational temperature of O_2 colliding HO_2 varied from ≈300 K to ≈4000 K, and the rotational and vibrational states of O_2 were approximately assigned to the ground state. The initial vibrational state of HO_2 consisted of three vibrational energies (21, 36, and 48 kcal/mol) that were selected by quasi-classical excitation. The rotational temperature of HO_2 was ≈300 K. They found the dominant relaxation mechanism was V-R transfer, across all of the impact temperatures, and that collisions generally caused a V-R energy transfer. A mechanistic observation shared with Brown and Miller.[126] They also found that the shape of the distribution of energy transferred per collision is only weakly dependent on the initial vibrational energy of HO_2. Deactivation by V-T transfer was found to be more important for lower collision temperatures. The authors concluded vibration-vibration (V-V) transfer was a minor effect, because they found negligible post-collision excitation of the O_2 oscillator.

From the studies discussed above involving larger molecules, there is some evidence that the characteristics of vibrational relaxation by collisions with a bath gas change at higher pressures. Based on the experimental results of Schwarzer *et al.* and Benzler *et al.*, there appears to be a slowing of relaxation time constants with increasing bath density (pressure). Similar density effects on relaxation time constants were seen in the trajectory study by Paul, *et al.* We wish to determine if these density dependent effects are a general phenomenon. Combustion conditions can occur at elevated densities (pressures) and it is of interest to assess whether the IBC prediction of linear scaling of relaxation time constants as a function of system density holds true in the relaxation of small radicals and molecules important to hydrocarbon combustion. As an initial system,

we chose to study the relaxation of vibrationally excited HO_2 in a dense gas at a single temperature with varying densities (pressures). We suspect that the single-collision relaxation studies of HO_2 done so far cannot offer conclusive guidance about the timescales of the relaxation process, or whether the density of the bath would have any effect on the relaxation mechanism. The methods are outlined in Sec. B, the results in Sec. C, and the conclusions in Sec. D. Future studies are proposed in Sec. E.

B. Methods

We have investigated the relaxation of vibrationally excited HO_2 in a dense gas with classical trajectories. The methods used in the simulations are similar to the general strategies developed by others which have been used to investigate the effect of a dense gas environment on isomerization,[128] vibrational relaxation,[19(c),125] and unimolecular decay.[129]

All of the simulations were performed using the classical trajectory code GENDYN[38] modified for the dense gas simulations. The simulations of HO_2, embedded in a bath across a series of pressures (35, 70, 100, 500, 900, and 1300 atm), consisted of 125 Ar atoms with a single HO_2 radical. The bath temperature was 800 K and each ensemble consisted of 1,600 trajectories. Additional tests with larger bath sizes of 250, 500, 750 and 1000 Ar atoms were also completed at 1300 atm. The velocity Verlet integrator was used for integrating the equations of motion. The integration step size was 0.1 fs and the maximum integration time needed to relax HO_2 was determined from preliminary simulation results. The use of the velocity Verlet integrator was motivated by the low execution cost and long, stable integration behavior shown and discussed in Ch. II Sec. D. Phase space points of the system were recorded every 3 fs for analysis.

1. Intermolecular Potentials

The potential energy for the system is given by

$$V = V_{HO_2} + V_{Inter} + V_{Cell}, \tag{23}$$

where V_{HO_2} is represented by the XXZLG PES[54] and V_{Inter} is

$$V_{Inter} = V_{HO_2-Ar} + V_{Ar-Ar} \quad . \tag{24}$$

The intermolecular potential used was the Buckingham potential (Exp-6) where V_{HO_2-Ar} and V_{HO_2-Ar} are given by

$$V_{\mathrm{HO_2-Ar}} = \sum_{i \in HO_2} \sum_{j \in Ar} A_{ij} \exp(-B_{ij} r_{ij}) - \frac{C_{ij}}{r_{ij}^6} \tag{25}$$

and

$$V_{\mathrm{Ar-Ar}} = \sum_{i} \sum_{j>i} A_{ij} \exp(-B_{ij} r_{ij}) - \frac{C_{ij}}{r_{ij}^6}. \tag{26}$$

The heteroatomic parameters of A_{ij}, B_{ij}, and C_{ij} were obtained using

$$A_{ij} = \sqrt{A_{ii} A_{jj}} \tag{27}$$

$$B_{ij} = \frac{1}{2}\left(B_{ii} + B_{jj}\right) \tag{28}$$

$$C_{ij} = \sqrt{C_{ii} C_{jj}} \tag{29}$$

The values for the Buckingham parameters are given in Table VII. Micheal *et al.*[130] commented that the inclusion of electrostatic forces would lead to improved accuracy in modeling the intermolecular interactions of HO_2 with the bath gas atoms. However, such considerations are beyond the scope of the present study.

The term V_{Cell} refers to the spherical cell potential that was used to confine the simulation. This potential was developed by Marks *et al.*[131] and is a modified Born-Mayer function

$$V_{cell} = \sum_i \frac{\alpha r_i^2}{R^2} \exp(-\beta(R - r_i)) \qquad (30)$$

where α is the potential energy at the radius R of the cell, r_i is the distance of the i^{th} atom from the center of the cell, and β is a parameter that controls the steepness of the Ar- and HO_2-wall potentials. The radius of the cell varied with the desired pressure of simulation, while α and β were set to 75 kcal/mol and 6.5 $Å^{-1}$, respectively.

Table VII. Values of the intermolecular potential parameters.

	H[a]	O[a]	Ar
A (kcal/mol)	2202.082	69416.3	69600.0
B ($Å^{-1}$)	3.74	3.96	4.04
C (kcal mol^{-1} $Å^{-6}$)	32.5956	347.3498	1295.0

[a.] The parameters for H and O were taken from D. C. Sorescu, B. M. Rice, and D. L. Thompson, J. Phys. Chem. B **101**, 798 (1997).

The computational cost of evaluating the $(n/2)(n-1)+3n$ interactions scales as n^2, where the first term is the number of interactions between bath gas atoms, the second term is the number of interactions between the reactant atoms and bath atoms, and n is the number of bath gas atoms. The computational cost of the potential evaluations was minimized by only evaluating the potential energies between atoms that had an appreciable interaction. This was accomplished by smoothly turning off the potential and ignoring any interactions greater than a distance of $2.7\sigma_{ij}$ using a switching function that has two continuous derivatives. The form of this switching function is

$$S(\Delta) = \min[1, \max[0, 1 - 10g(r_{ij})^3 + 15g(r_{ij})^4 - 6g(r_{ij})^5]] \quad (31)$$

where

$$g(r_{ij}) = (r_{ij} - 2.5\sigma_{ij})(2.7\sigma_{ij} - 2.5\sigma_{ij})^{-1}, \quad (32)$$

where the σ_{ij} are the van der Waals radii and $g(r_{ij})$ is the progress variable of the switching function. The switching function was only applied when $g(r_{ij})$ was between 0 and 1. The value of the unmodified potential at the start of the attenuation ($r_{ij} = 2.5\sigma_{ij}$) is ≈3% of the magnitude of the potential well depth. At the end of the attenuation ($r_{ij} = 2.7\sigma_{ij}$) the unmodified potential is ≈2% of the magnitude of the potential well depth. The van der Waals radii of the Exp-6 potentials were located using bisection.[32] The use of the switching function should have only minor effects on the physical properties of the fluid.[30]

A neighbor list[132] was also used to further reduce the cost of the force calculations by excluding pairwise interactions outside the cutoff of $2.7\sigma_{ij}$. The organization of the neighbor list is shown in Table VIII. The neighbor list consists of two arrays: The first contains the number of neighbors of a particular atom and the second contains the identification number of the neighboring atom.

Table VIII. A schematic of a neighbor list using a two-array system.[a]

Atom index	$i^{th}(n)$
$i^{th}(1)$	23
$i^{th}(2)$	56
⋮	⋮
⋮	⋮
$i^{th}(n)$	k

$j^{th}(m)$	Neighbor Atom Index
$j^{th}(1)$	4
$j^{th}(2)$	6
⋮	⋮
$j^{th}(23)$	54
$j^{th}(24)$	12
⋮	⋮
$j^{th}(56)$	6
⋮	⋮
$j^{th}(k)$	m

[a.] Based on Fig. 5.5 in Haile, Ref. 30c.

Updating of the neighbor list was automated monitoring a buffer region out to $2.9\sigma_{ij}$ and defining a maximum displacement $r_{max} = 2.9\sigma_{ij}–2.7\sigma_{ij}$. When the sum of the two largest atomic displacements, measured from the most recent list update, became greater than or equal to r_{max} the list was updated.

Evaluation of initial conditions and a trajectory of 1 ps duration, calculated for 125 Ar atoms at 800 K and 1300 atm with one HO_2 and no reduction in the 8,125 pairwise interactions requires ≈310 s of cpu time. Applying the switching function and neighbor list in a similar trajectory reduced the average number of interactions to ≈1180, and the evaluation time of this trajectory was ≈80 s of cpu time.

In our previous work on the isolated radical in Ch. III, the gradients from the XXZLG were calculated by finite difference using a central difference formula. Also in that work we identified a cusp in the potential along a perpendicular bisector with the origin being the center of the O-O bond. In the region of the cusp, we symmetrized the potential and found it sufficiently smoothed the discontinuity. Unfortunately, this increased the computational cost of the surface. In an effort to improve the efficiency of our simulation

in the present work, the gradients of the XXZLG potential were calculated analytically in all regions away from the perpendicular bisector. In the region of the perpendicular bisector we evaluate the gradients by finite difference on a symmetrized surface as described in Ch. III. It was necessary to use the mixed numeric and analytic gradients because of the previously discussed deficiencies of the XXZLG PES, see Appendix II. Using analytic gradients offers an order of magnitude speedup over numerical gradients. The evaluation times for 10 ps trajectories including initial conditions that typically involved ≈675,000 potential and gradient calls are as follows: 356 s for analytic gradients with symmetrized, numerical gradients evaluated in the bisector region; 233 s for pure analytic gradients without symmetrization in the bisector region, a procedure that yields non-energy conserving trajectories; and 2847 s for numerical evaluation of the gradients everywhere including the symmetrized bisector region. The relative speed up from using the mixed analytic and numeric gradients is a factor of eight, while the full analytic gradients offer a speed up factor of 12. The loss of efficiency from the mixed gradient solution is due to the overhead of multiple potential energy evaluations needed for calculating both the finite-difference gradients and the symmetrization of the potential.

2. Initial Conditions

Simulations of vibrationally excited HO_2 in a bath gas were performed for a bath temperature of 800 K and pressures of 35, 70, 100, 500, 900 and 1300 atm. The initial conditions were done in three sequential steps: (a) Populate the simulation vessel with the desired number of bath gas atoms, followed by adjustment of the simulation sphere volume to obtain the desired pressure (done once for each pressure); (b) select the initial conditions of the HO_2; and (c) thermalize the bath gas. After the third step an NVE

trajectory was integrated using the velocity Verlet integrator for a predetermined time with a step size of 0.1 fs. The termination time of a trajectory was based on approximate thermalization times from early test simulations. The lower pressure ensembles were integrated for longer times to ensure sufficient relaxation of the HO_2.

a. Cell Size and Pressure

The following paragraphs are devoted to discussion of populating the reaction environment and adjusting the volume to obtain a desired pressure. The initial volume of the simulation vessel was calculated using the ideal gas law for the desired temperature and pressure. This volume was used as a starting point for populating the locations of the Ar atoms within the confining potential. The simulation cell was centered at the origin of a Cartesian coordinate frame and the center of mass of the radical was also positioned there. The equilibrium geometry of the radical was obtained using the Stepit[133] routine interfaced to GENDYN. The gradients and Hessians of the PES were calculated at this geometry to confirm this was the minimized structure of the radical.

The bath gas atoms were randomly inserted in the simulation cell using a simple acceptance/rejection scheme. A trial placement of a bath gas atom was done by randomly selecting the Cartesian coordinates of one of the previously placed atoms, adding a random displacement to all three Cartesian coordinates, inserting a test atom at the resulting position and evaluating of the potential energy. The maximum magnitude of random displacement in a single direction was taken to be half of the current cell radius. The new placement was accepted if the total potential energy remained less than zero; otherwise the placement was rejected and a new trial placement was generated. This

process was repeated until all of the bath gas atoms were placed in the simulation cell. A larger number of insertion rejections occurred for the higher pressure simulations, which required smaller simulation volumes. A smaller vessel volume has two effects on the insertion procedure: First, there was an increased chance of sampling of the repulsive spherical wall; second, the sequential placement of bath gas atoms eventually leads to packing of the bath gas in which insertions with positive potential energies are more likely. A simple solution to prevent large rejection rates was to start with a larger estimated ideal gas volume and correct for the overestimated volume in the pressure adjustment trajectory. The lowest acceptance rate for the cell population procedure was ≈20%.

After placing all of the bath gas atoms, a trajectory was integrated for 25 ps with a 0.1 fs step size and the pressure was equilibrated by changing the volume of the simulation cell. The HO_2 was held stationary at the center of the cell during this process. This pressure equilibration trajectory was started by assigning initial Cartesian velocities to the bath gas from one-dimensional Maxwell velocity distributions. Maxwell distributions were calculated by sampling a weighted Gaussian distribution. The weighting factor used is $(m_i \kappa T)^{1/2}$ where m_i is the mass of i^{th} atom, κ is Boltzmann's constant, and T is the temperature. The Gaussian distributions, for each Cartesian degree of freedom, were calculated using the *gasdev* subroutine from *Numerical Recipes*.[32] Velocities were assigned to the bath gas while the radical was held fixed at the center of the simulation cell by excluding it from the integration of the equations of motion; however, the pairwise interactions of the radical with the Ar atoms were calculated in the equations of motion to prevent any aphysical overlaps.

After selecting the initial velocities of the bath atoms, a trajectory was integrated and after each integration step the instantaneous average kinetic energy (temperature) was calculated using[30]

$$T_I = \frac{1}{3N\kappa}\sum \frac{p_x^2 + p_y^2 + p_z^2}{m}, \tag{33}$$

where N is the number of bath atoms, and p_x, p_y, p_z are the Cartesian momentum components of each atom. After evaluating the temperature, the pressure was calculated using[30]

$$P = \rho\kappa T_I - \frac{1}{3V}\sum\sum r_{ij}F(r_{ij}), \tag{34}$$

where ρ is the current number density, T_I is the result of Eq. 33, V is the current volume of the sphere at the value of R in equation 30, and $\sum\sum r_{ij} \cdot F(r_{ij})$ is the virial from the interatomic forces $F(r_{ij})$. Both the temperature and pressure were smoothed by a rolling average[134] with a 200 fs window (2,000 integration steps):

$$G_{roll} = \frac{1}{n}\sum_i^n G(n) + G(n-1) + ... + G(i) - G(i-1), \tag{35}$$

where each $G(i)$ is either an instantaneous temperature or pressure, n is the total number of samples in the window and G_{roll} is the value of the rolling average of either temperature or pressure. After every 1000 integration steps (100 fs), the rolling average temperature of the bath was compared to the desired temperature and if the absolute difference was greater than 10 K the momenta were scaled using

$$P_N = P_O\sqrt{\frac{T}{T_{roll}}}, \tag{36}$$

where P_N and P_O are the new and old momenta, respectively, and T is the desired temperature. After the temperature was tested the rolling-average pressure was compared to the desired pressure. If the absolute difference was greater than *5%* of the desired pressure then the volume of the reaction cell was resized to give the desired pressure. The Cartesian positions of the bath gas atoms were scaled to adjust for the change in volume using

$$q_N = q_O \left(\frac{V_N}{V_O} \right)^{1/3}, \tag{37}$$

where q_N and q_O are the new and old Cartesian coordinates, respectively, and V_N and V_O are the new and old cell volumes. The cell radius was smoothed with a 50 point rolling average using Eq. 37, as a function of the number of times it was adjusted. As stated above the cell volume was only adjusted if the absolute difference between the rolling average and desired pressure differed by 5%.

Figure 14 shows examples of the instantaneous (magenta curves) and rolling average values (black curves) for cell radius (a), temperature (b), and pressure (c) as functions of time. The temperature and pressure targets are 800 K and 1,300 atm. The instantaneous and rolling average values oscillate about the target values with the magnitude of the rolling average values being modestly smaller than the instantaneous values for both temperature and pressure. The rolling average of the cell radius reaches a smooth average within 1 ps. Frames (d-f) are an enhanced view on a shorter timescale of the results shown in (a-c). These plots (d-f) show that the large initial fluctuations in the temperature, pressure, and the cell radius are quickly smoothed and stable trends for all three properties are reached well within the maximum integration time of 25 ps. The cell

radius was fixed to the final value obtained at the end of the integration time. Similar results for the smoothing of the cell fluctuations, as those shown in Fig. 14, were obtained for all of the temperatures and pressures simulated in this work. The averaged volumes, radii, and bath densities are reported in Table IX.

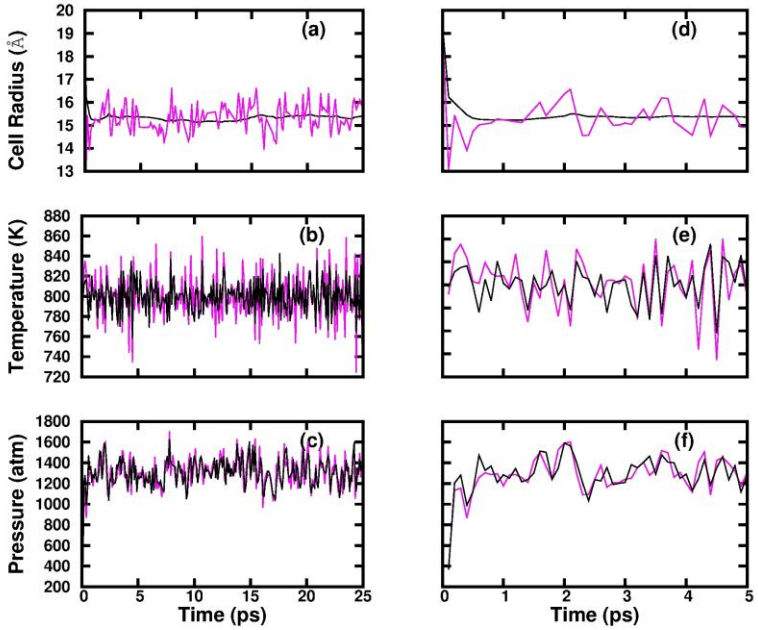

Figure 14 An illustration of the convergence of the cell properties during the pressure equilibration: (a) Cell radius; (b) Bath temperature; (c) Bath pressure. On a shorter timescale: (d) Cell radius (e) Bath temperature; (f) Bath pressure

Table IX. The radii, volumes, and gas densities of the simulated pressures.[a]

Pressure (atm)	Radius (Å)	Volume (Å^3)	Density (mol/L)
35	45.62 (4)[b]	398000 (1200)	0.522 (2)
70	36.26 (7)	120000 (1200)	1.039 (6)
100	32.34 (6)	141800 (700)	1.46 (1)
500	19.67 (9)	31900 (400)	6.51 (9)
900	16.78 (7)	19800 (300)	10.5 (1)
1300	15.36 (7)	15200 (200)	13.7 (2)

[a.] These values are the averages and uncertainties calculated from the sixteen sub-ensembles.

[b.] The numbers in parenthesis indicate the uncertainty in the last non-zero digit.

The volume of the cell decreased by a factor of three going from 35 to 1300 atm and the density increased two orders of magnitude. At the higher pressures of 900 and 1300 atm

there appears to be some signs of incompressibility with only modest changes in cell radius and density.

b. Solute Initial Conditions

The initial conditions of the radical were selected using (EMS)[34a,b] with a total internal energy of 40 kcal/mol and no restriction on the angular momentum of the radical. The bath atoms were held fixed at the positions reached at the end of step (a) and only the reactant was changed during the Markov walk. The intermolecular potential was ignored, so the surrounding bath gas had no effect on the selection of the internal state of the reactant. Any possible interatomic overlaps between HO_2 and Ar that could have occurred were dealt with in step (c). A warm-up walk of 250,000 steps in Cartesian coordinates was started from the equilibrium geometry in which all three atoms of HO_2 were allowed to move with random displacements. The maximum possible displacement of a single atom was 0.2 Å. The acceptance of a new displacement was governed by the weight in Eq. 7. At the end of the walk a set of momenta were sampled and scaled to obtain the desired energy as described in Ch. II. The final coordinates of HO_2 at the end of the Markov walk were used as the starting configuration for selecting the initial conditions of the next trajectory in the simulation. Subsequent walk lengths consisted of 100,000 steps that were taken between trajectories. The length of subsequent walks was selected based on the convergence of the coordinates and potential energy as a function of the number of steps in the Markov walk. The number of accepted moves of each walk was between 0.4 and 0.6.

Assigning the translational momenta is the next step in selecting the initial conditions of the solute. A set of Maxwell velocity distributions were sampled for each of the atoms in HO_2, then the center-of-mass velocity was calculated using

$$v_{cm} = \frac{\sum p_i}{\sum m_i}, \tag{38}$$

where p_i are the Cartesian momenta and m_i is the mass of the *ith* atom. The components of the sampled velocities that contribute to the internal motions of HO_2 were discarded. Translational momentum was then vectorially added to the momenta sampled at the end of the EMS procedure using

$$p_i = p_i - mv_{cm}. \tag{39}$$

The result is a rotationally and vibrationally hot reactant that has a thermal distribution of translational energy. The sampled kinetic energy of the center-of-mass motion was compared to the analytic Maxwell-Boltzmann distribution of kinetic energy given by

$$P(E_k) = 2\sqrt{\frac{E_k}{\pi(\kappa T)^3}} \exp\left(\frac{-E_k}{\kappa T}\right), \tag{40}$$

where E_k is the center-of-mass kinetic energy. An example histogram of the translation kinetic energy distribution is shown in Fig. 15.

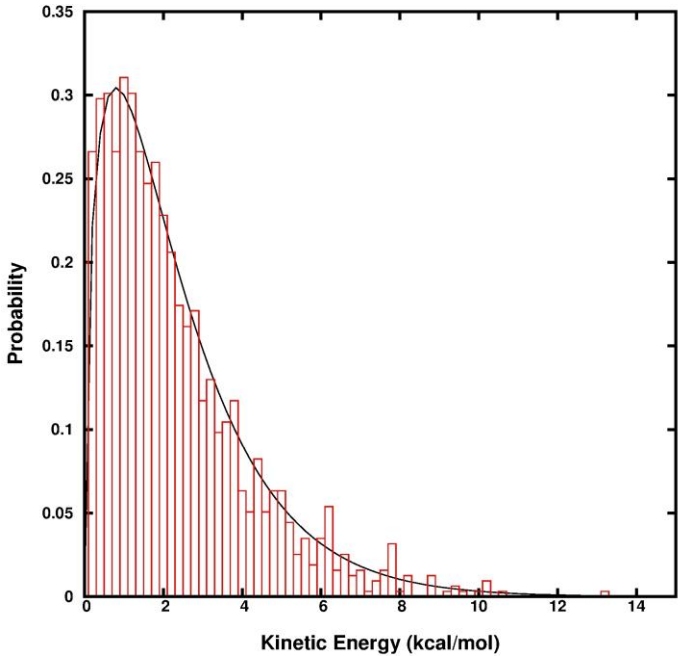

Figure 15 The histogrammed center-of-mass kinetic energy of HO_2 from the selection of the initial conditions at 800 K shown as red boxes. The analytic distribution for T = 800 K is shown as a solid black line for comparison.

c. Final Thermalization

The conformation of the radical was changed by the selection of microcanonical initial conditions described in Sec. B.2b, without consideration of the configuration of the surrounding bath gas. Interatomic overlaps between the HO_2 and Ar atoms are a possible consequence that could occur due to this neglect. To correct for this possibility, the bath gas atoms were re-thermalized with a new set of velocities using the procedure as described in Sec. B.2a. The reactant was again held fixed, as described in Sec. B.2a but retaining the phase space point selected during Sec. B.2b. A thermal trajectory was integrated for 25 ps with the temperature controlled in the same manner as it was in Sec. B.2a. The final Cartesian coordinates of the bath-gas atoms were stored at the end of

each thermalization trajectory, and used as the starting configuration for subsequent thermalization trajectories in the simulation sequence.

3. Energy Transfer

Analysis of the energy transfer between the hydrogen peroxyl radical and the bath was done by decomposing the Hamiltonian of the radical into the translational, rotational, and vibrational components. The separation of linear momenta of the radical is exact. After removing the translational component a zeroth-order separation of rotational and vibrational energy was assumed

$$H_{RV} = H_R + H_V, \tag{41}$$

where H_R the was calculated using

$$H_R = \frac{1}{2} L \bullet I^{-1} \bullet L. \tag{42}$$

L is the whole-body rotational angular momentum

$$L = r \times p, \tag{43}$$

and the instantaneous moment of inertia was calculated using

$$I = \begin{bmatrix} m(y^2 + z^2) & -mxy & -mxz \\ -mxy & m(x^2 + z^2) & -myz \\ -mxz & -myz & m(x^2 + y^2) \end{bmatrix}. \tag{44}$$

This allows the vibrational energy to be defined as

$$H_V = H_{RV} - H_R . \tag{45}$$

Frederick *et al.*[112] described several different ways of separating the vibrational and rotational degrees of freedom in molecular systems and recommended using Eq. 42, because the definition is independent of the coordinate system.

The vibrational energy was calculated using Eqns. 42-45 as a function of time and the asymptotic thermal energy $E(\infty)$ was subtracted. We refer to the vibrational energy above $E(\infty)$ simply as "excess-vibrational energy." We assume that two factors will govern the behavior of $E(\infty)$ in the limit of infinite time: First, the solute will have the same average thermal energy as the bath. Second, in this limit the radical will have lost sufficient energy such that the trajectory is only sampling harmonic portions of the PES and that the contribution of the potential to equipartion[135] will be $\frac{1}{2}\kappa T$. The definition of $E(\infty)$ is $3\kappa T$ for vibrational motion and $\frac{3}{2}\kappa T$ for rotational motion. Since we are simulating a finite system, the energy loss from the radical will cause the bath to heat to a new asymptotic temperature; consequently, we assigned T to be the time-dependent ensemble average temperature of the bath gas.

The resultant curve, representing the decay of the excess-vibrational energy of the radical to $E(\infty)$, was fit to a bi-exponential function

$$E(t) = A\exp(-k_1 t) + B\exp(-k_2 t), \tag{46}$$

where A and B are calculated by linear least squares subject to the constraint $A+B = 1$, and k_1 and k_2 are time constants fitted using standard nonlinear methods.[32]

C. Results

1. Thermal State of Bath

The first test of the simulation method was to show that the equilibration of the bath resulted in a stable temperature and pressure and that the Maxwell-Boltzman distribution of speeds was adequately sampled by the bath gas. These tests were done to ensure that there were no abnormalities in the implementation, since previously Marks *et al.*[131] had shown that satisfactory results for these properties can be obtained using the sphere potential with a smaller number of bath atoms. We tested two temperatures above and below 800 K for additional verification. The initial conditions of HO_2 were selected so that 10 kcal/mol was divided between the rotational and the vibrational degrees of freedom and the translational velocities were selected from a thermal distribution, as described in Sec. B.2. The magnitude of the internal energy was of HO_2 was arbitrarily selected to be smaller than the value (40 kcal/mol) that used in the actual relaxation studies. This choice was made to minimize potential heating of the bath gas from energy transfer out of HO_2. It should also be pointed out that the results reported in this section are from individual trajectories.

Figure 16 (a-c) contains of histograms of the Maxwell-Boltzmann speed distribution calculated from the bath gas speeds sampled during a trajectory, the analytic function is also plotted as dashed lines for comparison. These plots were generated from the results of individual trajectories of 125 Ar atoms and a single HO_2.

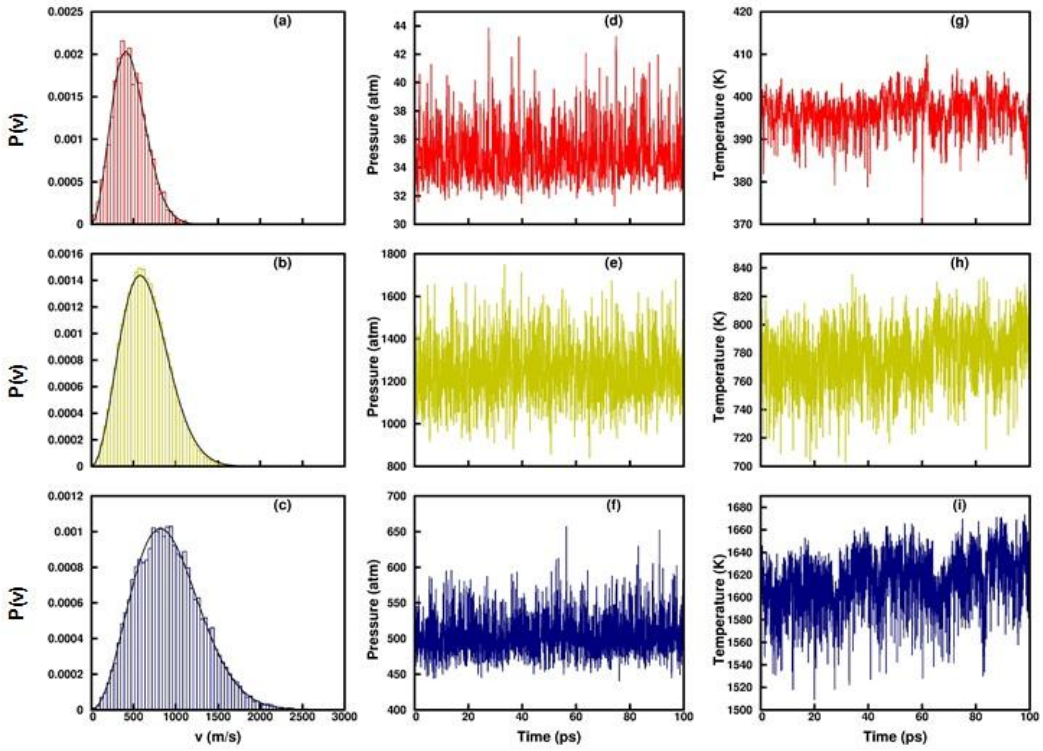

Figure 16 Thermal state and pressure of the bath for a variety of sampled temperatures. (a) Maxwell-Boltzmann bath gas speed distribution: (a) 400 K; (b) 800 K; (c) 1600 K. Instantaneous pressures: (d) 35 atm; (e) 1300 atm; (f) 500 atm. Instantaneous temperatures: (g) 400 K, (h) 800 K, (i) 1600 K.

The velocity histograms are in excellent agreement with the analytic distributions. The temperature and pressure calculated using Eqns. 33 and 34 are shown in frames (g-i) and (d-f), respectively. The fluctuations in the pressure are a function of both the temperature and the magnitude of the interatomic forces (see Eq. 34), so as the temperature and density of the system increase the magnitude of the pressure fluctuations also increases. However, it is either the time average or ensemble average that has physical meaning. The time average pressures going down the middle column of Fig. 16 are: 34.8 atm, 1242.1 atm, and 506.6 atm and the root mean square (rms) fluctuations are: 1.8, 130.4, and 26.3 atm, respectively. The time average temperatures in the right hand

column of Fig. 16 are: 396.8 K, 777.1 K, and 1615.8 K and the rms fluctuations are 6.0 K, 20.0 K, and 23.4 K, respectively. The increased fluctuations, in the temperatures and pressures, at higher densities could be indicative of increased incompressibility of the bath gas. This incompressibility can be identified as an increased number of multiple, non-negligible interatomic interactions. Some evidence of this incompressibility can be seen in the rms fluctutations of the HO_2-Ar interactions calculated by Eq. 25: The rms fluctuations in the HO_2-Ar interactions are the following: for 400 K and 35 atm, it is 0.16 kcal/mol; for 800 K and 1300 atm, it is 0.90 kcal/mol; and for 1600 K and 500 atm, the rms is 0.79 kcal/mol. The multiple, non-negligible interactions cause more fluctuation in the kinetic energy of the system, which is used to define a temperature in Eq. 33. The virial term, $\sum\sum r_{ij} \cdot F(r_{ij,})$, used in calculating the system pressure in Eq. 34, also fluctuates more, which combined with the modulation in temperature could be the cause the observed fluctuation in pressure.

There is a slight upward drift in the temperature of the bath for the 800 K (frame h) and 1600 K (frame i). The drift is due to the bath gas atoms gaining energy from HO_2 via collisions during the course of the trajectory. The expected thermal energy of rotational and vibrational energy of HO_2 is $4.5\kappa T$. For the 800 K trajectory the temperature of drops as low as ≈720 K and the relative internal energy, 10 kcal/mol, of HO_2 at this temperature is $\approx 6.9\kappa T$, so it is probable that energy will transfer to the bath gas atoms and cause the overall temperature of the simulation to rise. Similar analysis 1600 K trajectory shows the same behavior, the instantaneous temperature drops as low as ≈1510 K and the relative internal energy of HO_2 is $\approx 4.6\kappa T$, so again energy transfer out of HO_2 can occur. The 400 K trajectory shows no overall temperature drift because the activating and

deactivating collisions of HO_2 with the bath gas atoms effectively canceled each other out over the course of the trajectory.

A way to decrease the magnitude of the fluctuations is to increase the number of bath gas atoms. If one assumes that the reduction in error follows the relation of $1/\sqrt{N}$, where N is the system size, reducing the fluctuations in Fig 16 by half would require a system size of 500 Ar and reducing the error to a quarter of its value would require 2000 Ar. These results taken as a whole show that the procedure described in Sec. B.2b was sufficient in setting the thermodynamic state of the bath.

2. Energy Transfer Results

The goal of this study is to detemine whether there is any pressure effect on the relaxation of excited HO_2. The integration time lengths were determined from extrapolation of preliminary results. The 35 and 70 atm trajectory ensembles were simulated for 1700 ps, the 100 atm ensemble was simulated for 750 ps, and the 500, 900, and 1300 atm ensembles were simulated for 500 ps. The effect of the system size was studied by varying numbers of bath gas atoms in the simulation vessel. The number of bath gas atoms was varied from 125 up to 1000 Ar atoms and these simulations were done at 1300 atm and 800 K.

a. Vibrational Relaxation Pressure Dependence

Figure 17 contains plots of the vibrational energy of HO_2, the bath temperature, and the bath pressure as functions of time. All of these quantities were scaled to a range of 0 to 1 relative to their respective values at *time = 0*. The initial conditions of HO_2 were

selected so that the translational motion was thermal and 40 kcal/mol was distributed between the rotational and vibrational degrees of freedom. Both the bath temperature and pressure, for all of the trajectory ensembles, show a relative increase with respective to the values at *time* = 0. The final relative increase in both temperature and pressure, for all of the ensembles, is ≈10%. The increase in both temperature and pressure is due to the Ar atoms gaining energy as the HO_2 is deactivated by collisions.

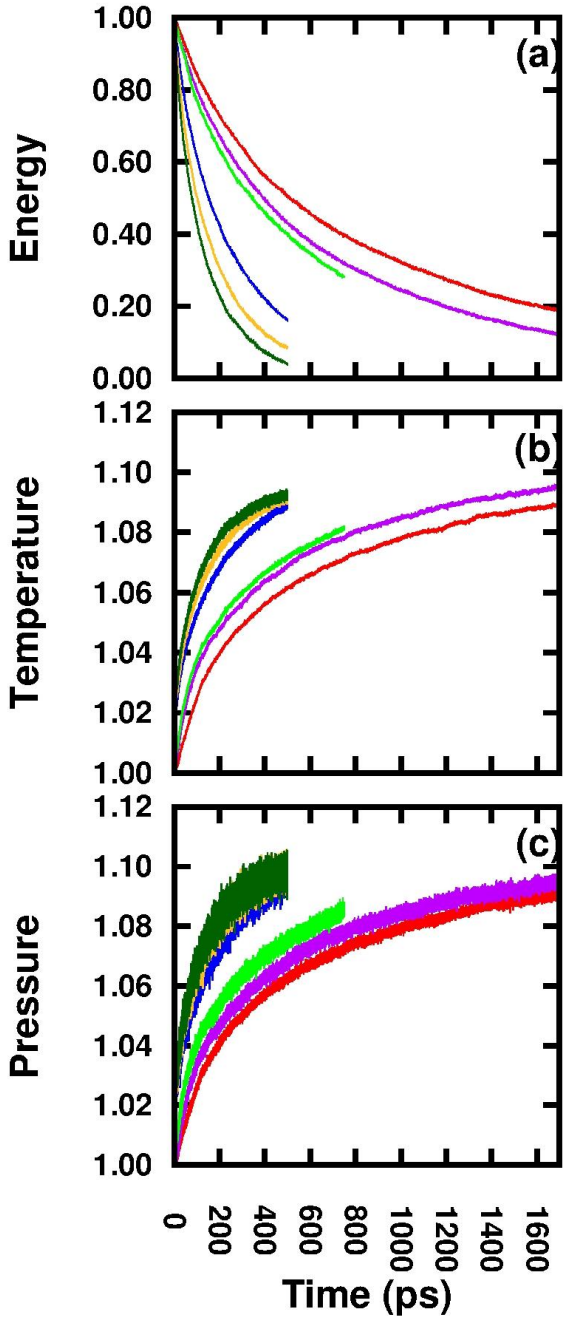

Figure 17 . The results of HO_2 with 40 kcal/mol of excess internal energy relaxing in a bath of 125 Ar atoms at various pressures. The scaled: (a) vibrational energy, (b) temperature, and (c) pressure. The line coloration: 35 atm, red; 70 atm, magenta; 100 atm, green; 500 atm, blue; 900 atm, yellow; 1300 atm, dark-green.

Figure 18 contains plots of the energy decay curves and single exponential fits on a semi-log scale. The amplitude of the single exponential fits was constrained to unity. It is apparent that the vibrational relaxation is not well fit by a single exponential and two relaxation timescales are present. Close examination of the curves show indicate that there are two appearant linear regions. An example of the transition from the first relaxation timescale to the second can be seen with the red curve at ≈ 425 ps. This nonlinearity in the energy relaxation curves exists in all of the simulated results.

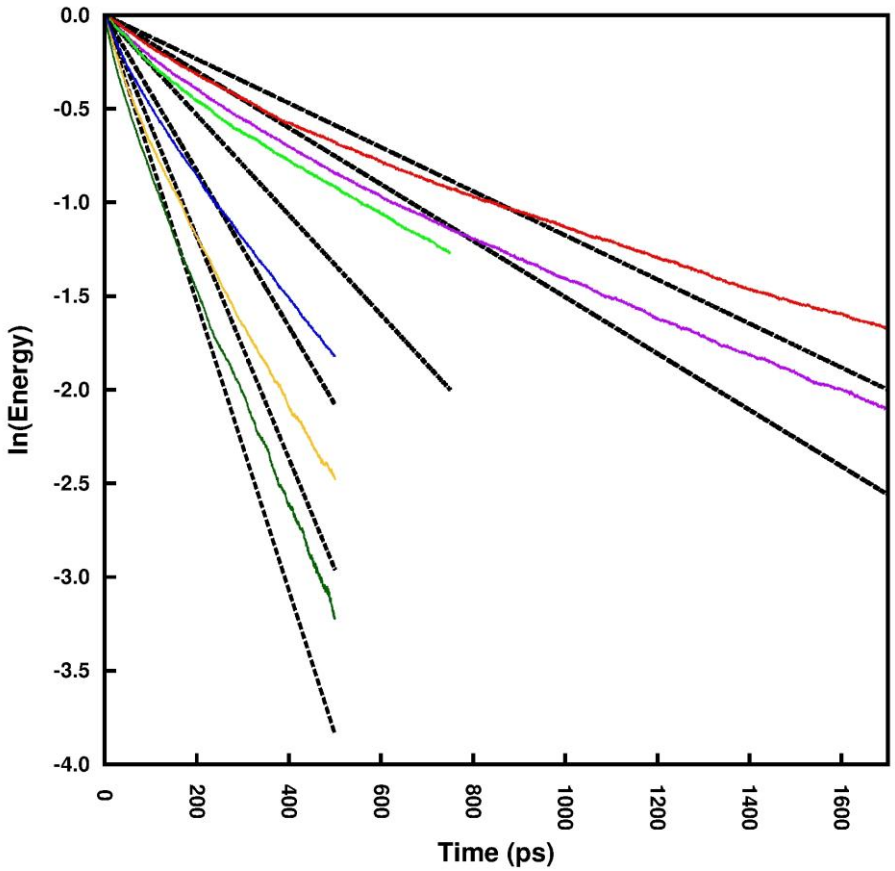

Figure 18. Plots of the decay of excess-vibrational energy above the thermal limit (See, Fig. 17a) as a function of time on a semi-log scale: single exponential fits (dashed-black); 35 atm, red; 70 atm, purple; 100 atm, light-green; 500 atm, blue; 900 atm, yellow; and 1300 atm dark-green.

The results of fitting to Eq. 46 are shown in Fig. 19 and it appears that the bi-exponential fit is satisfactory. HO_2 loses at least 70% of the initial vibrational energy for all of the pressures simulated and for the highest pressure the vibrational energy falls by ≈95% within the simulated time.

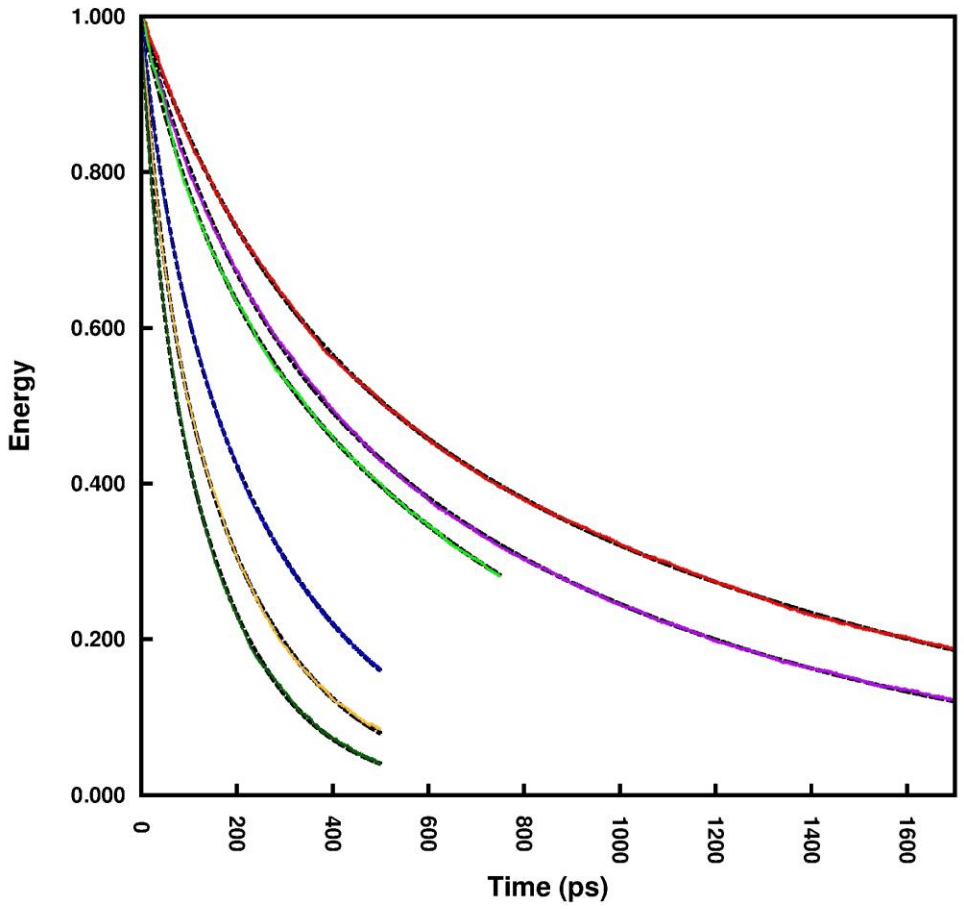

Figure 19. Same as figure 18, except scale is not semi-log and fitted curves are from Eq. 46.

The fitting parameters and uncertainties calculated in fitting the curves in Fig. 17a to Eq. 46 are tablulated in Table X. The asymptotic limit of zero required for fitting the curves in Fig. 17a was done by subtracting off the thermal energy of the radical, which is a function of the bath temperature shown in frame 17(b), with an appropriate conversion by equipartion, described in methods Sec. B.3. As discussed in the methods (Sec. B.3),

the fitting of the energy decay curves was done with *A* and *B* determined by linear least-squares with the constraint of $A + B = 1$ and k_1 and k_2 treated as adjustable parameters. The error bars in Table X were generated by bootstrapping[48] the 1600 trajectories of each ensemble. In total, 5000 resampled groups of 400 trajectories were generated for each pressure ensemble. The excess-vibrational energy curves, calculated from the resampled data sets, were also fit to Eq. 46. The bootstrapping was done so that each trajectory could only be sampled once per resampled group.

Table X. Parameters and error bars from fitting the vibrational relaxation of HO_2 to Eq. 46

P (atm)	ρ (mol/L)	A	B	σ_{AB}	k_1[a]	σ_{k1}	k_2	σ_{k2}
35	0.52	0.34	0.66	0.07	0.0038	0.0008	0.0007	0.0001
70	1.04	0.34	0.66	0.07	0.0048	0.0011	0.0010	0.0001
100	1.46	0.23	0.77	0.07	0.0081	0.0017	0.0013	0.0001
500	6.51	0.21	0.79	0.06	0.0167	0.0049	0.0032	0.0002
900	10.47	0.26	0.74	0.06	0.0221	0.0051	0.0045	0.0003
1300	13.66	0.26	0.74	0.05	0.0301	0.0075	0.0058	0.0003

a. The unit of k_1, k_2 and the respective errors is ps^{-1}. The amplitudes *A* and *B* are dimensionless.

Figure 20a contains plots of the amplitudes and time constants found in Table X as a function of the bath gas density. The change of the independent variable to density was made to faciliate comparison with the results of Paul *et al.*[19c] Both time constants grow with increasing bath density, but there is a change in behavior near ≈1-2 mol/L as shown by the blue curves. Also at this density the amplitudes of the exponentials shown as the red curves oscillate and the amplitude of the primary exponential increases, while the amplitude of the smaller exponential decreases. However, the error bars of the amplitude show a fair amount of overlap across the density range indicating that the amplitudes

have a weak density dependence. The amplitude of the slower exponential is consistently larger than that of the faster exponential.

The vibrational relaxation results of Paul *et al.*[19c] are included in frame (b) of Fig. 20 for comparison with our results in frame (a). Plots of this sort were not reported by Paul *et al.,* so we have plotted their data in Table III of Ref 19c as a function of the reported bath densities. The reported results are from simulations of vibrationally excited C_6F_6 embedded in an N_2 fluid described with periodic boundary conditions. Paul *et al.* fit the relaxation of excess-vibrational energy was fit to the bi-exponential function where $E(\infty)$ was treated as an adjustable fitting parameter. These simulations also span a density range four times the maximum density we investigated. The magnitude of the relaxation time constants for C_6F_6 are larger than those reported by us for HO_2 by about a factor of three to five. We believe this difference could be due to C_6F_6 having only low frequency modes that will readily couple to the motion of the bath gas. Despite the difference in the magnitudes of the time constants there are striking similarities in the relaxation results of HO_2 and C_6F_6. The amplitudes shown in Fig 20b exhibit a density dependence, but in the same range of densities we simulated, the amplitudes reported appear to exhibit only a weak-density dependence. It is interesting that the relaxation results for very different chemical species are well fit by a bi-exponential function. While there are differences in the magnitudes of the relaxation timescales, both the C_6F_6 and HO_2 results show two different regions of linear dependence with respect to bath density The turnover from one linear region to the other in our results occurs at ≈1 mol/L and at ≈10 mol/L for the results of Paul *et al*. It is possible that the size of the molecule plays a role in determining the density at which this turnover behavior occurs. The turnover effect is somewhat

appearant with the dashed green line in frame (b), but it is less clear when examining the solid green curve. It is worth noting that a turnover can be seen in the experimental relaxation time constants obtained by Schwarzer *et al.*[19b] and Benzler *et al*.,[123] and in both of these studies the turnover occurred at a density of ≈10 mol/L. Additional simulation results for C_6F_6 at a lower density range are needed to better characterize the density at which the turnover behavior occurs.

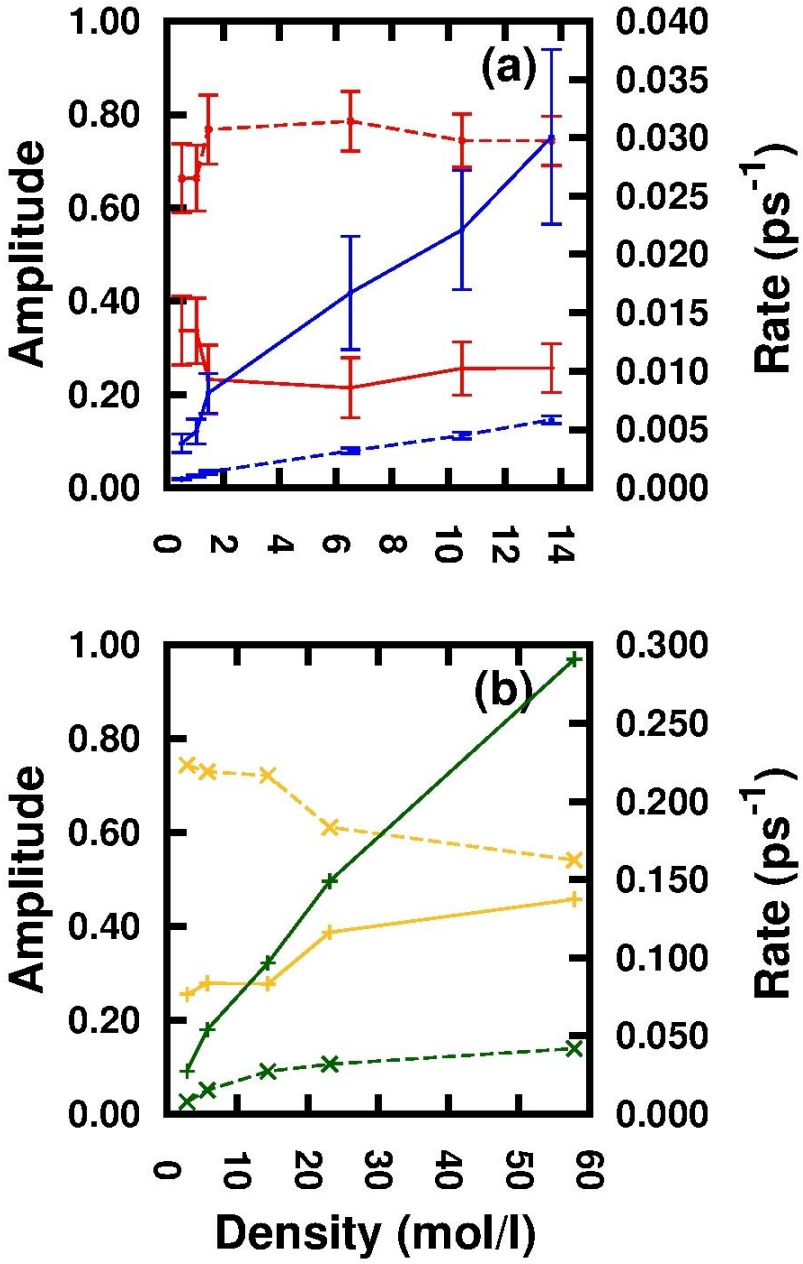

Figure 20. Plots of the fitting amplitudes and time constants in Table X as a function of bath gas density. The lines are intended to guide the eye: (a) the solid-blue line corresponds to the larger time constant and the amplitude is matched with the solid-red line. The dashed-blue line corresponds to the smaller time constant and the amplitude is matched with the dashed-red line; (b) the results from Paul *et al.*[19c]: (a) the solid-green line corresponds to the larger time constant and the amplitude is matched with the solid-yellow line. The dashed-green line corresponds to the smaller time constant and the amplitude is matched with the dashed-yellow line. The symbols in (b) were included to emphasize the densities specific densities of the simulations.

Our low-pressure time constants are shown on a much larger scale in Fig. 21. Linear fits are shown as the black lines in this figure. These fits to the three data points were obtained with the intercept fixed at zero. The zero intercept is the limit of no collisions and consequently no energy transfer. The fitted lines lie outside of the bootstrapped error bars reported at the lowest density. An overlap of linear fits with the data would have been supporting evidence of a linear proportionality between the time constants and the bath gas density, which is an important assumption in IBC. We think that the increase in both temperature and pressure of the simulation drives the relaxation of HO_2 and leads to an overestimation of the time constants. This possible finite-size effect motivated a study of how the system size affected the relaxation process.

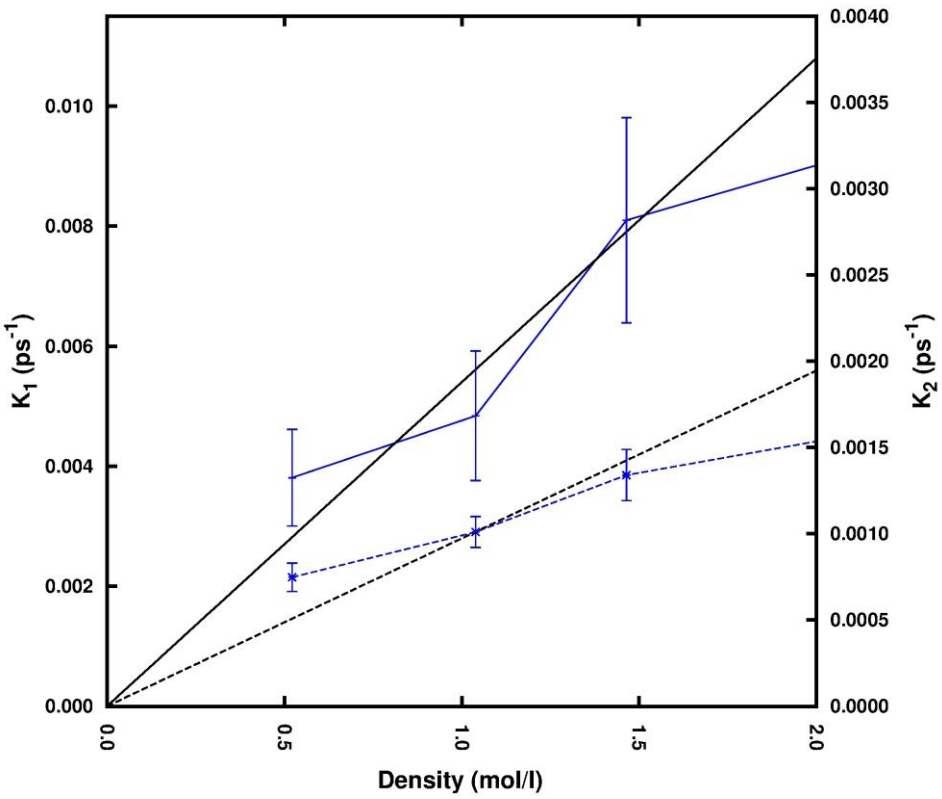

Figure 21 The low-pressure time constants k_1 and k_2 as a function of pressure on a smaller scale than that shown in Fig. 19. The larger time constants are plotted relative to the axis on the left and the smaller time constants are plotted relative to the axis on the right. The solid and dashed-black lines correspond to a linear fit of the time constants subject to the constraint of zero energy transfer in the limit of zero pressure.

b. Finite Size Effects

The simplest prescription to avoid the finite size problem is to increase the system size until the results of interest no longer change. However, increasing the bath comes with a tradeoff of time, because the computational cost of the simulation scales with the system size. For our particular study, we assume that the excited HO_2, started with 40 kcal/mol of internal energy, is relaxing to thermal equilibrium. In the long-time limit, the internal energy of the radical predicted by equipartition would be $4.5\kappa T$ or 7.2 kcal/mol at 800 K. This means that ≈33 kcal/mol of excess energy would be transferred to the bath

in the limit of complete thermalization. The predicted increase in the bath temperature for a monoatomic gas is $\approx 2N\kappa/3E_k$, so doubling the number of bath atoms would reduce the rise in temperature by half. To study the effect of the number of Ar atoms on the relaxation, we did additional simulations of HO_2 relaxing with increasing numbers of bath gas atoms with initial conditions selected described in Sec. B.2b. at 800 K and 1300 atm. We chose to simulate several system sizes to see how the temperature increase progressed: for 125 atoms the increase would be ≈90 K; for 250 atoms, ≈45K, for 500 atoms, ≈22 K, for 750 atoms, ≈15 K, and for 1000 bath atoms, ≈11 K. We attempted to partially account for heating of the bath on the relaxation process by making the asymptotic energy of HO_2 a function of the bath temperature. However, this does not account for the associated rise in pressure that occurs with heating (see, Fig. 17c).

The results from the simulations with increasing numbers of Ar atoms are shown in Fig. 22. The approximate temperature increase shown in frame (a) agrees fairly well with the predicted increase for each of the numbers of bath gas atoms. The increase in the simulation temperature from smallest to largest number of bath gas atoms is: 36, 18, 12 and 9 K. The increases in pressure shown in (b) are a possible indication as to why the smaller simulations have larger relaxation time constants. The pressure calculated by Eq. 34 has explicit temperature dependence in the ideal gas term $\rho\kappa T$. The increase in temperature would cause a corresponding increase in pressure, or the collision frequency between the radical and the bath, which would likely manifest as a faster decay of the excess-vibrational energy with smaller system size. The results in frames (c) and (d) seem to support this fact with the results from the smaller bath simulations relaxing to a much lower final excess-vibrational energy. The HO_2 embedded in 125 Ar atoms is ≈4%

above the equilibrated limit, see Fig. 19, while the HO_2 embedded in the 1000 Ar is ≈10% above this limit. We also fit the curves in Fig. 22d to Eq. 46 and the fitting results are tabulated in Table XI.

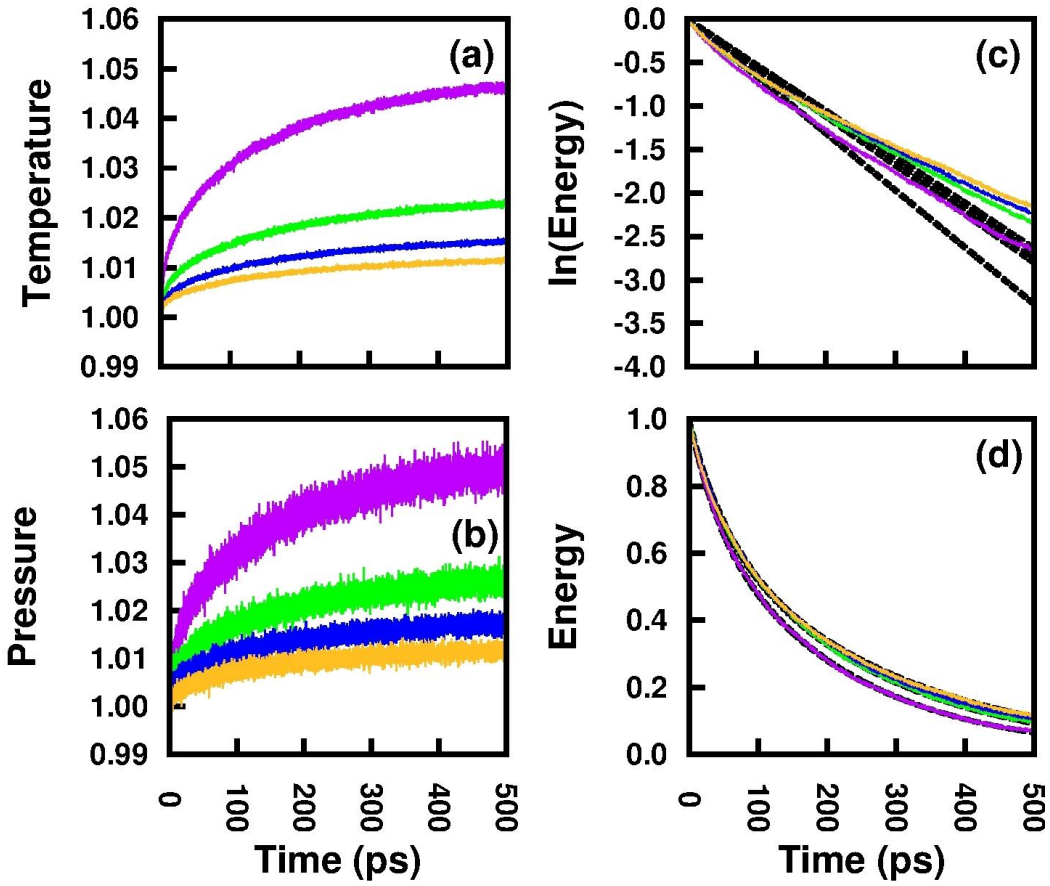

Figure 22. Relaxation results as a function of increasing numbers of Ar bath atoms. (a) Scaled bath gas temperature; 250 Ar, purple curve; 500 Ar, green curve; 750 Ar, blue curve; 1000 Ar, yellow curve. (b) Same as (a), except scaled bath pressure. (c) Vibrational energy decay on semi-log scale with the same coloration as in (a), dashed, black lines correspond to fits to a single exponential function. (d) Vibrational decay with corresponding fits to Eq. 46.

Table XI. Parameters and error bars as a function of number of Ar atoms.

# of Ar	A	B	σ_{AB}	k_1	σ_{k1}	k_2	σ_{k2}
125	0.26	0.74	0.05	0.0301	0.0075	0.0058	0.0003
250	0.26	0.74	0.05	0.0253	0.0053	0.0049	0.0003
500	0.25	0.75	0.05	0.0229	0.0051	0.0042	0.0002
750	0.28	0.72	0.05	0.0201	0.0040	0.0039	0.0002
1000	0.31	0.69	0.05	0.0203	0.0035	0.0036	0.0002

The amplitudes of the exponentials, red curves in Fig. 23a, appear to be only weakly affected by the number of bath atoms within the calculated error bars. The magnitudes of the time constants, blue curves, show a decrease with increasing number of bath gas atoms. These results indicate that the mechanism of the relaxation process is only very weakly dependent on the system size, but the speed of the process is accelerated by the heating of the bath gas, even after the estimated equipartition energy of HO_2 is subtracted off. The magnitudes of both time constants are plotted in Fig. 23b on an expanded scale. The larger time constant increases by about 30% going from the largest number of bath atoms to the smallest; however, it should be noted that the calculated error bars indicate there is a great deal of overlap among the larger time constants. The smaller time constant increases by ≈40% going from the largest to the smallest number of bath gas atoms. There is not as much overlap of the error bars of the smaller time constants, except with the larger simulation size results. This indicates that the slower process is more sensitive to the issue of the finite size of the simulation.

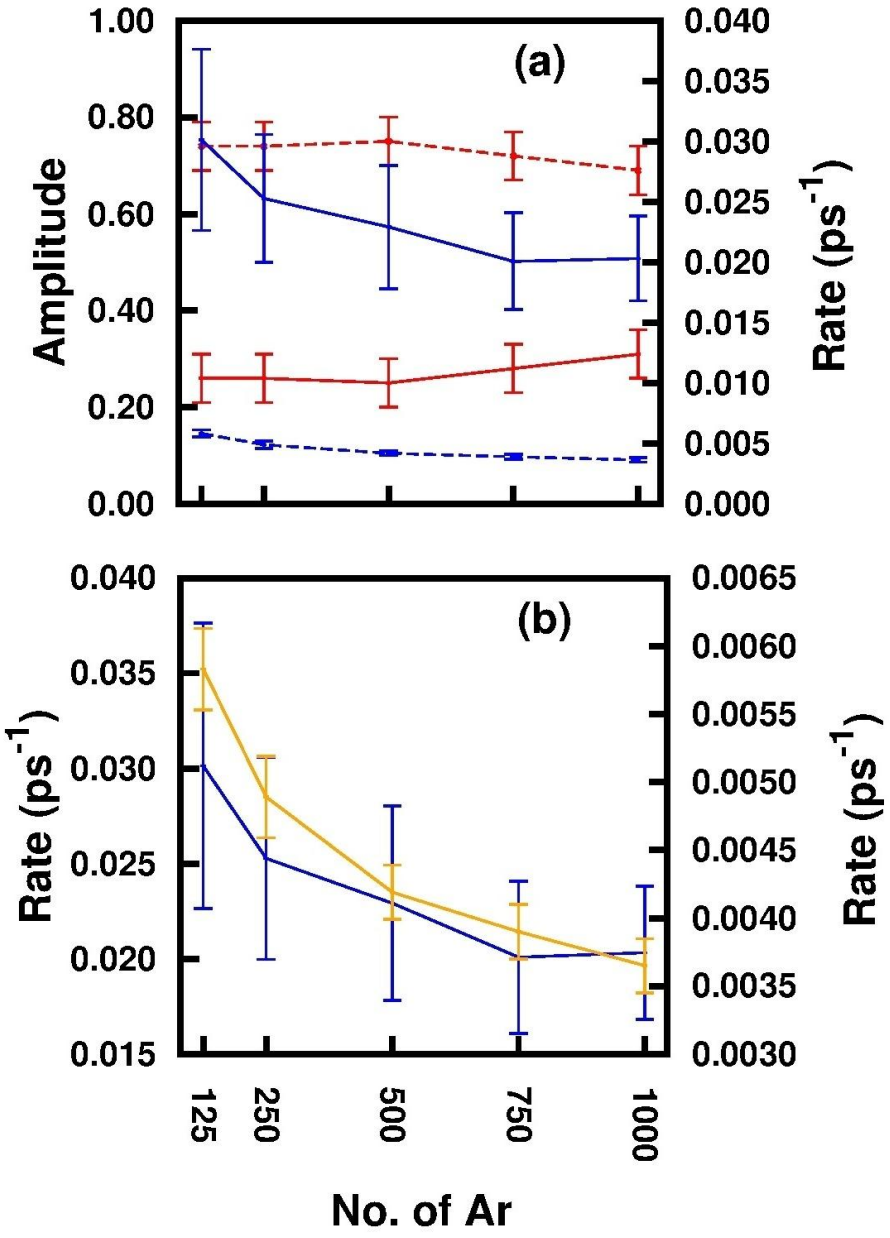

Figure 23. The variation of the time constants and amplitudes obtained in fitting Eq. 46 as a function of the number of bath gas atoms at 800 K and 1300 atm. The lines are intended to guide the eye. The results from the 125 Ar atoms at 1300 atm have also been included in the plotted data. (a) The solid-blue line correspond to the magnitude larger exponential and the solid-red line corresponds to the associated amplitudes. The dashed-blue line corresponds to the magnitude of smaller exponential and the dashed-red lines correspond to the associated amplitudes. (b) Plots of the magnitude of the time constants on an expanded scale; larger time constants are in blue and are relative to the left y-axis and the smaller time constants are in yellow and are relative to the right axis

D. Conclusions

The relaxation of HO_2 embedded in a dense Ar bath was presented in this chapter. Our work was motivated by the nonlinear, density dependent effects on relaxation reported in the experimental studies of Schwarzer *et al.*[19b] on azulene, and Benzler *et al.*[123] on cycloheptatriene, and in the simulations done by Paul *et al.*[19c] on hexaflurobenzene. Given the relative importance of HO_2 in combustion, we were interested in seeing whether the relaxation of vibrationally excited HO_2 has a density (pressure) dependence. We chose to simulate the relaxation process of excited HO_2 embedded in 125 Ar atoms at 800K and 35, 70, 100, 500, 900 and 1300 atm. We have established and validated a general scheme for these simulations that is similar to the methods proposed by others.[19c,125,128,129]

We found that the decay of excess vibrational energy was well represented by a bi-exponential function. This finding is surprisingly similar to the results of Paul *et al.*,[19c] who reported simulations of a much larger solute in a diatomic bath gas. We also observed that both our time constants and the time constants reported by of Paul *et al.* have a non-linear densities dependence similar to the behavior reported by Schwarzer *et al*. and Benzler *et al*. We also reanalyzed the results of Paul *et al.* and found similarities with our results and evidence of turnover behavior. We found that our lower pressure results do not extrapolate to zero in the limit of an infinitely dilute gas.

We also investigated the effect of finite sizes on the relaxation process. The primary size effect is heating of the bath due to energy lost by the solute. We found as expected, that the bath heats up to temperatures predicted by energy equipartition. This heating does not appear to change the relaxation mechanism, but rather it only appears to

accelerate it. The effect of heating is not completely accounted for by making the asymptotic thermal energy of HO_2 a function of the temperature of the bath gas. The finding that the low-pressure time constants do not extrapolate to zero in the limit of low density could be due to this finite size effect, and the lower pressure time constants would likely decrease with increasing system size. The number of Ar atoms will have to be increased by a factor of eight to recover the low-pressure limit.

While we have found evidence of bi-exponential relaxation timescales and pressure effects on the relaxation time constants we do not have a clear mechanism for what is occurring. It is probable that there is an interplay of multiple factors, which ultimately gives rise to the results we report in this paper. A probable mechanism that could have two relaxation timescales is the following. We hypothesize that the first timescale is related to the relaxation of rotational energy. Large extensions of the O-O bond will cause large modulation of the rotational energy. The oscillation of the O-O bond is intimately tied to the loss or gain of rotational energy. A shorter O-O bond length means smaller moments of inertia, so rotational energy will be more easily changed by collisions with the bath. Longer extensions of the O-O bond would mean larger moments of inertia that would make the radical are more resistant to changes in the rotational kinetic energy.. It is probable that loss of rotational energy is mitigated with a slow leakage of energy from the O-O vibrational degree of freedom. A cascade of energy into the bath via the rotational degrees of freedom would continue until these degrees of freedom are thermalized and the magnitude of vibrational energy is not sufficient to sustain longer extension of the O-O bond. A potential test would be to measure the range of oscillation of O-O as the radical is progressively loses energy by collisions. The relaxation process

would then transition to the slower mechanism which would likely consist of a slow direct energy transfer out of the lowest frequency vibrational degrees of freedom.

The turnover of the relaxation time constants with increasing density implies a change in how the bath gas atoms are interacting with the solute. We suspect a change in the local environment of the solute could be the cause of this turnover in the relaxation time constants. In the next section, we discuss some future directions of research that could helpful in understanding the bi-exponential timescales of relaxation and how the bath gas density could cause the turnover of the relaxation time constants.

E. Directions of Future Research

This initial work was motivated by evidence of a breakdown in the IBC assumption of linear scaling of relaxation time constants with increased pressure. While our simulation results show a breakdown in the expected linear scaling effects of pressure the mechanism of this breakdown has not been resolved and there are several avenues for future investigation. It has been suggested[19b,123] that a clustering effect of bath gas around the solute might inhibit collisional energy transfer and could be the source of the turnover effect. Collision events can have a varying finite lifetime, so it seems probable that collision events could overlap at higher densities.[136] Ohmine[122] proposed a potential energy criterion for determining the beginning and ending of collision events, and a relative scale for classifying the collisions that were most effective in relaxing an excited solute. Collisions were determined to occur when the sum of the intermolecular interactions of the bath with the solute became greater than some threshold. This scheme only identifies collisions from the cumulative interatomic potential energy without distinguishing the number bath gas atoms that could be participating in a collision event.

A more precise definition would look at changes in the magnitude of individual interactions. The beginning and end of a collision could then be determined, which would allow assignment of the duration of a collision. The distributions of the lifetimes of the solute-bath collision complexes and the average number of local collision partners could clarify how many-body effects or clustering influence density-dependent relaxation.

The decay of excess-vibrational energy was well represented by a bi-exponential function across all of the simulated pressures. As previously discussed in Sec. C.2a, a similar finding was reported by Paul *et al.*[19c] for a hexaflurobenzene. The bi-exponential fitting is evidence of two relaxation processes. It is possible that IVR is the cause of this binary timescale behavior. We hypothesize that the low frequency mode (O-O) is more likely to lose energy by collisions[137] than high frequency modes (O-H stretch and H-O-O bending motion). The energy flow out of the O-O mode could be mediated by V-R coupling, with the thermalization of the rotational degrees of freedom occurring relatively quickly. The high frequency modes would likely remain relatively isolated from the effects of collisions with the bath gas. A slow transfer of energy out of the high frequency modes could repopulate the O-O mode causing the collisional energy loss to repeat until the chemical species is thermalized. Once sufficient vibrational energy is lost, the repopulation of energy into the O-O mode would slow; consequently, the energy transfer to the bath gas would reflect this change in mechanism. Our IVR simulations of the isolated radical show the possibility of slow, picosecond timescales for internal energy transfer, which would fit in this mechanistic scheme. We are not aware of any internal energy transfer results for hexafluorobenzene. However, von Benten *et al.*[138]

reported picosecond IVR timescales in the experimental relaxation studies of mono-substituted benzenes, so it does not seem unreasonable to propose a slow IVR process as the source of the bi-exponential relaxation reported by Paul *et al*.

V. Conclusions

Some studies of the dynamics of the hydrogen peroxyl radical have been reported in the previous chapters. Beginning with the dynamics of the isolated radical we have compared three PESs for HO_2 in terms of phase space structures using surfaces-of-section, and for IVR, isomerization, and dissociation trajectory dynamics. The IVR shows multiple timescales with the relaxation of excited OO stretch being especially slow for both the IMLS and XXZLG PESs. There is evidence that isomerization helps facilitate IVR from the low frequency O-O mode to the higher frequency modes involving the motion of the hydrogen atom. Slow IVR in turn leads to prominent mode-specific effects in isomerization (on both PESs) and dissociation (only accessible on XXZLG). The isomerization and dissociation populations are best described as bi-exponential with the two timescales being attributed to slow IVR. The DMBE IV results contrast with the results obtained with the other surfaces: IVR occurs on much shorter timescales, mode specific effects are minor or nonexistent, and any effect of isomerization on IVR is also minor. The unimolecular reactions involving this surface are well described by a single timescale.

Future directions of study on isolated HO_2 could be devoted to further quantification of the non-statistical reaction dynamics by comparison of results from additional trajectory studies and variational transition state theory. Investigation of the interaction between rotation and vibration would also be useful in further understanding the timescales of energy transfer in this radical. Comparative studies of the dynamics of the HO_2 radical and the hydrogen peroxyl anion could offer additional insights into the factors and timescales of the dynamics.

The second study focused on the relaxation of HO_2 in a dense gas environment. The relaxation of the radical by collisions with an Ar bath was found to be bi-exponential. The relaxation time constants were found to have a nonlinear density dependence. Finite size effects, primarily in the form of heating, do not appear to change the mechanism, but rather speed up the rate of thermalization. Such finite effects are a likely source for the imperfect match of the time constants to the limit of zero density. The issue of finite size would likely have the same effects on the convergence of the lower pressure relaxation time constants.

Future research directions are proposed with emphasis on understanding if the suggested clustering effect or many body collisions with the bath could be the source of the nonlinear density dependence of the relaxation results. Ohmine[122] proposed a method for identifying and quantifying collisions, which we have modified for analyzing individual collision events. We suggest that IVR and clustering of the bath around the solute as possible sources for the bi-exponential decay of the excess-vibrational energy.

APPENDICES

Appendix I

The contents of this appendix is a listing of the modifications and additions that were made to the classical dynamics code GenDyn in the course of this research. The core program and user manual were obtained from:

http://www.chem.missouri.edu/Thompson/research/gendyn.htm

The subroutines are loosely grouped according to the role of the subroutine in the program: reading runtime conditions, selecting initial conditions, integration, potential energy surface, analysis. The user manual of the original code is sufficiently detailed for a straightforward compilation and execution of the code. The modularity of the programming style allows for easy inclusion of new routines and algorithms. The majority of the following routines were programmed during the course of this dissertation, unless indicated with italics. The subroutines in italics are generally composed of code that was primarily written by others. These subroutines were interfaced and modified for use within GenDyn and original authorship is acknowledged in line with the code. Some of the modified routines are core routines from the original GenDyn code where multiple authors likely contributed; these codes are not in italics. Much of the usage of the code is described in Ch. III and IV and liberal comments in line with the code are present throughout the subroutines.

Some of the code functionality of the routines related to the dense gas simulations were not used, but could be of future interest. The additional functionalities that were not used were: periodic boundary conditions; interatomic force fields for Lennard-Jones

interactions in addition to Buckingham potential; and interactions of a solute embedded in either diatomic, or triatomic bath gases.

Read in: cellinput.f, cellinput.pbc.f, eqcartmod.f, inputmod.f, varymod.f,

Initial conditions: canongas.f, cellboltz.f, cellboltz.pbc.f, celladj.f, cellsz.f, cellsz.pbc.f, *diag.f*, hessgen.f, inmnrg.f, randno.f, stmom.f, roto.excit.f, *paxis3.f90*

Integration: diffverlet.f, diffvprod.f, diffadm.f, pbc.f

PES: *dmbeiv.f, dynamic_parameters.f90,* genpotgas.f, genpotgas.pbc.f, genpotmod.f, , *ho2gxpot.f, ho2mb2001.f, ho2pesfast.f,* intern.pbc.f, *utility.f,* eqnmotmod.f, *PES_3D_subroutine.f90,*

Analysis: analysis.f, backinteg.f, eckart.f, hamsys.f, press.f, rotation.f, rdf.f, writeout.f

Appendix II

Supplemental Material for "A Classical Trajectory Study of the Intramolecular Dynamics and Unimolecular Dissociation of HO_2" by J. Perry, R. Dawes, A. F. Wagner, and D. L. Thompson, J. Chem. Phys. 139, 084319 (2013).

This supplemental material concerns (1) details of the XXZLG potential, (2) kinetic model for energy transfer, and (3) the determination of latency time.

A. XXZLG details

In the XXZLG routine any input geometry is converted to R_{OO}, R_{OH}, and $\angle$OOH and then splines are fit to the *ab initio* energies in these coordinates. Our initial trajectories and subsequent analysis of the XXZLG PES revealed two minor issues that can be loosely characterized as inflexible coordinates and a deficient database.

The coordinate inflexibility is a consequence of how XXZLG forces exchange symmetry with a valence bond coordinate system defined above that does not display that symmetry. The shortest O–H bond is always selected for spline interpolation.[53] This choice has the desired effect that any path through the O–O perpendicular bisector plane will be continuous and exhibit the required exchange symmetry; however, exchange symmetry also requires that any *perpendicular* path through the bisector plane have zero slope at the intersection of the plane. The XXZLG routine does not enforce this requirement, resulting in a discontinuous slope at the perpendicular bisector plane. The patch discussed in Ch. III remedies this problem.

The XXZLG database for the spline fitting is deficient in two ways. First, it would appear that at least for collinear geometries, many of the electronic structure calculations

are not fully converged to the ground state. Within the database there are 173 pairs of collinear geometries that correspond to the same Cartesian geometry; e.g., (R_{OH},∠OOH,R_{OO}) = ($1.0a_0$,180°,$2.2a_0$) or ($3.2a_0$,0°,$2.2a_0$). The two energies for each pair should be identical but the root-mean-square (rms) difference between the two energies over the 173 pairs is ≈3.3 kcal/mol. For energies below 70 kcal/mol, which encompasses both the H + O_2 and O + OH asymptotes, there are 22 pairs with a 1.4 kcal/mol rms difference and a maximum difference of 4.2 kcal/mol.

A second deficiency in the database is its sparsity of configurations. There are two measures of this. The first can be illustrated for the isomerization saddle point. The closest database geometry to that saddle point is (R_{OH},∠OOH,R_{OO}) = ($2.2a_0$,50°,$2.7a_0$). In evaluating the energy for ($2.2a_0$,∠OOH,$2.7a_0$), XXZLG will evaluate the spline shown in Fig. 1 where the dots are the available database entries for ∠OOH given (R_{OH},R_{OO}) = ($2.2a_0$,$2.7a_0$).

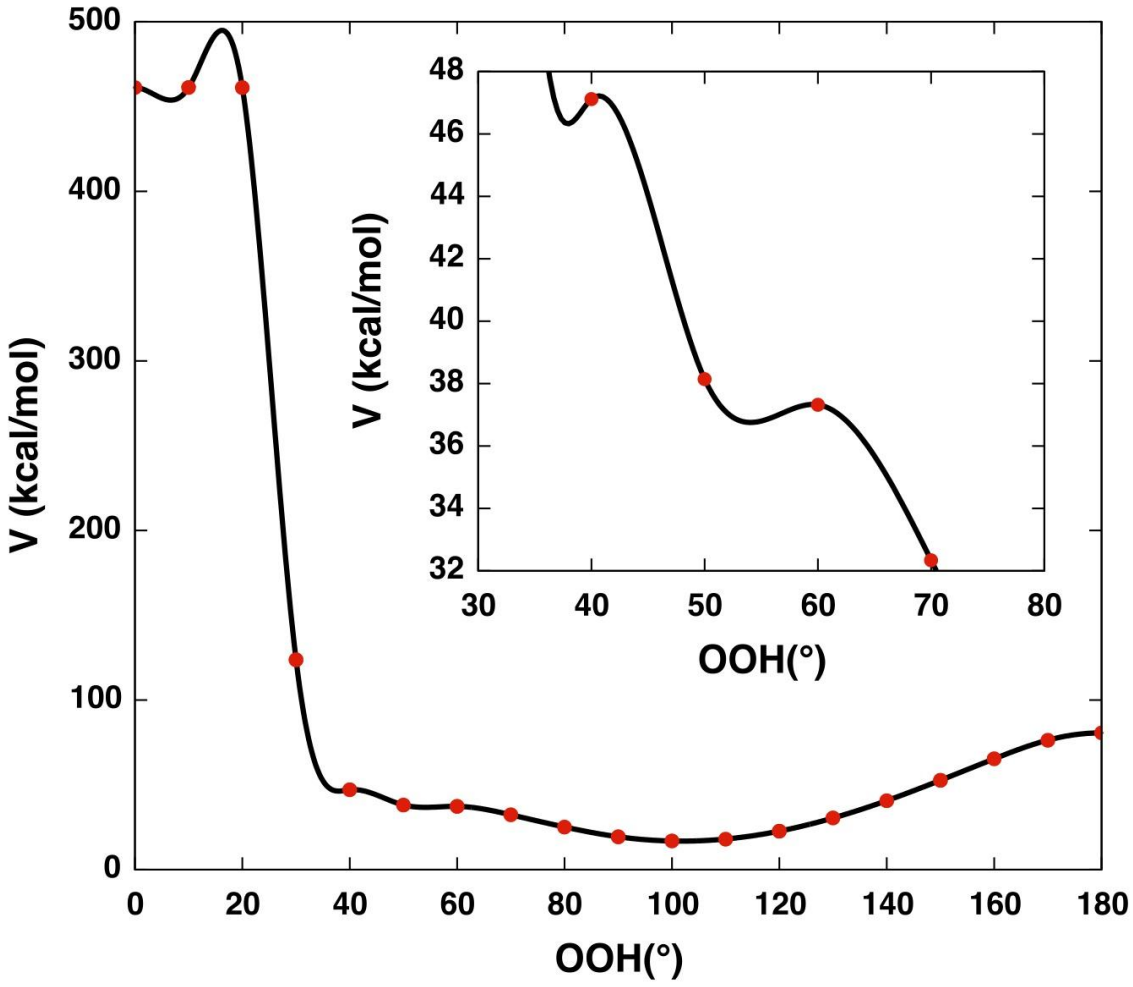

Fig. 1 Spline of the XXZLG potential energy with respect to ∠OOH for database entries where (R_{OH},R_{OO}) is fixed at ($2.2a_0$,$2.7a_0$). The inset is the region of the saddle point.

Those entries are for 10° angular increments and feature ≈300 kcal/mol energy changes over a single increment which leads to ≈1 kcal/mol ripples in the spline near 40° and 50° as seen in the insert of Fig. 1. Using the electronic structure methods that were used to compute the XXZLG data, we calculated an energy 1.3 kcal/mol higher than the XXZLG energy at the XXZLG isomerization saddle point geometry, consistent with the ripple features in Fig. 1. A second measure of database sparsity arises from the fact that ≈25% of the geometries in the database have R_{OH} values that are the larger of the two

R_{OH} values for the given (R_{OO},∠OOH). Because XXZLG only uses the *ab initio* database at the smaller of the two possible R_{OH} values, XXZLG will not exactly recover the database energy for these geometries. About 25% of the database is not fully used or put another way, 25% of the database can be used to quantify the XXZLG "fitting error." For energies less than 70 kcal/mol, the rms fitting error is 0.17 kcal/mol for ≈1,300 geometries. The convergence errors for collinear geometries discussed above contribute to this rms error, but when these points are removed the rms error is 0.13 kcal/mol with a maximum error of 1.0 kcal/mol.

Of course any PES based on an *ab initio* method will have errors inherent in the specific electronic structure theory. However, the XXZLG PES has fitting errors that are measured in a few tenths of a kcal/mol globally and a few kcal/mol for selected regions for energies under 70 kcal/mol. These fitting errors can only be improved by more complete convergence of the electronic structure theory calculations, especially in the collinear region. Further improvements would require either a denser database or a different fitting method, such as interpolative moving least squares,[26c] that can be supported by a database of non-uniform point distribution constructed to minimize the fitting error.

B. Kinetics Model

As a means for interpreting the energy transfer in isolated HO_2 Albert F. Wagner proposed and we jointly developed an analytical kinetics model of energy transfer in a three mode system that is based on two principles: (1) the change in the energy of a mode is directly proportional to the amount of energy the mode currently has and (2) the energy of each mode asymptotically relaxes to the same value, i.e., the total energy divided by the number of modes. These two principles produce the following kinetics model:

$$\begin{aligned}
\frac{dE_1}{dt} &= -(k_{12}+k_{13})E_1 + k_{12}E_2 + k_{13}E_3 \\
\frac{dE_2}{dt} &= k_{12}E_1 - (k_{12}+k_{23})E_2 + k_{13}E_3 \\
\frac{dE_3}{dt} &= k_{12}E_1 + k_{12}E_2 - (k_{13}+k_{23})E_3
\end{aligned} \qquad \text{(S.1)}$$

where E_i is the energy in mode i and k_{ij} is the IVR rate constant for the transfer of energy from mode i to mode j. The second principle, (2) above, of asymptotic equipartition of energy requires $k_{ij} = k_{ji}$. Equation (1) does not make explicit the conservation of total energy. By a change of variables from (E_1, E_2, E_3) to ($E_1+E_2+E_3 = \Sigma$, $E_1 - E_2 = \Delta$, $E_2 - E_3 = \Gamma$), Σ becomes the fixed total energy while Δ and Γ asymptotically go to zero to satisfy the equipartition requirement. Applying the change of variables to Eq. (1) results in:

$$\begin{aligned}
\frac{\partial\Sigma}{\partial t} &= 0 \\
\frac{\partial\Delta}{\partial t} &= -(2k_{12}+k_{13})\Delta - (k_{13}-k_{23})\Gamma \\
\frac{\partial\Gamma}{\partial t} &= -(2k_{23}+k_{13})\Gamma - (k_{13}-k_{12})\Delta
\end{aligned} \qquad \text{(S.2)}$$

The analytic solution for Σ is $\Sigma = E_{total}$ and the solutions for Δ and Γ are

$$\Delta(t) = Ae^{-k_1 t} + Be^{-k_2 t}$$
$$\Gamma(t) = -cAe^{-k_1 t} + \left(\frac{3}{4c}\right)Be^{-k_2 t} - \frac{1}{2}\Delta(t) \qquad \text{(S.3)}$$

where $k_{1(2)} = k_{12}+k_{13}+k_{23} \pm \lambda$, $c = (4\lambda - 2\,k_{12} - k_{13} - k_{23})/(k_{13}-k_{23})$, $\lambda = (k_{12}^2+k_{13}^2+k_{23}^2 - k_{12}k_{13} - k_{12}k_{23} - k_{13}k_{23})^{1/2}$ and A and B are as yet undetermined constants. Equation (3) has three nonlinear parameters that together give the three k_{ij}. From the above, Eqs. (S.3) can be rearranged to provide explicit expressions for $E_i(t)$:

$$E_1(t) = E_{asymp} + \left(\frac{1}{2} - \frac{c}{3}\right)Ae^{-k_1 t} + \left(\frac{1}{2} + \frac{1}{4c}\right)Be^{-k_2 t}$$
$$E_2(t) = E_{asymp} - \left(\frac{1}{2} - \frac{c}{3}\right)Ae^{-k_1 t} - \left(\frac{1}{2} + \frac{1}{4c}\right)Be^{-k_2 t} \qquad \text{(S.4)}$$
$$E_3(t) = E_{asymp} + \left(\frac{2c}{3}\right)Ae^{-k_1 t} - \left(\frac{1}{2c}\right)Be^{-k_2 t}$$

Here E_{asymp} is the asymptotic final energy equal to one third of the total energy.

This model can display two different kinds of structural deficiencies. First, as results in CH. III C.1 show, optimized values of k_1, k_2, and c can be reasonable while an underlying k_{ij} might have a *negative* value. Under such circumstances, the kinetics model may be phenomenologically useful but its k_{ij}'s are not capable of general physical interpretation. In these cases, the reported k_1, k_2, and c values are for a constrained optimization where any optimized negative k_{ij} is constrained to be zero. One way this behavior can happen is when the model is fit to IVR decay over too short a period of time relative to the decay constant such that the decay is very nearly linear in time. Since the energies in all three modes depend only on $\Delta(t)$ and $\Gamma(t)$, under such circumstances the data can only strongly support four constants, namely two intercepts and two slopes s_Δ

and s_Γ. However, the model has five adjustable parameters: k_1, k_2, c, A, and B [see Eq. (S.4)]. If A and B represent the intercept information, the k_1, k_2, and c, or more specifically, three k_{ij}'s must be correlated to obtain the two optimum slopes. This can lead to a k_{ij} being negative because large excursions including into negative values of any one k_{ij} result in negligible change in fitting error if the two other k_{ij}'s change in a correlated fashion. The two slopes s_Δ and s_Γ contain all the rate information and in CH. III C.1 some of the discussion will involve their value.

A second deficiency arises from the nature of Eq. (S.1) where each E_i is controlled by one of the three pairs of rate constants that can be formed from the three k_{ij}'s. In the extreme case where two rates constants are zero, then one of the E_i's and E itself are time independent, allowing the kinetics model to display two different asymptotes. CH. III C.1 does have such a case.

The parameters A and B can be made to give exactly the initial conditions or they can, along with the nonlinear parameters, be least-squares adjusted to the trajectory results for Δ and Γ. As explained in CH. III C.1, A and B are best determined by a linear least-squares process, while the k_{ij} parameters are determined by standard nonlinear least squares fitting methods.[32] Altogether, this makes five adjustable parameters to represent a particular IVR simulation. These nonlinear methods were complemented by a discretized search for apparent local minima on various 3D grids in k_{ij} parameter space. This discretization approach revealed topological features of the rms error surface with respect to the k_{ij} parameters that were useful in determining the global minimum.

C. Latency time

For some mode-specific excitations, for an initial period of time there is either no decay rate or an accelerating decay rate. When decay curves display such features, population data over an initial period of time were excluded from the fit of Eq. (20). This exclusion or, in effect, latency time t_0 was determined by contrasting the rms fitting error to the rms sampling error.[139] The rms sampling error comes from the fact that only a finite number of trajectories are used to construct the population, implying that the population at each time has a sampling uncertainty whose square summed over every time increment leads to the rms sampling error. Both the fitting error and the sampling error change as more data is excluded from their calculation by an increasing latency time. However, the fitting error is initially larger than the sampling error and rapidly decreases as latency time increases, all because of the unsuitability of Eq. (20) for fitting early time features. At the same time, the sampling error changes little with latency time because excluded sampling errors are small when the normalized population is near unity, which it is at early times. We define the latency time as the earliest time at which the fitting and sampling rms errors are equal.

REFERENCES

[1] See, e.g., M. J. Pilling and P. W. Seakins, *Reaction Kinetics*, (Oxford University Press Inc., New York, 1995);

[2] See, e.g.:(a)W. H. Miller, Chem. Rev. **87**, 19 (1987); (b) U. Lourderaj, and W. L. Hase, J. Chem. Phys. A **115**, 2236 (2009).

[3] See, e.g.: (a) P. J. Robinson and K. A. Holbrook, *Unimolecular Reactions* (Wiley, New York, 1972); (b) T. Baer and W. L. Hase, *Unimolecular Reaction Dynamics:Theory and Experiments* (Oxford Uni. Press Inc. New York, 1996).

[4] F. A. Lindenmann, Trans. Faraday Soc. **17**, 598 (1922).

[5] C. N. Hinshelwood, Proc. Roy. Soc. A **113**, 230 (1926).

[6] O. K. Rice, and H. C. Ramsperger, J. Am. Chem. Soc. **49**, 1617 (1927).

[7] (a) L. S. Kassel, J. Phys. Chem. **32**, 225(1928); (b) *ibid* **32**, 1065 (1928).

[8] N. B. Slater, Proc. Camb. Phil. Soc. **35**, 56 (1939).

[9] R. A. Marcus, J. Chem. Phys. **20**, 359 (1952).

[10] E. Fermi, J. R. Pasta, and S. M. Ulam, Los Alamos Scientific Report LA-1940 978 (1955).

[11] J. L. Tuck and M. T. Menzel, Adv. Math. **9**, 399 (1972).

[12] J. Ford. J. Math. Phys. **2**, 387(1961).

[13] See, e.g.: (a) T. Uzer, Phys. Rev. **199**, 73 (1991); (b) M. Gruebele and P. G. Wolynes Acc. Chem. Res. **37**, 261 (2004); (c) B. K. Carpenter, Annu. Rev. Phys. Chem. **56** 57 (2005).

[14] (a) D. L. Bunker, J. Chem. Phys. **37**, 393 (1962); (b) D. L. Bunker, J. Chem. Phys. **40**, 1946 (1964).

[15] D. L. Bunker and W. L. Hase, J. Chem. Phys. **59**, 4621 (1973).

[16] See, e.g. (a) T. R. Rizzo, C. C. Hayden and F. F. Crim, Faraday Discuss. **75**, 223(1983); (b)B. G. Sumpter and D. L. Thompson, J. Chem. Phys. **82**, 4557 (1985); (c) N. F. Scherer and A. H. Zewail J. Chem. Phys **87**, 97 (1987); (d) T. Uzer, J. T. Hynes, and W. P. Reinhardt, J. Chem. Phys. **85**, 5791 (1986); (e) L. J. Butler, T. M. Ticich, and M. D. Likar and F.F. Crim, J. Chem. Phys. **85**, 2331(1986); (f) B. Kuhn and T. R. Rizzo, J. Chem. Phys. **112**, 7461 (2000); (g) M. Joyeux, J. Chem. Phys. **122**, 074303 (2005).

[17] T. A. Litovitiz, J. Chem. Phys. **26**, 469 (1957).

[18] See, e.g.: (a) J. Chesnoy and J.J. Weis, J. Chem. Phys. **84**, 5378 (1986); (b) P. A. Rejto and D. Chandler, J. Phys. Chem. **98**, 12310 (1994)

[19] See, e.g.: (a) K. E. Schultz, D. J. Russell, and C. B. Harris, J. Chem. Phys. **97**, 5431 (1992); (b) D. Schwarzer, J. Troe, M. Votsmeier, and M. Zerezke, J. Chem. Phys, **105**, 3121 (1996); (c) A. K. Paul, S C. Kohale, S. Pratihar, R. Sun, S. W. North and W. L. Hase, *unpublished.*

[20] M. Hénon and C. Heiles, Astron. J. **69**, 73 (1964).

[21] See, e.g.: (a) D. W. , M. L. Koszykowski, and R. A. Marcus, J. Chem. Phys. **67**, 404 (1977); (b) B. Waite and W. H. Miller, J. Chem. Phys. **74,** 3910 (1981); (c) T. D. Sewell, D. L. Thompson, J. D. Gezelter, and W. H. Miller, Chem. Phys. Lett. **193**, 512 (1992).

[22] See, e. g.: M. Tabor, *Chaos and integrability in nonlinear dynamics: an introduction* (Wiley, New York, 1989).

[23] M. Born, and R. Oppenheimer, Ann. Phys. **84** (1927), J. C. Tully, Theor. Chem. Acc. **103** (2000).

[24] See, e.g.: (a) T. D. Sewell and D. L. Thompson, Int. J. Mod. Phys. B **11**, 1067 (1996); (b) L. M. Raff and D. L. Thompson, in *Theory of Chemical Reaction Dynamics*, Vol. 3, edited by M. Baer (CRC, Boca Raton, 1985).

[25] See, e.g., W. L. Hase, K. Song, and M. S. Gordon, Comput. Sci. Eng. **5** (2003).

[26] See, e.g.: (a) D. R. McLaughlin and D. L. Thompson, J. Chem. Phys. **59** 4393 (1973); (b) J. Ischtwan and M. A. Collins, J. Chem. Phys. **100**, 8080 (1994); (c) R. Dawes, D. L. Thompson, A. F. Wagner, and M. Minkoff, J. Chem. Phys. **128**, 084107 (2008).

[27] R. Bellman *Adaptive control processes: A guided tour* (Princeton University Press, Princeton, NJ, 1961).

[28] See, e.g.: (a) Y. Guo, L. B. Harding, A. F. Wagner, M. Minkoff, and D. L. Thompson, J. Chem. Phys. **126**, 104105 (2007); (b) R. Dawes, D. L. Thompson, Y. Guo, A. F. Wagner, and M. Minkoff, J. Chem. Phys. **126**, 184108 (2007).

[29] N. Metropolis, A. W. Rosenbluth, M. N. Rosenbluth, A. H. Teller, and E. Teller, J. Chem. Phys. **21**, 1087 (1953).

[30] See, e. g.: (a) D. Frenkel, and B. Smit, *Understanding Molecular Simulation From Algorithms to Applications* (Academic Press, San Diego 2002); (b) M. P. Allen, and D. J. Tildesley, Computer Simulation of Liquids. (Oxford University Press: New York City, 1987); (c) J. M. Haile, *Molecular Dynamics Simulation: Elementary Methods* (John Wiley & Sons, Inc., 1992).

[31] E. B. Wilson, Jr., J. C. Decius, and P. C. Cross, *Molecular Vibrations: The Theory of Infrared and Raman Vibrational Spectra* (Dover, New York, 1980).

[32] See, e.g., W. H. Press, B. P. Flannery, S. A. Teukolsky, and W. T. Vetterling, *Numerical Recipes* (Cambridge University, New York, 1989).

[33] W. L. Hase, D. G. Buckowski, and K. N. Swamy, J. Phys. Chem. **87**, 2754 (1983).

[34] R. Viswanathan, L. M. Raff, and D. L. Thompson, J. Chem. Phys. **81**, 828 (1984).

[35] See, e. g.: (a) G. Nyman, S. Nordholm, and H. W. Schranz, J. Chem. Phys. **93**, 6767 (1990); (b) H. W. Schranz, S. Nordholm, and G. Nyman, J. Chem. Phys. **94**, 1487 (1991); (c) G. Nyman, K. Rynefors, L. Holmlid, J. Chem. Phys. **88**, 3572 (1988).

[36] See, e.g.:(a) S. K. Gray, D. W. Noid and B. G. Sumpter, J. Chem. Phys. **101**, 4062 (1994); (b) J. M. Millam, V. Bakken, W. Chen, W. L. Hase, and H. B. Schlegel, J. Chem. Phys. **111,** 3800(1999).

[37] See, e.g.: See, *e.g.*: (a) R. W. Hamming, *Numerical Methods for Scientists and Engineers*, 2nd ed. (McGraw-Hill, Inc: New York, 1973).

[38] GENDYN. Code and Manual are available at http://www.chem.missouri.edu/Thompson/research/gendyn.htm

[39] S. Gill, Proc. Cambridge Phil. Soc. **47**, 96 (1951).

[40] H. O. Pritchard, Cent. Eur. J. Chem. **9**, 753(2011).

[41] W. C. Swope, H. C. Anderson, P. H. Berens and K. R. Wilson, J. Chem. Phys. **76**, 637 (1982).

[42] See, e.g.: (a) M. Tuckerman, B. J. Berne, and G. J. Martyna, J. Chem. Phys. **97**, 1990 (1992); (b) R. D. Skeel, G. Zhang, and T. Schlick Siam J. Sci. Comp. **18**, 203(1997).

[43] C. A. Parr, Ph.D. Dissertation, California Institute of Technology, 1969.
[44] See, e.g.: (a) W. H. Miller, J. Phys. Chem. A **105**, 2942 (2001); (b) G. S. Ezra, in *Advances in Classical Trajectory Methods: Comparisons of Classical and Quantum Dynamics*, (JIA Press, 1998).
[45] T. D. Sewell, D. L. Thompson, J. D. Gezelter, and W. H. Miller, Chem. Phys. Lett. **6**, 512 (1992)
[46] Y. Guo, D. L. Thompson, and T. D. Sewell, J. Chem. Phys. **104**, 576 (1996).
[47] See, e.g.: (a) N. Makri and W. H. Miller, J. Chem. Phys. **91** 4026 (1989); (b) T. D. Sewell, Y. Guo and D. L. Thompson, J. Chem. Phys. **103**, 8557 (1995).
[48] See, e.g.: (a) B. Efron, SIAM Rev. **21**, 460 (1979); (b) P. Diaconis and B. Efron, Sci. Am. **248**, 166 (1983).
[49] See, *e.g.*, J. A. Miller, M. J. Pilling, and J. Troe, Proc. Combust. Inst. **30**, 43 (2005).
[50] M. R. Pastrana, L. A. M. Quintales, J. Brandão, and A. J. C. Varandas, J. Chem. Phys. **94**, 8073 (1990).
[51] B. Kendrick and R. T Pack, J. Chem. Phys. **102**, 1994 (1995).
[52] L. B. Harding, A. I. Maergoiz, J. Troe, and V. G. Ushakov, J. Chem. Phys. **113**, 11019 (2000).
[53] C. Xu, D. Xie, D. H. Zhang, S. Y. Lin, and H. Guo, J. Chem. Phys. **122**, 244305 (2005).
[54] D. Xie, C. Xu, T. Ho, H. Rabitz, G. Lendvay, S. Y. Lin, and H. Guo, J. Chem. Phys. **126**, 074315 (2007).
[55] C. Xu, D. Xie, P. Honvault, S. Y. Lin, and H. Guo, J. Chem. Phys. **127**, 024304 (2007).
[56] A. Li, D. Xie, R. Dawes, A. W. Jasper, J. Ma, and H. Guo, J. Chem. Phys. **133**, 144306 (2010).
[57] J. Brandão, C. M. A. Rio, and J. Tennyson, J. Chem. Phys. **130**, 134309 (2009).
[58] H.-J. Werner and P. J. Knowles, J. Chem. Phys. **89**, 5803 (1988).
[59] P. J. Knowles and H.-J. Werner, Chem. Phys. Lett. **145**, 514 (1988).
[60] S. R. Langhoff and E. R. Davidson, Int. J. Quantum Chem. **8**, 61 (1974)
[61] C. F. Melius and R. J. Blint, Chem. Phys. Letters **64,** 183 (1979).
[62] (a) S. P. Walch, C. M. Rohlfing, C. F. Melius, and C. W. Baushlicher, Jr., J. Chem. Phys. **88**, 6273 (1988); (b) *ibid*. **90**, 7613 (1989); (c) S. P. Walch and C. M. Rohlfing, *ibid.* **91**, 2373 (1989).
[63] (a) K. G. Lubic, T. Amano, H. Uehara, K. Kawaguchi, and E. Hirota, J. Chem. Phys., **81**, 4826 (1984); (b) H. Uehara, K. Kawaguchi, and E. Hirota, J. Chem. Phys. **83,** 5479 (1985); (c) J. F. Ogilvie, Can. J. Spectrosc. **19**, 171 (1973); (d) C. Yamada, Y. Endo, and E. Hirota, J.Chem. Phys. **78**, 4379 (1983); (e) J. B. Burkholder, P. D. Hammer, C. J. Howard, J. P. Towle, and J. M. Brown, J. Mol. Spectrosc. **151**, 493 (1992); (f) J. D. DeSain, A. D. Ho, and C. A. Tattjes, J. Mol. Spectrosc. **219,** 163 (2002).
[64] A. J. C. Varandas, J. Chem. Phys. **90**, 4379 (1989).
[65] See, *e.g.*, J. N. Murrell, S. Carter, S. C. Farantos, P. Huxley, and A. J. C. Varandas, *Molecular Potential Energy Function*s, (John Wiley & Sons: New York, 1984).
[66] V. A. Mandelshtam, T. P. Grozdanov, and H. S. Taylor, J. Chem. Phys. **103**, 10074 (1995).

[67] C. Yang and S. J. Klippenstein, J. Chem. Phys. **103**, 7287 (1995).
[68] M. A. Bajeh, E. M. Goldfield, A. Hanf, C. Kappel, A. J. H. M. Meijer, H.-R. Volpp, and J. Wolfrum, J. Phys. Chem. A **105**, 3359 (2001).
[69] M. Stumpf, A. J. Dobbyn, D. H. Mordaunt, H.-M. Keller, H. Fluethmann, R. Schinke, H.-J. Werner, and K. Yamashita, Faraday Discuss. **102**, 193 (1995).
[70] J. M. C. Marques and A. J. C. Varandas, J. Phys. Chem. A. **101**, 5168 (1997).
[71] A. J. Dobbyn, M. Stumpf, H.-M. Keller, W. L. Hase, and R. Schinke, J. Chem. Phys. **102**, 5867 (1995).
[72] A. J. H. M. Meijer and E. M. Goldfield, J. Chem. Phys. **110**, 870(1999).
[73] J. A. Miller, J. Chem. Phys. **84**, 6170 (1986).
[74] J. A. Miller and B. C. Garrett, Int. J. Chem. Kinet. **29**, 275 (1997).
[75] R. J. Duchovic and M. A. Parker, J. Phys. Chem. A. **109**, 5883 (2005).
[76] W. J. Lemon and W. L. Hase, J. Phys. Chem. **91**, 1596 (1987).
[77] S. Y. Lin, D. Xie, and H. Guo, J. Chem. Phys. **125**, 091103 (2006).
[78] C. Xu, B. Jiang, D, Xie, S. C. Farantos, S. Y. Lin, and H. Guo, J. Phys. Chem. A. **111**, 10353 (2007).
[79] S. Y. Lin, H. Guo, P. Honvault, and D. Xie, J. Phys. Chem. B **110**, 23641 (2006).
[80] P. Bargueño, T. González-Lezana, P. Larrégaray, L. Bonnet, J. C. Rayez, M. Hankel, S. C. Smith, and A. J. H. M. Meijer, J. Chem. Phys. **128**, 244308 (2008).
[81] S. Y. Lin, H. Guo, P. Honvault, C. Xu, and D. Xie, J. Chem. Phys. **128**, 014303 (2008).
[82] G. Lendvay, D. Xie, and H. Guo, Chem. Phys. **349**, 181 (2008).
[83] M. Jorfi, P. Honvault, P. Bargueño, T. G.-Lezana, P. Larrégaray, L. Bonnet, and P. Halvick, J. Chem. Phys. **130**, 184301 (2009)
[84] See, e.g.: (a) M. M. Graff and A. F. Wagner. J. Chem. Phys. **92**, 2423 (1990); (b) J. Ma, H. Guo, C. Xie, A. Li and D. Xie, Phys. Chem. Chem. Phys. **13**, 8407 (2011).
[85] This work was started prior to the publication of the fourth version of the XXZLG reported in Ref. 56.
[86] See**,** *e.g.*, G. Wu, G. C. Schatz, G. Lendvay, D. Fang, and L. B. Harding, J. Chem. Phys. **113**, 3050 (2000).
[87] C. R. Gallucci and G. C. Schatz. J. Phys. Chem. **86**, 2352 (1982). They used a similar symmetrization strategy to correct a similar seam in an earlier HO_2 PES.
[88] G. Herzberg, *Molecular Spectra and Molecular Structure*, Spectra of Diatomic Molecules Vol. 1 (Van Nostrand, Princeton, 1950).
[89] M. P. Deskevich, D. J. Nesbitt, and H.-J. Werner, J. Chem. Phys. **120**, 7281 (2004).
[90] R. Dawes, A. W. Jasper, T. C. Richmond, C. Mukarakate, S. H. Kable, and S. A. Reid, J. Phys. Chem. Lett. **1**, 641 (2010).
[91] H.-J. Werner and P. J. Knowles, J. Chem. Phys. **89**, 5803 (1988).
[92] P. J. Knowles and H.-J. Werner, Chem. Phys. Lett. **145**, 514 (1988).
[93] T. Helgaker, P. Jorgensen, and J. Olsen, *Molecular Electronic Structure Theory* (Wiley, New York, 2000).
[94] T. H. Dunning, J. Chem. Phys. **90**, 1007 (1989).
[95] R. Dawes, D. L. Thompson, A. F. Wagner, and M. Minkoff, J. Phys. Chem. A **113**, 4709 (2009).

[96] R. Dawes, X.-G. Wang, A. W. Jasper, and T. Carrington Jr., J. Chem. Phys. **133**, 134304 (2010).

[97] B. Ruscic, private communication of ATcT result based on version 1.110 of the Core (Argonne) Thermochemical Network (May 17, 2010); B. Ruscic, R. E. Pinzon, M. L. Morton, G. von Laszewski, S. Bittner, S. G. Nijsure, K. A. Amin, M. Minkoff, and A. F. Wagner, J. Phys. Chem. A **108**, 9979 (2004); B. Ruscic, R. E. Pinzon, G. von Laszewski, D. Kodeboyina, A. Burcat, D. Leahy, D. Montoya, and A. F. Wagner, J. Phys.: Conf. Ser. **16**, 561 (2005); W. Klopper, B. Ruscic, D. P. Tew, F. A. Bischoff, and S. Wolfsegger, Chem. Phys. **356**, 14 (2009).

[98] The range of the IMLS PES only extends to $R_{H\text{--}OO'} = 2.65$ Å, so the asymptotic energy was evaluated from an electronic structure calculation with $R_{H\text{--}OO'} = 25.0$ Å. The difference in energy between 25.0 Å and 2.65 Å is 0.11 kcal/mol.

[99] (a) J. Echave and D. C. Clary, Chem. Phys. Lett. **190**, 225 (1992); (b) H. Wei and T. Carrington, Jr., J. Chem. Phys. **97**, 3029 (1992).

[100] See, *e.g.*, A. J. Lichtenberg and M. A. Lieberman, *Regular and Stochastic Motion* (Springer, New York, 1983).

[101] L. Seidel, C. González-Giralda, R. M. Benito, and F. Borondo, Int. J. Quantum Chem. **86**, 175 (2002).

[102] G. L. Barnes and M. E. Kellman, J. Chem. Phys. **133**, 101105 (2010); *ibid* **134**, 074108 (2011).

[103] See, *e.g.*, *CRC Standard Mathematical Tables* 25th ed., edited by W. H. Beyer (CRC Press Inc: Boca Raton, 1982**)**.

[104] We tested initial conditions selected by a local mode excitation (see Ref. 24 and references therein) for both OH* and OO* and found that the number of "ballistic" trajectories in the decay of the OH* ensembles decreased but was not eliminated, and there was no effect on the "latency time" seen in the decay of the OO*ensemble population.

[105] See, *e.g.*: (a) C. C. Chambers, and D. L. Thompson, Chem. Phys. Lett. **218**, 166 (1994); (b) D. J. Nesbitt and R. W. Field, J. Phys. Chem. **100**, 12735 (1996).

[106] The results in Table VI are the same as those of Marques and Varandas (See Table 1 in Ref. 70) for OO* and OH* but are ≈10% higher for OOH*. Marques and Varandas defined the time of dissociation as the time when separation of H from O_2 reached 5 Å, not the time of the last inner turning point as we have. More importantly, they ran half the number of trajectories used here. Bootstrap error estimation [W. H. Press, B. P. Flannery, S. A. Teukolsky, and W. T. Vetterling, *Numerical Recipes* (Cambridge University, New York, 1989).] that randomly resampled thousands of groups of 500 trajectory lifetimes out of our original ensemble of 1000 trajectories produced a Gaussian-like distribution of rate constants from which a 1σ error bar could be estimated. Inclusion of an individual trajectory multiple times in an individual bootstrapped data set was possible in this application. Only for OOH* are the Marques and Varandas results outside our 1σ error bar but then within the 2σ error bar. We conclude the small disagreement for OOH* are due to somewhat unusual statistical fluctuations due to small sample size.

[107] See, e.g., B. M. Rice, J. Grosh, and D. L. Thompson, J. Chem. Phys. **102**, 8790 (1995).

[108] See, *e.g.*, B. G. Sumpter and D. L. Thompson, J. Chem. Phys. **86**, 2805 (1987).
[109] See, e.g.: W.-T. Chan and I. P. Hamilton, J. Chem. Phys. **105**, 5907 (1996); (b) W.-T. Chan and I. P. Hamilton Chem. Phys. Lett. **292**, 57 (1998); (c) K. Geise and O. Kühn, J. Chem. Theo. Comput. **2**, 717 (2006).
[110] *See, e.g.*: (a) R. Viswanathan, L. M. Raff, and D. L. Thompson, J. Chem. Phys. **81**, 828 (1984); (b) T. D. Sewell, H. W. Schranz, D. L. Thompson, and L. M. Raff, J. Chem. Phys., **95**, 8069 (1991).
[111] J. Perry, R. Dawes, A. F. Wagner, D. L. Thompson, J. Chem. Phys. 139, 084319 (2013).
[112] J. H. Frederick, G. M. McCelland, and P. Brumer, J. Chem. Phys. **83**, 190 (1985).
[113] See, e.g.: (A) B. Brumfield, W. Sun, Y. Ju, and G. Wysocki, J. Phys. Chem. Lett. **4**, 827 (2013); (b) M. P. Burke, M. Chaos, F. L. Dryer, and Y. Ju, Combust. Flame. **157**, 618 (2010).
[114] G. L. Pollack, Rev. Mod. Phys. **36**, 748 (1964).
[115] See, e.g.: (a) D. Oxtoby, Ann. Rev. Phys. Chem. **32**, 77 (1981); (b) R. M. Stratt, and M. Maroncelli, J. Phys. Chem. **100**, 12981 (1996).
[116] T. A. Litovitiz, J. Chem. Phys. **26**, 469 (1957).
[117] See, e.g.: (a) R. Zwanzig. J. Chem. Phys. **34**, 1931 (1961); (b) M. Fixman, J. Chem. Phys. **34**, 369 (1960); (c) M. Fixman, J. Chem. Phys. **34**, 369 (1960)
[118] K. Herzfeld, J. Chem. Phys. **36**, 3305 (1962).
[119] P. K. Davis and I. Oppenheim, J. Chem **57,** 505 (1972).
[120] P. S. Dardi and R. I. Cukier, J. Chem. Phys. **95**, 98 (1991).
[121] M. Châtelet, B. Oksengorn, G. Widenlocher and Ph. Marteau, J. Chem. Phys. **75**,2374 (1981); M. Châtelet, J. Kieffer, and B. Oksengorn, Chem. Phys. **79**, 413 (1983).
[122] I. Ohmine, J. Chem. Phys. **85**, 3342 (1986)
[123] J. Benzler, S. Linkersdörfer and K. Luther, J. Chem. Phys. **106**, 4992 (1997).
[124] See, e.g: (a) O. Kajimoto, M. Futakami, T. Kobayashi and K. Yamasaki, J. Chem. Phys. **92**, 1347 (1988); (b) A. Morita, and O. Kajimoto, J. Phys. Chem. **94**, 6420 (1990); (c) S. C. Tucker, Chem. Rev. **99**, 391 (1999).
[125] (a) C. Heildelbach, I. I. Fedchenia, D. Schwarzer, and J. Schroeder, J. Chem. Phys. **108**, 10152 (1998); (b) C. Heildelbach, V. S. Vikhernko, D. Schwarzer, and J. Schroeder. J. Chem. Phys. **110**, 5286 (1999).
[126] N. J. Brown and J. A. Miller, J. Chem. Phys. **80**
[127] A. J. C. Varandas, and L. Zhang, Chem. Phys. Lett. **402**, 399 (2005).
[128] See, *e g.*: (a) A. J. Marks, J. N. Murrell, and A. J. Stace, J. Chem. Phys. **94**, 3908 (1991); (b) E. P. Wallis, and D. L. Thompson, J. Chem. Phys. **99,** 2662 (1993).
[129] See, *e.g.*: (a) Y. Guo, and D. L. Thompson, J. Chem. Phys. B **103**,10599 (1999); (b) K. Bolton, W. L. Hase, and C. Doubleday, Jr. J. Phys. Chem. B, **103**, 3691(1999).
[130] J. V. Michael, M.-C. Su, J. W. Sutherland, J. J. Carroll, and A. F. Wagner, J. Chem. Phys. A. **106** 5297(2002).
[131] A. J. Marks, J. N. Murrell, A. J. Stace, and H. Buscher, Mol. Phys. **65**, 1153 (1988).
[132] L. Verlet, Phys. Rev. **159**, 98 (1967).
[133] J. P. Chandler, *Subroutine Stepit*, Comp. Sci. Dept. Oklahoma State University, (1991).

[134] See, e.g., S. W. Smith, *The Scientist and Engineer's Guide to Digital Signal Processing* (Cal. Tech. Publishing, San Diego, 1997).

[135] *See, e.g*. R. C. Tolman, Phys. Rev. **11**, 261 (1918).

[136] *See, e.g*., V. Bernshtein, K. F. Lim, and I. Oref., J. Phys. Chem. **99**, 4531 (1995).

[137] See, e.g.: (a) C. G. Elles, M. J. Cox and F. F. Crim, J. Chem. Phys. **120**, 6973 (2004); (b) A. V. Davis, R. Wester, A. E. Bragg, and D. M. Neumark, J. Chem. Phys. **119**, 2020 (2003).

[138] R. S. von Benten, Y. Liu and B. Abel, J. Phys. Chem. A. **114**, 11522 (2010).

[139] If N is the total number of trajectories and Np(t) is the number of trajectories that define a population P at time t, then P(t) = Np(t)/N and the sampling error is $P(t)[(1-P(t))/Np(t)]^{1/2}$.

VITA

Jamin W. Perry was born on September 25th, 1984 in Joplin, MO to James and Janine Perry. He attended Missouri Southern State University and graduated with honors in May 2003 with Bachelors of Science in Chemistry and Physics. In August 2008 he began his studies at the University of Missouri-Columbia and in Dec. 2008 he joined Dr. Donald Thompson's research group. He completed the requirements for his PhD in May 2014.